SYNTHESIS AND CHARACTERIZATION OF SOLAR PYROLYZED RICE HUSK ASH AS A CATALYST SUPPORT

A THESIS SUBMITTED TO
THE GRADUATE SCHOOL OF NATURAL AND APPLIED SCIENCES
OF
MIDDLE EAST TECHNICAL UNIVERSITY

BY

OĞUZHAN COŞĞUN

IN PARTIAL FULFILLMENT OF THE REQUIREMENTS
FOR
THE DEGREE OF MASTER OF SCIENCE
IN
CHEMICAL ENGINEERING

DECEMBER 2024

Approval of the thesis:

SYNTHESIS AND CHARACTERIZATION OF SOLAR PYROLYZED RICE HUSK ASH AS A CATALYST SUPPORT

submitted by **OĞUZHAN COŞĞUN** in partial fulfillment of the requirements for the degree of **Master of Science** i**n Chemical Engineering, Middle East Technical University** by,

Prof. Dr. Naci Emre Altun
Dean, **Graduate School of Natural and Applied Sciences** _____

Prof. Dr. Yusuf Uludağ
Head of the Department, **Chemical Engineering** _____

Prof. Dr. Deniz Üner
Supervisor, **Chemical Engineering, METU** _____

Examining Committee Members:

Prof. Dr. Gülay Ertaş
Chemistry, METU _____

Prof. Dr. Deniz Üner
Chemical Engineering, METU _____

Assoc. Prof. Dr. Bahar İpek Torun
Chemical Engineering, METU _____

Assist. Prof. Dr. Necip Berker Üner
Chemical Engineering, METU _____

Assist. Prof. Dr. Samira Fatma Kurtoğlu Öztulum
Materials Science and Technology, TAU _____

Date: 27.12.2024

I hereby declare that all information in this document has been obtained and presented in accordance with academic rules and ethical conduct. I also declare that, as required by these rules and conduct, I have fully cited and referenced all material and results that are not original to this work.

Name Last name : Oğuzhan Coşğun

Signature :

ABSTRACT

SYNTHESIS AND CHARACTERIZATION OF SOLAR PYROLYZED RICE HUSK ASH AS A CATALYST SUPPORT

Coşğun, Oğuzhan
Master of Science, Chemical Engineering
Supervisor : Prof. Dr. Deniz Üner

December 2024, 109 pages

Rice husk ash was produced and characterized by solar pyrolysis method in this study, and its utilization as a catalyst support was investigated. Results were compared with industrially produced flame pyrolyzed rice husk ash samples to observe the effect of solar pyrolysis. For that purpose, solar pyrolysis of rice husk was conducted and several samples with varying carbon contents were produced. Flame and solar pyrolyzed samples were thoroughly characterized. Stability of the samples were investigated by thermal gravimetric analysis and temperature programmed reduction. Morphology was studied with scanning electron microscopy and Brunauer-Emmett-Teller analysis. Surface characterization was performed by electron spin resonance spectroscopy, nuclear magnetic resonance spectroscopy, Fourier transform infrared spectroscopy, Raman spectroscopy, and X-ray diffraction crystallography. Adsorption isotherms were measured with acidic carbon dioxide and basic ammonia gases. Catalyst was prepared by incipient wetness impregnation method, and used in temperature programmed reduction analysis in the presence of hydrogen. Results indicate solar pyrolysis to be an effective method to produce rice husk ash with high stability and hierarchical porosity where carbon content, porosity, and free electron density can be engineered by manipulating the exposure time to

concentrated solar energy. Temperature programmed studies show rice husk ash to be a stable support for palladium catalysts in the presence of hydrogen.

Keywords: Rice Husk Ash, Catalyst Support, Characterization, Spectroscopy, Carbon

ÖZ

GÜNEŞ ENERJİSİ İLE PİROLİZ EDİLMİŞ ÇELTİK KABUĞU KÜLÜNÜN KATALİZÖR DESTEĞİ OLARAK SENTEZİ VE KARAKTERİZASYONU

Coşğun, Oğuzhan
Yüksek Lisans, Kimya Mühendisliği
Tez Yöneticisi: Prof. Dr. Deniz Üner

Aralık 2024, 109 sayfa

Bu çalışmada, solar piroliz yöntemi ile üretilmiş çeltik kabuğu külü karakterize edilmiş ve katalizör desteği olarak kullanımı incelendi. Sonuçlar, güneş pirolizinin etkisini gözlemlemek için endüstriyel olarak, alevle piroliz edilmiş çeltik kabuğu külü numuneleri ile karşılaştırıldı. Bu amaçla, çeltik kabuğunun yoğunlaştırılmış güneş enerjisi ile pirolizi yapıldı ve farklı karbon içeriklerine sahip çeltik kabuğu külü numuneleri üretildi. Alev ve güneş pirolizi yöntemleri ile üretilmiş numuneler kapsamlı bir şekilde karakterize edildi. Numunelerin kararlılığı termal gravimetrik analiz ve sıcaklık programlı indirgeme ile; morfoloji, taramalı elektron mikroskobu ve Brunauer-Emmett-Teller analizi ile incelendi. Yüzey karakterizasyonu, elektron spin rezonans spektroskopisi, nükleer manyetik rezonans spektroskopisi, Fourier dönüşümlü kızılötesi spektroskopisi, Raman spektroskopisi ve X-ışını kırınım kristalografisi gibi yöntemlerle gerçekleştirildi. Adsorpsiyon izotermleri asidik karbondioksit ve bazik amonyak gazları ile ölçüldü. Katalizör, ıslaklık başlangıcı emdirme yöntemi ile hazırlanmıştır ve hidrojen varlığında sıcaklık programlı indirgeme analizlerinde kullanıldı. Sonuçlar, güneş pirolizinin, konsantre güneş enerjisine maruz kalma süresinin manipüle edilmesiyle karbon içeriği, gözeneklilik ve serbest elektron yoğunluğunun tasarlanabildiği yüksek kararlılık ve hiyerarşik

gözenekliliğe sahip çeltik kabuğu külü üretmek için etkili bir yöntem olduğunu göstermektedir. Sıcaklık programlı indirgeme deneyleri, çeltik kabuğu külünün, hidrojen varlığında paladyum katalizörleri için stabil bir destek olduğunu desteklemektedir.

Anahtar Kelimeler: Çeltik Kabuğu Külü, Katalizör Desteği, Karakterizasyon, Spektroskopi, Karbon

To my late uncle, Ümit

ACKNOWLEDGMENTS

I would like to express my gratitude to my supervisor, Prof. Dr. Deniz Üner, who perhaps has the most significant impact on who I am as a researcher, an engineer, and a person. I extend my gratitude to all past and present members of the Uner Research Group. Particularly, Begüm Yılmaz, Dr. Mustafa Yasin Aslan and Seyithan Deniz Ergül are acknowledged for their help.

I am deeply thankful to Ezgi Altıntaş, Gökhan Sağlam, Zeynep Birce Reyhan, Hüseyin Öztürk, Yaşar Görkem Bak, Zeynep Ece Akgül, Elif Ferligül, Azad Yılmaz, Asena Kızıl, Selin Karahan, Almira Çaldıklıoğlu, Alican Ertaş, Dr. Merve Sarıyer, and Bengisu Barış for their much precious love, support and frendship.

I am priviledged to call Berkehan Karaman, Boran Özlen, and Onur Karaman my best friends. Life would not feel the same without them.

I am eternally grateful to my parents, Nalan and Şadi, for their unconditional love and support towards me. They have been my greatest strength from the very beginning of my life. As well, I am utterly lucky to have my brother, Onuralp, in my life. I want to thank him for being there.

Volkan Veziroğlu of Silo Gıda is kindly acknowledged for the rice husk and rice husk ash samples.

Financial support from State Oil Company of Azerbaijan Republic (SOCAR) is gratefully acknowledged (Project code: ODTU TTO GC-009-2022).

Financial support from TÜBİTAK program 2210-A is gratefully acknowledged.

TABLE OF CONTENTS

LIST OF TABLES

TABLES

LIST OF FIGURES

FIGURES

LIST OF ABBREVIATIONS

ABBREVIATIONS

BET	Brunauer-Emmett-Teller
BJH	Barrett-Joyner-Halenda
ESR	Electron Spin Resonance
FP	Flame Pyrolyzed
FT-IR	Fourier Transform Infrared
IUPAC	International Union of Pure and Applied Chemistry
NMR	Nuclear Magnetic Resonance
RB5	Reactive Black 5
RH	Rice Husk
RHA	Rice Husk Ash
SEM	Scanning Electron Microscopy
SP	Solar Pyrolyzed
TGA	Thermal Gravimetric Analysis
TPR	Temperature Programmed Reduction
UV-Vis	Ultraviolet Visible
XRD	X-Ray Diffraction

CHAPTER 1

INTRODUCTION

1.1 Carbon

Carbon is the fourth most abundant element in the universe and the building block of all organic matter on earth [1,2]. Due to the flexibility in bonding configurations of carbon molecules, it can exist in many different forms each of which have unique properties of their own. Some well-known allotropes of carbon are shown in Figure 1-1.

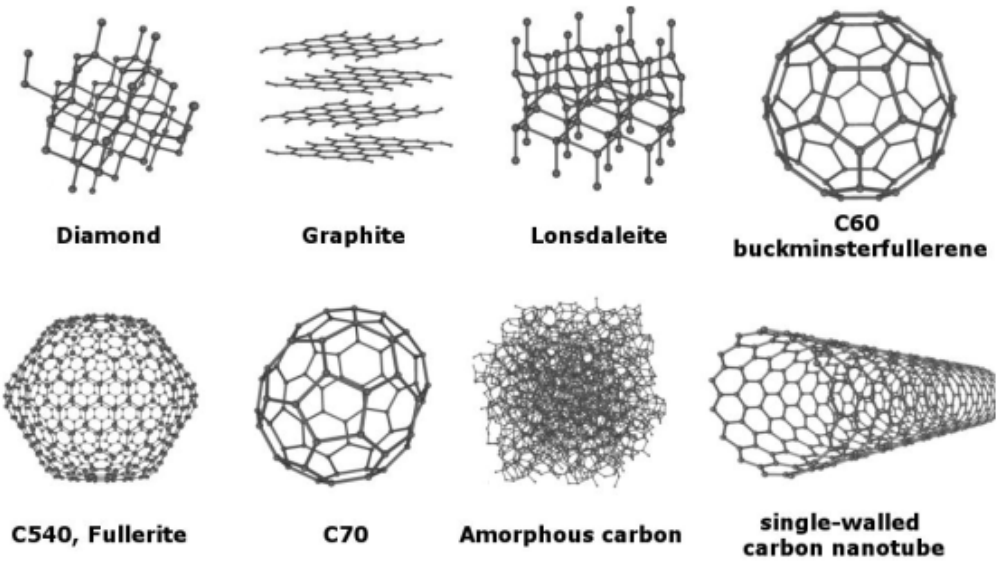

Figure 1-1: Allotropes of carbon [3]

Due to its abundance, electrical conductivity, strength, chemical bonding flexibility, and stability; carbon is a valuable material for a wide variety of applications. Additionally, the ability to engineer porosity of carbon enhances the diversity of possible applications.

Classification of pores in a material are defined by pore size. International Union of Pure and Applied Chemistry (IUPAC) distinguishes pores as macropores, mesopores, and micropores as summarized in Table 1-1. Pores of different classes can exist in a material.

Table 1-1: IUPAC pore classification [4]

IUPAC Pore Class	*Pore size (nm)*
Micropores	< 2
Mesopores	2-50
Macropores	> 50

Carbon and carbonaceous materials have emerged as not only valuable catalyst supports but also active catalysts themselves. Unique physical and chemical properties of carbonaceous materials makes them highly versatile for numerous applications. The wide variety of carbon-based materials offers an attractive opportunity for improving reaction kinetics and selectivity, ultimately contributing to greener and more efficient chemical processes. Forms of carbon suitable for catalytic utilizations include but are not limited to graphene, carbon nanotubes (CNTs), and activated carbon.

Activated carbon, a porous medium formed by carbon atoms, can be produced from fossil fuel-based (coal, petroleum, lignite, etc.) and biomass-based (nut husks, wood, livestock waste, etc.) resources [5–7]. The term "*activated*" refers to the process during which properties of the carbon-rich material are engineered to form an effective adsorbent. The activation process can be done thermally or chemically. In thermal activation process, first a char is produced by pyrolysis of carbon-rich material. The char is then exposed to an oxidizing atmosphere such as carbon dioxide or steam at high (800-1000 ºC) temperatures [8–10]. Chemical activation requires impregnation of the carbon-rich material with oxidizing chemicals like phosphoric

acid and potassium hydroxide and heating at 400-800 ºC [8,11]. At the end of the activation process, new pores and vessels are formed on the carbon due to the removal of some individual carbon atoms, which creates a more porous structure [10,12]. Activated carbons stand out for their vast surface area thanks to their exceptionally porous structure. Combined with their other valuable qualities like stability, low cost, and ease of production it makes activated carbons one of the most frequently used supports for heterogeneous catalysis [5,6]. They expedite the adsorption-desorption processes in catalytic reactions by serving as effective adsorbents for reactants and by-products [13,14].

Graphene is a two-dimensional, single-atom-thick layer of carbons [15,16]. It has exceptional properties that have attracted the attention of scientists since its isolation from graphite in 2004 [17]. It has superior conductivity, strength, and electron mobility [18,19]. There are several methods to synthesize graphene. The original method is the mechanical cleavage method, where graphene is isolated by peeling layers of graphite with an adhesive tape. This method produces high-quality graphene; however, it is only feasible for small-scale synthesis [17,20]. Electrochemical exfoliation is another method to synthesize graphene by graphite. In this method, graphite is placed in an electrochemical cell filled with electrolytes. Constant current in the cell followed by centrifuge and washing forms stable graphene [18,21]. Graphene can also be synthesized from non-graphitic sources. Chemical vapor deposition (CVD) is an example of such. The CVD method operates by decomposing a precursor, commonly gaseous methane, and their diffusion on a catalyst surface where adsorbed species undergo a catalytic reaction to form graphene layers. Non-carbon species present in the precursor gas, like hydrogen, later desorbs from the surface [22–24]. Graphene applications include composite materials [25,26], and supercapacitors [27,28]. Also, the high surface area of graphene, as well as the increased electron mobility and chemical stability, make it an ideal material for catalysis applications. The higher number of active sites on the graphene surface due to its two-dimensional structure promotes faster reactions [29,30].

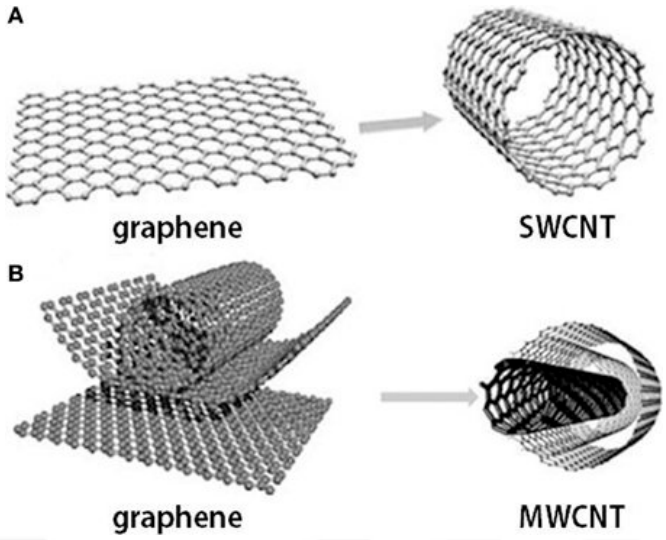

Figure 1-2: Graphene and carbon nanotubes (A) single-walled carbon nanotube (B) multi-walled carbon nanotube [31]

Carbon nanotubes are nano-scale cylindrical structures of carbon atoms arranged in hexagonal lattices. They are basically graphene sheets rolled up in a hollow cylindrical shape in single wall (SWCNT) or multi wall (MWCNT) configurations as illustrated in Figure 1-2 [32–34]. CNTs have a wide range of remarkable properties, including excellent electrical and thermal conductivity, mechanical strength, and stability [35,36]. Various pathways can be followed for the synthesis of CNTs. The three main methods are chemical vapor deposition (CVD), arc discharge, and laser ablation. The most common CVD method requires the transmission of a hydrocarbon vapor through a tubular reactor containing a transition metal catalyst at elevated temperatures. In time, carbon is decomposed on the catalyst and CNTs are formed. This method makes it possible to produce CNTs at low cost and large scales [35,37]. The arc discharge method uses graphite electrodes under an inert atmosphere to form an arc. With electric current under high temperatures, a plasma is formed, which helps deposition of carbon on the electrodes, forming CNTs [35,38,39]. The laser ablation method aims to vaporize atoms of a solid carbon target by the high energy supplied by a laser light in the presence of a catalyst under an inert atmosphere. As the forming vapor cools down, carbon atoms condense and form CNTs [39]. CNTs have a wide range of applications in various fields, such as

biomedicine [32], batteries [40,41], and purification technologies [42]. In catalysis, the tubular structure of CNTs provides a confined environment for the catalytic reactions. This confined environment promotes mass transport and enables efficient reactant diffusion, leading to higher selectivity [43–45].

Despite the promising properties of materials like activated carbon, carbon nanotubes, and graphene, they entail intricate and energy consuming production processes. They sometimes require chemicals and high temperatures, ultimately contributing to carbon emission. Therefore, using inherently energy efficient and environment friendly materials is more advantageous in terms of both cost and environmental impact.

1.1.1 Biomass and Biochar

Biomass, the organic materials sourced from living organisms, has been utilized by humankind for hundreds of thousands of years. Before the discovery of fossil fuels or modern energy sources such as wind or solar radiation, society relied on wood, manure, crop residues, and peat for the energy requirement [46]. Figure 1-3 shows the significant increase in fossil fuel consumption as an energy source since the 19th century. Although they have high calorific values, fossil fuels are the prevalent cause of greenhouse gas emissions [47–49]. Additionally, they are scarce resources and dependence on them is not sustainable in the long term. These drawbacks paved the way for a shift to traditional energy sources, particularly, biomass.

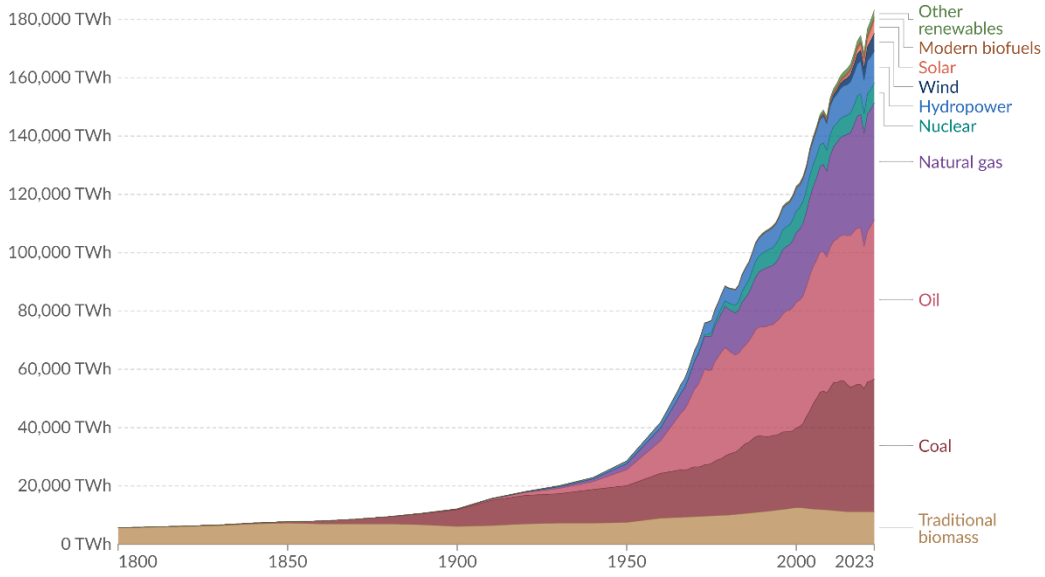

Figure 1-3: Global primary energy source [50]

Biochar is the product obtained when biomass goes through thermal decomposition at elevated temperatures under finite oxygen containing atmosphere. Along with biomass, biochar has been used by humankind for a long time. High fertility of *terra preta* soil of Amazon basin is attributed to the high biochar content in the region, dating back to 5th century, BC [51,52]. There are also reports of biochar usage for body preservation in tombs in Ancient China [53]. Furthermore, biochar is known to be an effective and cheap adsorbent for various applications [54,55]

Traditionally, wood based biomass was the main source for biochar [56]. In time, increasing demand for alternative sources and waste management requirement shifted the interest to agricultural resdiues, manure, and food waste. The limited amount of oxygen during pyrolysis ensure the fixation of carbon in solid form within the char. This makes biochar a sustainable carbonaceous material. Besides, this process provides a sustainable mechanism for waste management by transforming waste and residues to value added products.

1.1.2 Rice Husk and Rice Husk Ash

When the *Oryza sativa* plant is harvested, it yields grains known as rough rice or rice paddy. A rice paddy consists of a non-bounding, stiff outer layer, which is commonly referred to as rice husk or rice hull. When rice husk is separated, remaining grain is known as brown rice, which contains a brownish middle layer called the rice bran, and the centre piece, rice. Rice and rice bran can further be separated by milling [57–59]. Figure 1-4 shows the separate parts of the plant *Oryza sativa*.

Rice husk forms 20-25% of the rice paddy by weight [60–62]. In 2023, total rice production throughout the World surpassed 500 million tonnes [63]. This equates to by-production of more than 100 million tonnes of rice husk, which might have severe effects on the environment unless proper utilization is ensured. In underdeveloped regions, rice husk is most commonly disposed to rivers and farmlands. Accumulation of waste rice husk is a serious threat to soil and water quality. Low nutritional value and difficulty in digestion by animals eliminates its utilization as livestock food and non-controlled decomposition in the nature [64–66]. Rice husk is mainly comprised of cellulose and lignin, and the rest is organic matters and mineral ash [67]. When rice husk goes through pyrolysis, during which it loses roughly 80% of its weight, the resulting product is referred to as rice husk ash, as shown in Figure 1-5.

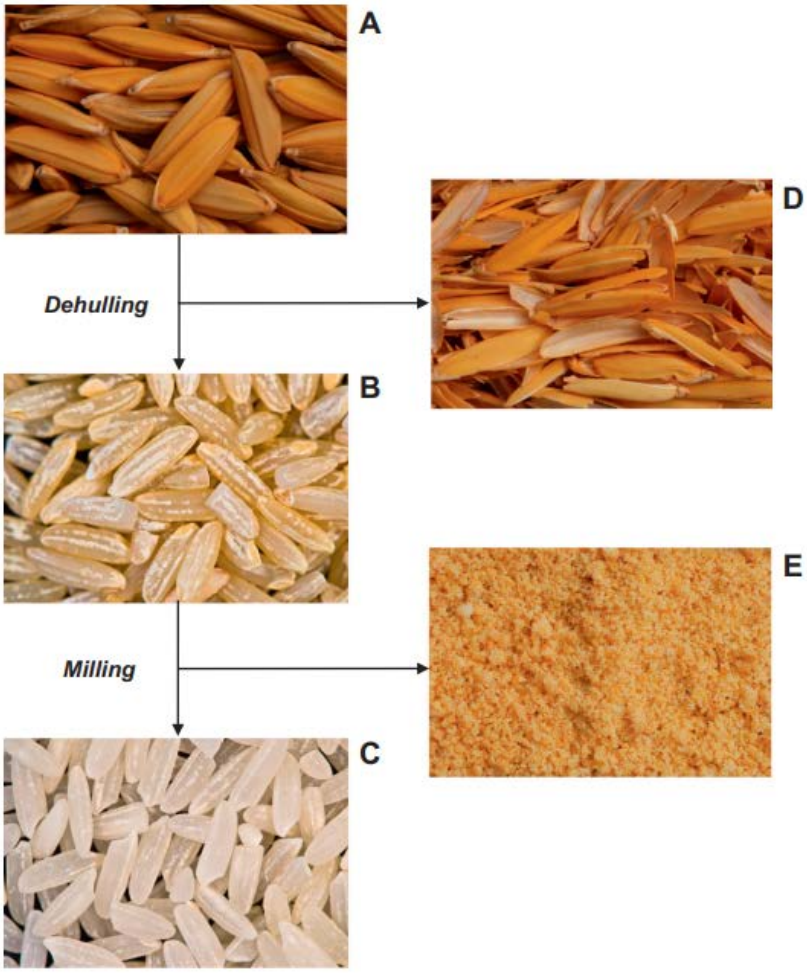

Figure 1-4: Rice paddy and its parts. (A) Rice paddy, (B) Brown rice, (C) Rice, (D) Rice husk, (E) Rice bran [57]

Figure 1-5: Rice husk ash

Rice husk ash has a very high silica content that is generally above 90%. Rest is the residual carbon structure and trace alkali elements [64,67–69]. RHA is a highly porous material with a high specific surface area, low bulk density and a rigid structure [64]. These properties make rice husk ash a highly sought after material in several industries, serving a wide range of purposes. Proper utilization of rice husk and its ash have been studied extensively worldwide. Some promising applications of rice husk and its ash include but are not limited to industrial fuel [70–72], a silica source for ceramics [73,74], zeolites [75–79], and glassware [80,81], and as a concrete filler [82–84].

1.2 Rice Husk Ash as an Adsorbent, and Catalyst Support

In the literature, several studies reported rice husk ash to show great performance as an adsorbent [85–89] and a catalyst support [90–93]. Various aspects of rice husk ash contributes to that success. Stability and content of rice husk ash lays the foundation for its potential usage as an adsorbent, but, in addition to those, structural properties of rice husk ash also stand out amongst a plethora of biochars.

Hierarchical porosity is a structure that consists of pores of different sizes interconnected within the material in a branched configuration. It provides an easier mass transfer, higher strength, and an immensely enhanced surface area [94–96]. Inevitably, such properties are quite attractive for catalytic applications. Hitherto, many methods are developed for synthesis of hierarchically porous materials. Surfactant templating, sol-gel controlling, and supercritical fluid processing are only a few examples of those [95]. The most significant drawback of hierarchically porous material synthesis methods lies in their substantial demand for resources and energy. Evolution always favors the most efficient and adaptable. Consequently, a structure as sophisticated as hierarchical porosity is often found in natural systems. For instance, vascular systems, leaves, and respiratory system [94–97].

In the scope of this work, rice husk ash, a natural, hierarchically porous material was studied. Flame and solar pyrolyzed rice husk ash samples were thoroughly characterized and their performance as adsorbent for gas and liquid phase, and as a support material for palladium catalysts were investigated.

CHAPTER 2

MATERIALS AND METHODS

2.1 Materials

2.1.1 Rice Husk

Rice husk was obtained from Silo Gıda Pirinç Tarım Sanayi of Edirne, Türkiye.

2.1.2 Rice Husk Ash

Rice husk ash was produced by flame, and solar pyrolysis methods. No further treatment was applied on rice husk ash samples unless otherwise stated.

2.1.3 Rice Husk Ash Supported Palladium Catalyst

0.5% Pd/RHA samples were prepared by Melis Yarar of Uner Research Group. Incipient wetness method was used for preparation using $Pd(NO_3)_2$ solution [98].

2.1.4 Reactive Black 5 (RB5)

Reactive black 5 used for liquid phase adsorption experiments was a DyStar Remazol Black B 133% dye.

2.2 Pyrolysis Methods

Solar pyrolysis was applied in our laboratory. Flame pyrolysis was applied by Silo Gıda Pirinç Tarım Sanayi by a method that was kept confidential.

2.2.1 Solar Pyrolysis

Rice husk samples were encased in aluminum foil, and placed in the focus point of the homemade concave mirror system shown in Figure 2-1. Samples were exposed to concentrated solar energy for a duration of 2-20 minutes. In the end, aluminum foils were carefully removed and rice husk ash samples were collected.

Figure 2-1: Homemade concave mirror system used for solar pyrolysis method.

2.2.2 Flame Pyrolysis

Flame pyrolysis was made by Silo Gıda Pirinç Tarım Sanayi in a temperature level of roughly 1000ºC. 5 different batches of flame pyrolyzed rice husk ash was obtained. These sample will be referred to as flame pyrolyzed rice husk ash or FP-RHA from this point onwards. Different batches of samples were indicated by different letters (e.g., FP-RHA-A).

2.3 Characterization Methods

X-Ray diffraction (XRD) crystallography, scanning electron microscopy (SEM), Brunauer-Emmett-Teller (BET) surface analysis, nuclear magnetic resonance (NMR) spectroscopy, electron spin resonance (ESR) spectroscopy, temperature programmed reduction (TPR), Raman spectroscopy, thermal gravimetric analysis (TGA), Fourier-transform infrared (FTIR) spectroscopy, adsorption calorimetry, and ultraviolet visible (UV-Vis) spectroscopy techniques were used for qualitative and quantitative analysis of the materials.

2.3.1 X-Ray Diffraction (XRD) Crystallography

X-ray diffraction crystallography is a non-destructive technique that is used for structural analysis of predominantly crystalline or semi-crystalline materials. It can be used to determine crystalline or atom structure, phase purity, and composition of a material. A crystal is a three-dimensional object whose atoms are in a highly ordered structure in all directions [99]. When a crystalline particle is exposed to X-ray beams, atoms of the particle cause scattering of X-rays in various directions at angle θ, known as the diffraction angle. Scattered beams inevitably interfere in either destructive or constructive manner as in Figure 2-2. If the latter occurs, they form a new beam, which has a higher amplitude at the particular diffraction angle [99,100].

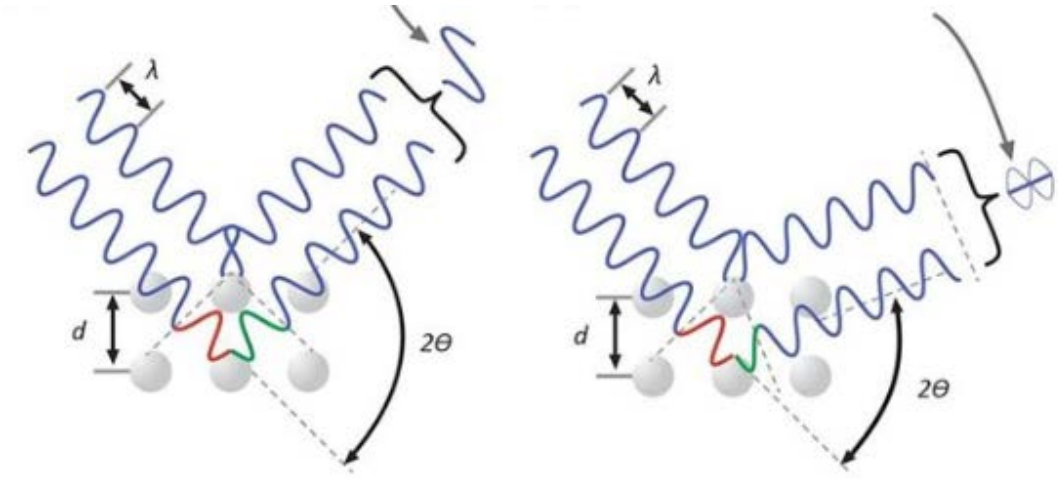

Figure 2-2: Constructive (left) and destructive (right) interference of X-ray beams [101]

Bragg's law in 2-1 relates the specific diffraction angle at which constructive interfernce occurs to the planar distance between the atomic planes, where λ is the wavelength of the X-ray beam, θ is the diffraction angle, d is the planar distance, and n is the order of reflection.

$$sin\theta = \frac{n\lambda}{2d} \qquad 2\text{-}1$$

Results of X-ray diffraction analysis are reported as an XRD pattern where intensity of a signal is plotted against 2θ. A typical XRD pattern is given in Figure 2-3. Scherrer equation in 2-2 relates crystal size to the broadening of a peak in XRD pattern. Here, τ is the average crystallite size in nm, K is dimensionless shape factor (K=0.9), λ is x-ray wavelength (0.154 nm), β is full width at half of maximum intensity in radians, and θ is Bragg angle in radians [102,103]

$$\tau = \frac{K\lambda}{\beta cos\theta} \qquad 2\text{-}2$$

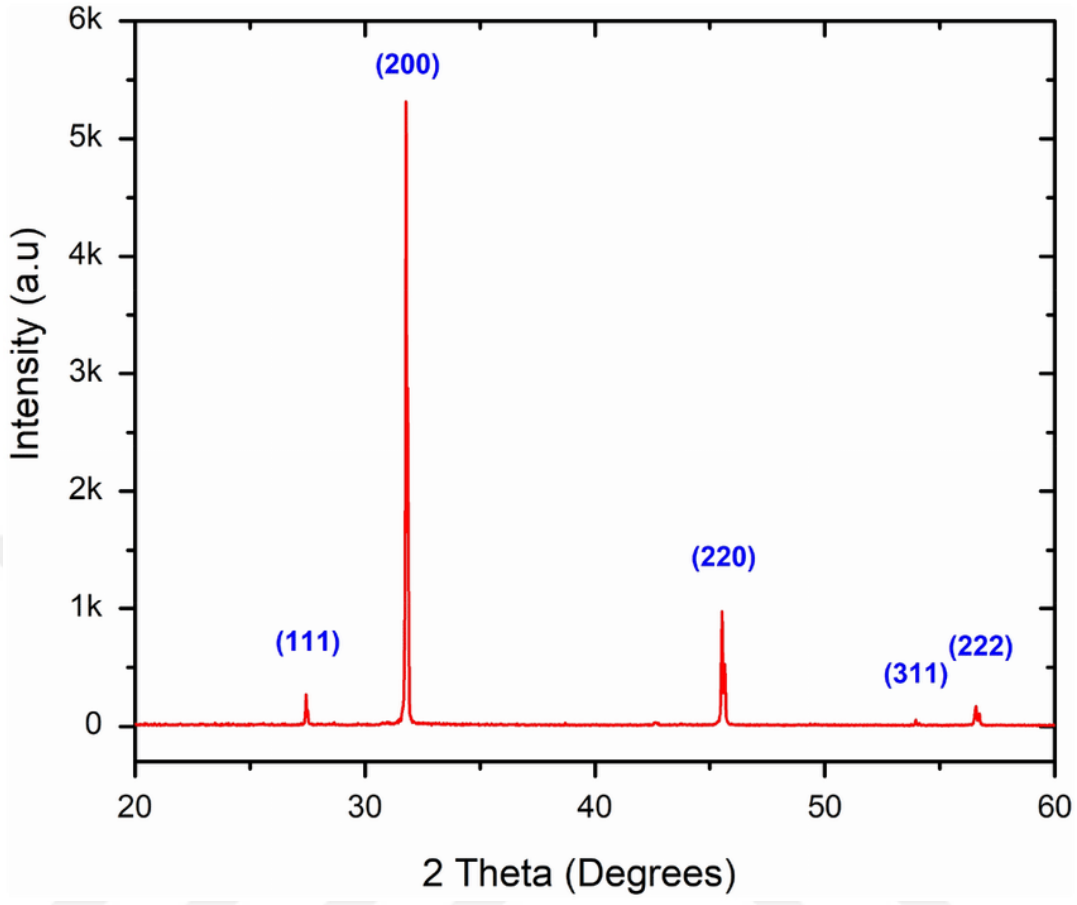

Figure 2-3: XRD pattern of sodium chloride [104]

20-minute solar pyrolyzed rice husk ash was subjected to powder X-Ray Diffraction (XRD) analysis with a Rigaku Ultima-IV X-ray diffractometer with a scan speed of 5º/min between 5-90º.

2.3.2 Thermal Gravimetric Analysis (TGA)

Thermal gravimetric analysis is used to obtain data on thermal stability and reaction kinetics of a material under controlled atmospheric conditions by measuring the changes in its mass during heating, cooling or keeping at a constant temperature of selection [105]. Mass change can be observed in occurrence of vaporization, sublimation, adsorption, absorption, or chemical reactions such as oxidation or reduction, depending on the material, temperature, and atmosphere. Thermal

gravimetric analysis help identifying the events occuring at certain temperatures as well as quantitative analysis by changes in the mass [106].

Results of the analysis are reported in the form of thermogravimetry curve. It simply represents the change in the mass as a function of temperature or time. A typical thermogravimetry curve is shown in Figure 2-4.

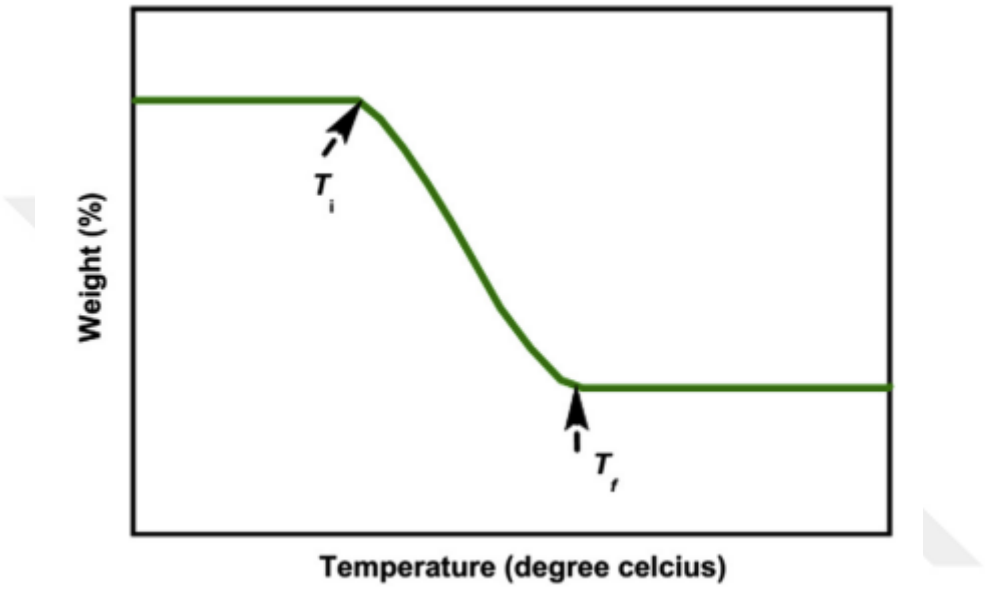

Figure 2-4: Typical thermogravimetry curve [105]

Thermal gravimetric analysis is crucial to investigate thermal stability of a material since it directly reports if a material can withtand high temperatures.

Thermal gravimetric properties were investigated with a Shimadzu DTG – 60H Thermogravimetric Analyzer equipment where sample was heated from room temperature to 800ºC with a heating rate of 10 ºC/min under constant air flow.

2.3.3 Brunauer-Emmett-Teller (BET) Surface Analysis

BET surface analysis method uses the BET theory, developed by Stephen Brunauer, Paul Hugh Emmett, and Edward Teller in 1938 [107]. It is an extensive study based on Langmuir adsorption model describing monolayer adsorption on a solid surface.

Langmuir's model have some fundamental assumptions such as adsorption only occurs as a single layer, all sites present on the solid surface are identical and each can hold only one adsorbate molecule, and the adsorbate molecules do not interact with each other [108].

BET theory extends Langmuir Theory by acknowledging the multilayer adsorption of molecules as illustrated in Figure 2-5. BET method defines adsorbate amount as a function of relative pressure within the system. 2-3 is used for the analysis where v is the adsorbate amount at pressure p, v_m is the volume of adsorbate at complete monolayer coverage, and c is the constant equal to $e^{\frac{E_1-E_l}{RT}}$ where $E_1 - E_l$ is the difference between heat of adsorption of the first layer and the heat of liquefaction, or heat of adsorption of the second and latter layers [107].

$$\frac{p}{v(p_0-p)} = \frac{1}{v_m c} + \frac{c-1}{v_m c}\frac{p}{p_0} \qquad 2\text{-}3$$

Plot of $\frac{p}{v(p_0-p)}$ against $\frac{p}{p_0}$ gives a straight line in a $\frac{p}{p_0}$ range of 0.05 and 0.35 with the intercept $\frac{1}{v_m c}$ and slope $\frac{c-1}{v_m c}$, which eases the calculation of v_m and c.

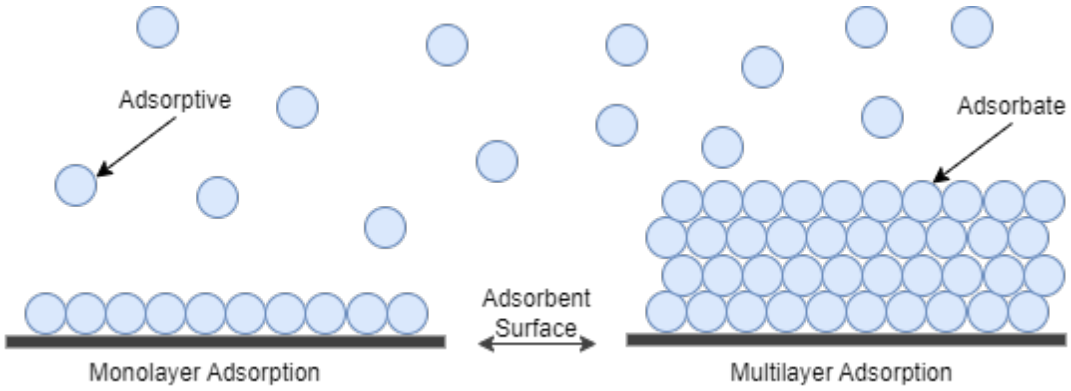

Figure 2-5: Monolayer and multilayer adsorption

Nitrogen at 77 K is the most commonly used adsorptive for the BET method. At this temperature, it has a cross-sectional area of 0.162 nm^2. This value is accepted as the average area occupied by each nitrogen molecule that sums up to a volume of v_m. Then, multiplication of the average area by the number of molecules adsorbed at a

complete mnolayer coverage gives the surface area of the adsorbent. Method is illustrated in Figure 2-6

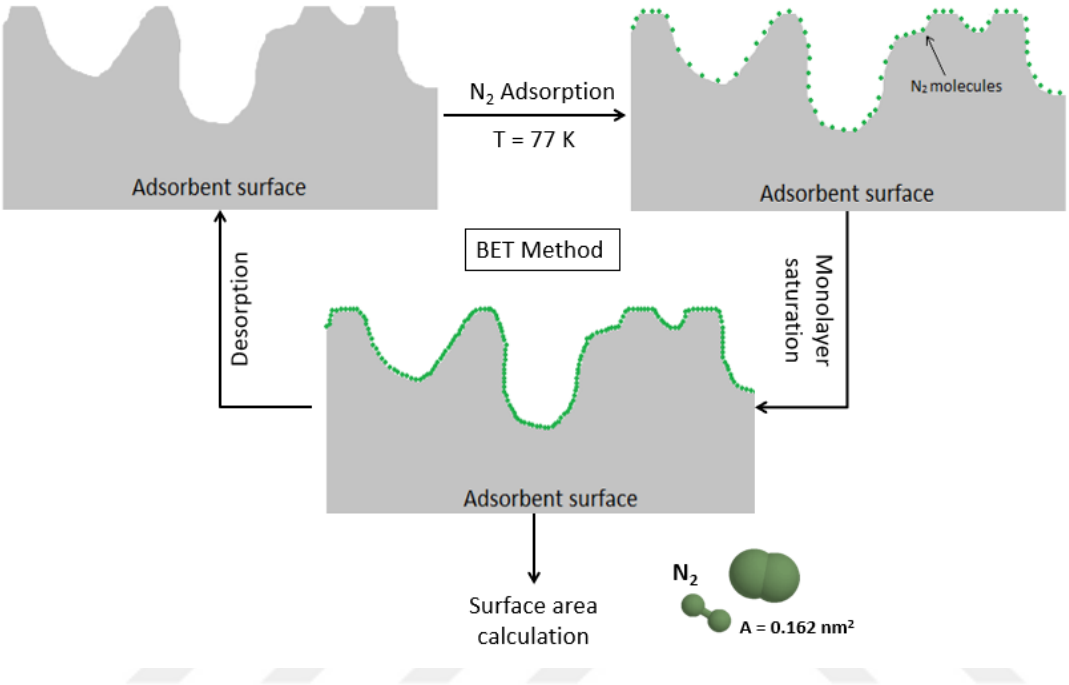

Figure 2-6: BET Method by nitrogen adsorption

Porous properties were measured by Brunauer-Emmett-Teller (BET) method at 77.3 K by nitrogen adsorption using the surface area and porosity system Micrometrics TriStar II 3020 after degassing the sample at 200°C for 6 hours.

2.3.4 Scanning Electron Microscopy (SEM)

The traditional optical microscopy uses visible light to observe a sample, much like a magnifying glass. A scanning electron microscope, on the other hand, differs from basic optical microscopy by its dependence on highly focused electron beams under vacuum conditions to scan the surface of the specimen [109]. If the sample has poor electrical conductivity, a thin metallic film coating is applied to create a conductive layer of the surface. The image is created by the information carried by the electrons

back-scattered from the sample surface. This method provides high-resolution images of the samples that makes it possible to have a detailed morphology and sizing analysis of the sample [110].

Morphological properties were investigated with a TESCAN-VEGA 3 Scanning Electron Microscope after the sample surface was coated with gold and palladium or copper by sputtering.

2.3.5 Raman Spectroscopy

Raman spectroscopy is a strong tool to obtain information on molecular and structural composition of materials. It is a non-destructive tool used for the characterization of crystalline, nanocrystalline, amorphous carbons, and many other materials [111]. Raman spectroscopy requires a light source (such as a laser), a spectrometer and a detector. When a sample is illuminated with laser, majority of the photons are scattered without energy exchange, known as Rayleigh scattering. However, a small fraction of photons interacts with molecular vibrations, resulting in a shift in their energy, resulting in "*Raman scattering*". This shift is a characteristic property, unique to each molecule, and can be used for identification and analysis of the given material [112,113]. Raman spectroscopy is both qualitative and quantitative. Qualitative analysis can be performed due to the characteristic "*Raman shift*" of different molecules and structures. Quantitative analysis can also be performed since intensity of the Raman scattering is directly proportional to number of molecules [114].

Raman spectroscopy is a widely used characterization method in catalysis since it is suitable for in-situ studies, i.e., analysis can be performed under reaction conditions. Also, common supports such as silica or alumina are weak Raman scatterers and hence, does not interfere with the results [111]. Raman spectroscopy is particularly sensitive to carbon-carbon bond vibrations. Therefore, it is indispensable for characterization of carbonaceous materials. An important feature of Raman

spectroscopy is that it can differentiate G and D bands of carbon, which have distinctive vibrational frequencies [115].

G-band is observed in graphitic carbon structures where carbon atoms move in graphene plane, known as the E_{2g} mode of vibration. It appears on a vibrational frequency level of around 1600 cm^{-1}. D-band is associated with the disorder, defects, and edges in carbon structure. These types of carbon have non-planar vibration modes known as A_{1g} mode of vibration and observed at around 1350 cm^{-1} frequency level. E2g and A1g modes of vibration are illustrated in Figure 2-7.

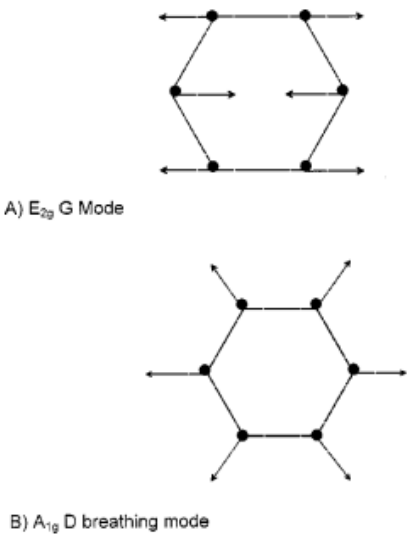

Figure 2-7: E_{2g} (Planar) and A_{1g} (non-planar) modes of vibration [112]

Degree of disorder which is proportional to the amount of D-band carbon within the sample is defined as the intensity ratio of D-band to G-band [116–118]. Degree of disorder have significant impact in catalysis since it is directly related to number of active sites in a catalytic material. Controlling the degree of disorder can create catalysts with higher number of active sites to increase activity.

Raman spectra of the samples were recorded on a Renishaw In Via Raman Microscope with a 532 nm laser by the Central Laboratory of Middle East Technical University. Spectral deconvolution was applied by OriginLab software where D and G bands were quantitatively analyzed for their integrated intensities. A sample

deconvoluted Raman spectrum can be seen in Figure 2-8. Here, the area under the D and G bands are calculated by the software. Degree of disorder can be found by the ratio of the former to the latter. Procedure for peak fitting was described in Appendix A.

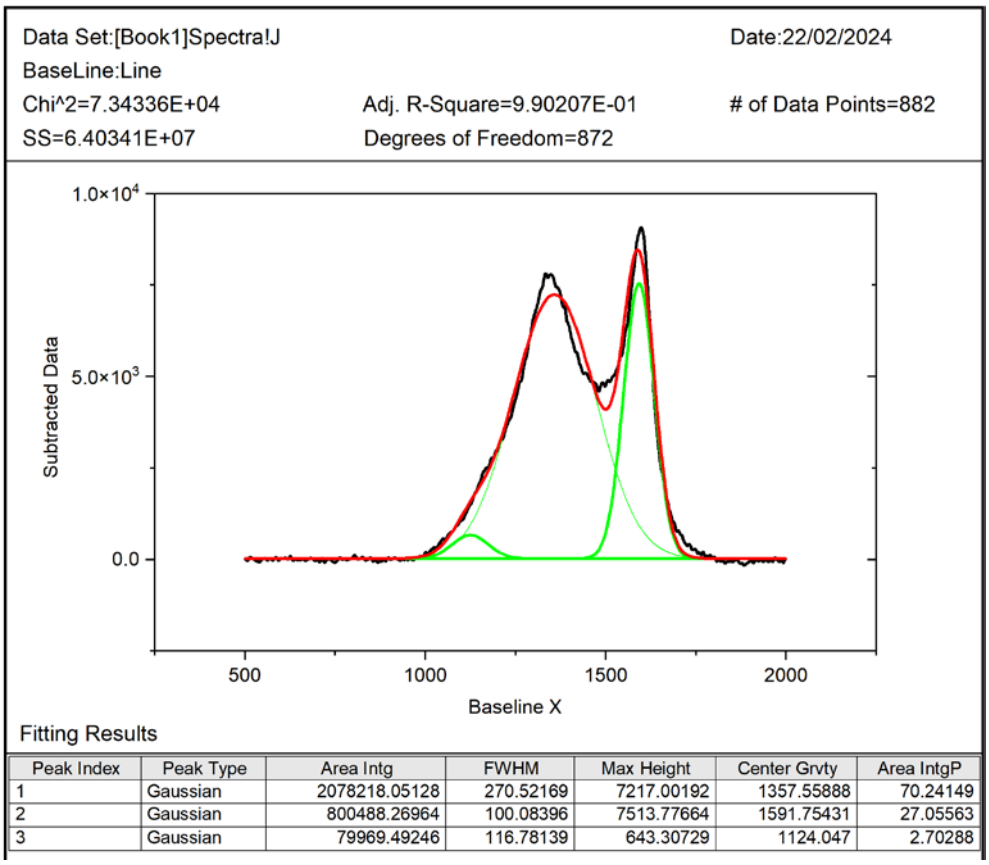

Fitting Results

Peak Index	Peak Type	Area Intg	FWHM	Max Height	Center Grvty	Area IntgP
1	Gaussian	2078218.05128	270.52169	7217.00192	1357.55888	70.24149
2	Gaussian	800488.26964	100.08396	7513.77664	1591.75431	27.05563
3	Gaussian	79969.49246	116.78139	643.30729	1124.047	2.70288

Figure 2-8: Deconvoluted Raman spectrum for SP-RHA-01

2.3.6 Electron Spin Resonance (ESR) Spectroscopy

Electron spin resonance (ESR) spectroscopy, also called electron paramagnetic resonance (EPR) spectroscopy, is used to study materials containing unpaired electrons. If an external magnetic field applies to a material, paramagnetic centers experience “Zeeman Splitting” due to splitting of the spectral lines as illustrated in Figure 2-9. Energy level is explained by 2-4 where μ_B is Bohr Magneton in J/T, B is

magnetic field strength in T, m_s is spin quantum number, and g is the dimensionless g-factor specific to different paramagnetic species.

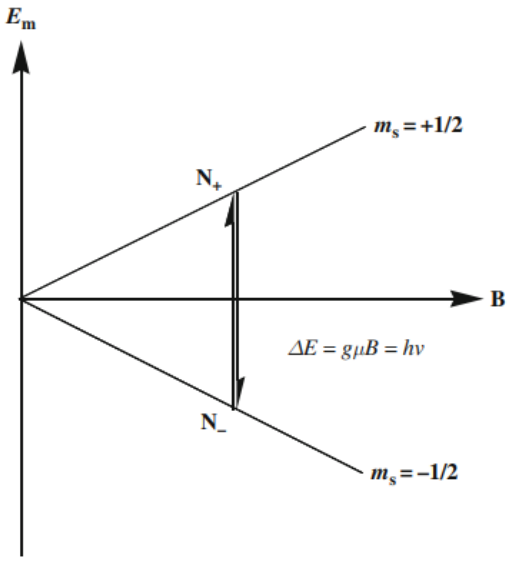

Figure 2-9: Zeeman Splitting [119]

$$E_m = g\mu_B B m_S,\ m_S = \pm 1/2 \qquad 2\text{-}4$$

In ESR spectroscopy, paramagnetic centres in the materials containing unpaired electrons are exposed to an external magnetic field of changing strength. When strength of the magnetic field matches to the frequency of unpaired electrons, resonance occurs, and a signal is produced due to absorption of microwave irradiation [119]. This signal is known as the absorption spectrum as shown in Figure 2-10. The ESR spectrum is generally reported as the first derivative of the absorption spectrum as shown in Figure 2-11. The g-factor corresponds to the point where absorption spectrum reaches its peak or ESR spectrum becomes zero.

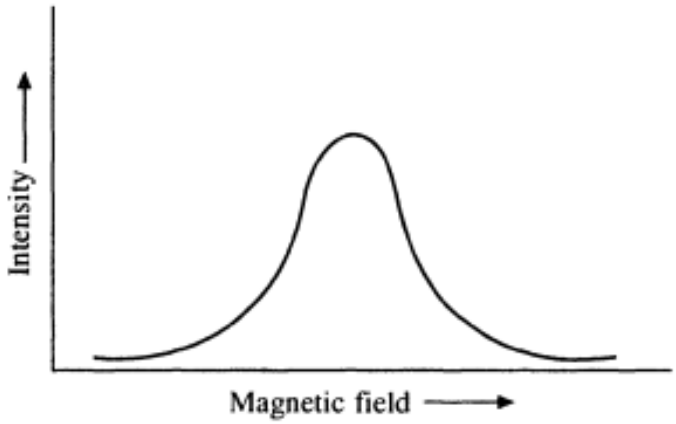

Figure 2-10: The absorption spectrum [120]

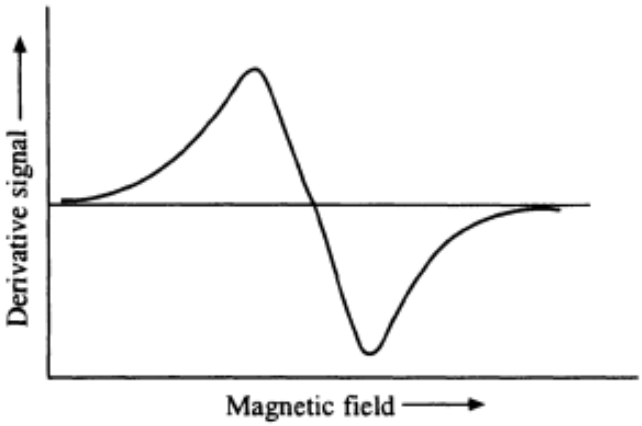

Figure 2-11:First derivative of the absorption spectrum, ESR spectrum [120]

Energy difference between two Zeeman levels is given by the equation $\Delta E = g\mu_B B$. g-factor then can be calculated from 2-5 where h is Planck's constant and v is microwave frequency. Under vacuum conditions, a free electron has a g-factor of 2.00232 [121].

$$g = \frac{\Delta E}{\mu_B B} = \frac{hv}{\mu_B B} \qquad 2\text{-}5$$

ESR analyses were completed with a benchtop Bruker MicroESR Spectrometer by placing the samples in 1 mm diameter glass tubes. All spectra were recorded with 25 mW microwave power and 64 scans.

2.3.7 Nuclear Magnetic Resonance (NMR) Spectroscopy

NMR spectroscopy is an exemplary, non-destructive characterization method that utilizes the magnetic properties of the nuclei. Atomic nuclei that has an odd number of protons behaves in a certain way under magnetic field, which gives information on the chemical environment of the analyte [122]. Nuclei of all molecules has an inherent characteristic property called spin, which makes nuclei act in a similar manner to a magnet, resulting in the change of behaviour and creation of different energy states when an external magnetic field is applied. Exposure to radiation in radiofrequency causes transitions between the energy states, similar to that described in Section 2.3.6, which is detected by NMR spectrometer. The changes are then transformed into what is called an NMR spectrum. The frequency of energy state change is specific to the chemical environment of a molecule, which is measured and reported in units of ppm from TMS, referencing a chemical shift from the reference compound, tetramethysilane [123].

A Magritek Spinsolve Benchtop 43 MHz NMR spectrometer in Figure 2-12 was used for the analyses. Experimental procedure was described in Appendix B.

Figure 2-12: Magritek Spinsolve Benchtop 43 MHz NMR Spectrometer

2.3.8 Fourier Transform Infrared (FTIR) Spectroscopy

Fourier transform infrared spectroscopy is a widely used method for molecular composition and structural characterization studies. The principle base of infrared spectroscopy is that molecules have a characteristic infrared radiation absorption range. The absorption only occurs when the molecule bears a change in dipole moment due to its motion, either vibrational or rotational. At the moment where radiation frequency aligns with the vibrational frequency of the molecule, an energy transfer occurs and intensity of the molecular vibration or rotation changes [110].

In the electromagnetic spectrum, infrared spectral regions are divided into three parts. They are tabulated in Table 2-1. Rotational changes require wavelengths of less than 100 cm^{-1}, which lays in the far IR region. They are also very limited in solids and liquids. The vibrational changes, on the other hand, are observed in all phases and have a wide wavelength range of 13000 to 675 cm^{-1}, that is in the near and middle IR region. Absorption radiation range of a majority of organic compounds and inorganic ions are in 4000 – 400 cm^{-1} wavelength range, which makes it the most commonly used range in infrared spectrometers [124]. Vibrational motion in molecules are also distinguished by the type of motion. They are divided into two categories; stretching, which corresponds to a change in bond length, and bending, which corresponds to a change in bond angle. They are further divided into subcategories depending on the direction of movement, all of which have characteristic wavelength ranges in a spectrum [110,125]. Figure 2-13 shows different vibrational moves in a molecule.

Table 2-1: IR spectral regions [110]

Region	**Wavelength Range (cm^{-1})**
Near IR	12800 - 4000
Middle IR	4000 - 200
Far IR	200 - 10

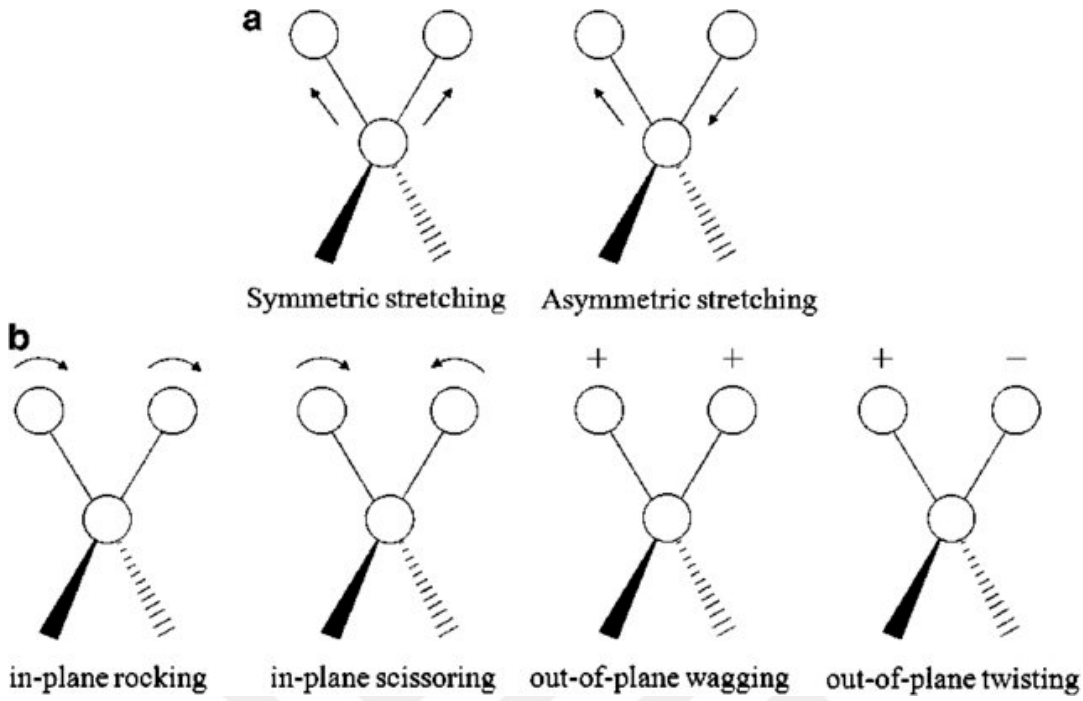

Figure 2-13: Vibrational modes. (a) stretching, (b) bending [126]

An infrared spectrometer consists of a radiation source, an interferometer, which converts the radiation to the time domain, a detector, a signal amplifier, an analog to digital convertor, and a sample compartment. The resulting data is known as an interferogram, which is in time domain. Fourier transform is applied to the interferogram to change the domain back to frequency, and form the IR spectrum. Y-axis of the IR spectrum can be transmittance or absorbance. A sample IR spectrum for caffeine is given in Figure 2-14.

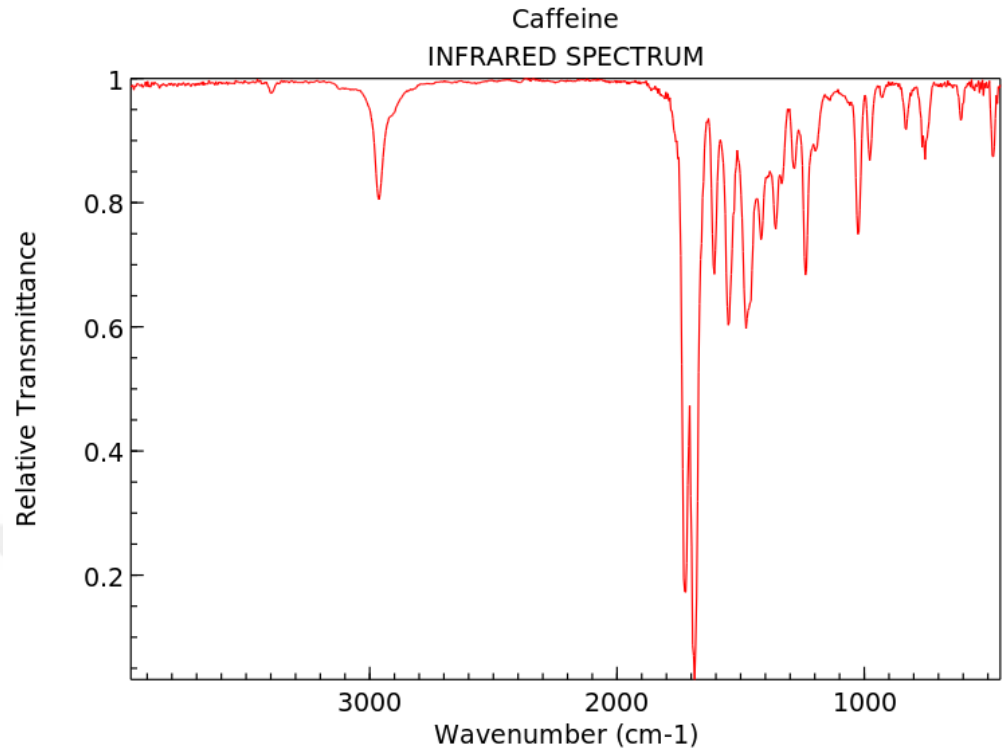

Figure 2-14: IR spectrum of caffeine [127]

Solid rice husk ash samples were analysed with a Perkin Elmer Spectrum Two w/UATR infrared spectrometer without any prior treatment.

2.3.9 Adsorption Calorimetry

A Tian-Calvet calorimeter is a device that consists of a well insulated vessel that is composed of two isolated chambers both of which are surrounded by an array of thermocouples that makes it possible to directly and accurately measure heat flow [128,129].

Adsorption and desorption isotherms were measured by Setaram Tian-Calvet C80 Calorimeter shown in Figure 2-15. A homemade glass manifold was used to connect the sample cell in the calorimeter with a Pfeiffer turbomolecular vacuum pump, a Baratron capacitance pressure sensor, and the adsorptive gas source. FP-RHA-A was used for all gas phase adsorption experiments. Ammonia and carbon

dioxide adsorption isotherms were measured. Prior to the experiments, system was evacuated at 100ºC until heat flow stabilized. Adsorbate amount is measured by changes in the pressure and heats of adsorption were measured by the calorimeter.

Figure 2-15: Calvet Setaram C80 Calorimeter

2.3.10 Ultraviolet-Visible (UV-Vis) Spectroscopy

Absorbance spectrum of a solid or aqueous compound in a wavelength range of ultraviolet and visible region of the electromagnetic spectrum can be measured by UV-Vis spectroscopy. It uses the phenomena that when a light beam is emitted by a compound, a certain fraction of it is absorbed while the rest of it is either reflected or transmitted [110]. The absorption occurs at the wavelength at which the energy of the light beam matches the excitation energy of the electrons within the analyte. The excitation wavelength is used to obtain information on the molecular structure of the compound. Intensity of the absorbance can be directly related to the concentration of the sample, therefore, quantitative analysis is possible [110,130].

Theoretical background for the UV-Vis spectroscopy can be explained by the Beer-Lambert law in 2-6 where A is absorbance, ε is the molar absorptivity that is characteristic to the analyte in units of $M^{-1}cm^{-1}$, c is concentration of the solution in units of M, d is the path length of the sample holder in units of cm. Absorption is defined as a function of transmitted instensity as in 2-7 where I_0 is the incident intensity and I is the transmitted intensity.

$$A = \varepsilon * c * d \qquad \text{2-6 [131]}$$

$$A = log_{10}\left(\frac{I_0}{I}\right) \qquad \text{2-7 [131]}$$

During the analysis, absorbance data is collected and reported as a function of wavelength, referred to as absorption spectrum. A simple illustration of an UV-Vis spectrometer is shown in Figure 2-16.

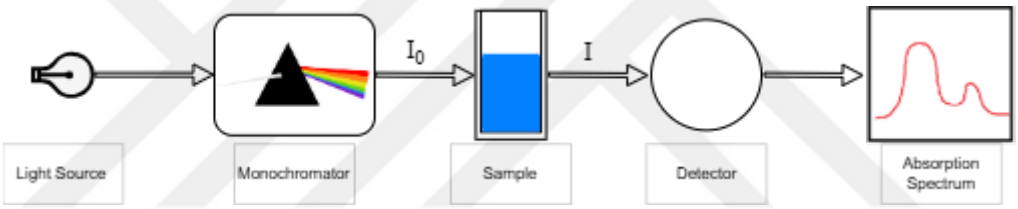

Figure 2-16: Illustration of an UV-Vis spectrometer

In the scope of this work, liquid phase adsorption studies of RB5 on RHA were quantitatively analyzed via UV-Vis spectroscopy. RB5 is a commonly used synthetic textile dye which has reactive groups that form chemical bond with the fiber during the dyeing process [132]. Chemical structure of RB5 is given in Figure 2-17.

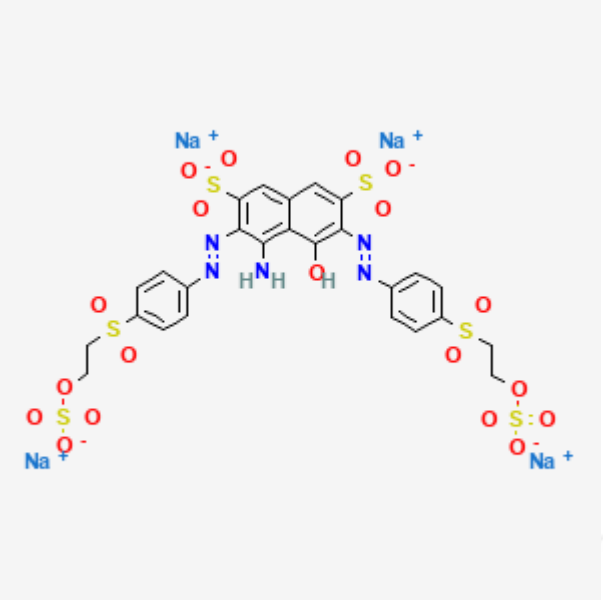

Figure 2-17: Chemical Structure of RB5 [133]

For the experiments, RHA was added to RB5 solutions of different concentrations and decolorization of the solutions were measured by changes in the absorption intensity, as a result of concentration change. A sample UV-Vis spectrum of RB5 is given in Figure 2-18. Here, the peak at ~600 nm is a characteristic of RB5 [134–136] A TG Instruments T80+ UV/Vis Spectrometer was used for the analyses.

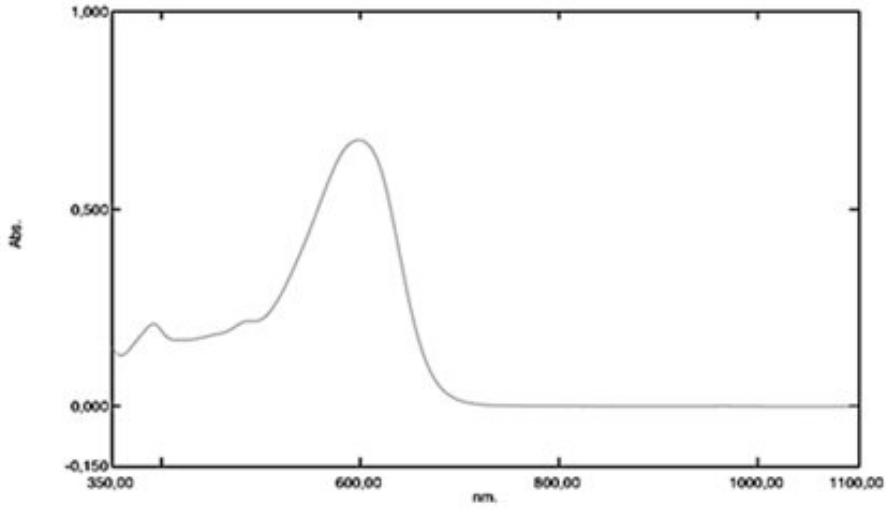

Figure 2-18: UV-Vis absorbance spectrum of RB5 [137]

2.3.11 Temperature Programmed Reduction (TPR)

Temperature programmed characterization techniques gives a highly accurate insight into performance of a material under reaction conditions by qualitatively monitoring the reaction during controlled heating.

0.5% Pd/RHA samples were subjected to temperature programmed reduction analyses under hydrogen flow. Experiments were performed on a Micromeritics ChemiSorb 2750 device. Analyte was positioned between two layers of glass wool in an U-shaped quartz tube reactor to prevent displacement. Before hydrogen flow was started, sample was exposed to helium until thermal conductivity detector signal stabilized. Once stable signal was ensured, hydrogen was introduced to the system at a rate of 25 sccm and heating was started at a rate of 10 K/min up to 1200 K where temperature was kept constant for 15 minutes. Then, system was cooled down to room temperature under helium flow. This procedure was repeated for 5 times.

CHAPTER 3

RESULTS AND DISCUSSION

This chapter presents the results of rice husk ash preparation, characterization, and its utiliziation as an adsorbent, absorbent, and a support for palladium catalysts.

3.1 Preparation

Rice husk and flame pyrolyzed rice husk ash were obtained from Silo Gıda Pirinç Tarım Sanayi. Rice husk was processed by solar pyrolysis using concentrated solar radiation as energy source.

3.1.1 Solar Pyrolysis

Rice husk was exposed to concentrated solar radiation using the homemade mirror system described in Section 2.2.1. Produced chars were used for characterization studies without further treatment unless mentioned otherwise.

To obtain a relation between exposure time and properties of the produced rice husk ash, duration of the pyrolysis was changed in a range 1-40 minutes. Carbon content of the products were plotted against exposure time in Figure 3-1. There is a clear polynomial relation between exposure time and carbon content. It is also clear that after a certain point, pyrolysis duration has minimal effect on carbon content of the sample. Although concentrated solar energy provides more than enough energy for pyrolysis at a greater extent, crystallization of the sample due to sudden temperature increase caused by the sample's exposure to an onslaught of energy might have been a barrier for an extended pyrolysis process.

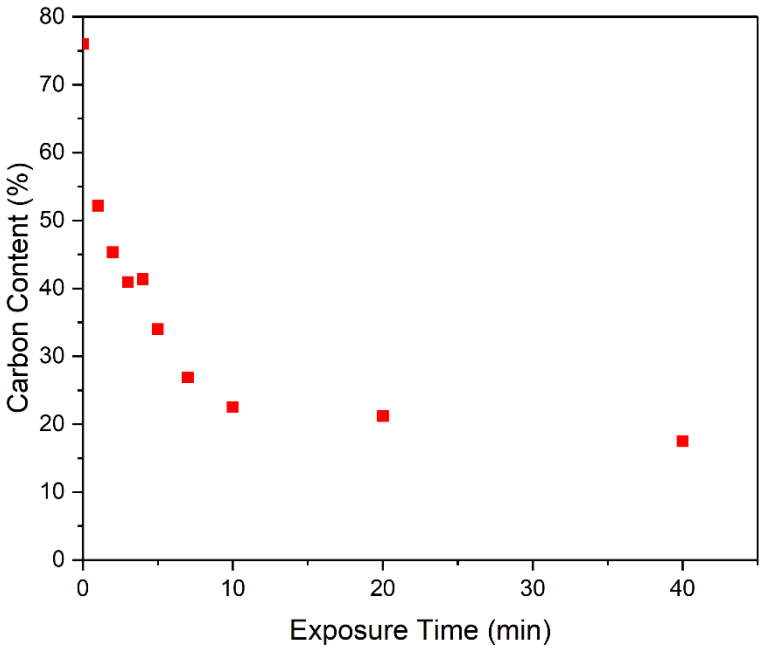

Figure 3-1: Effect of exposure time to carbon content in solar pyrolysis

3.2 Characterization

3.2.1 X-Ray Diffraction (XRD) Crystallography

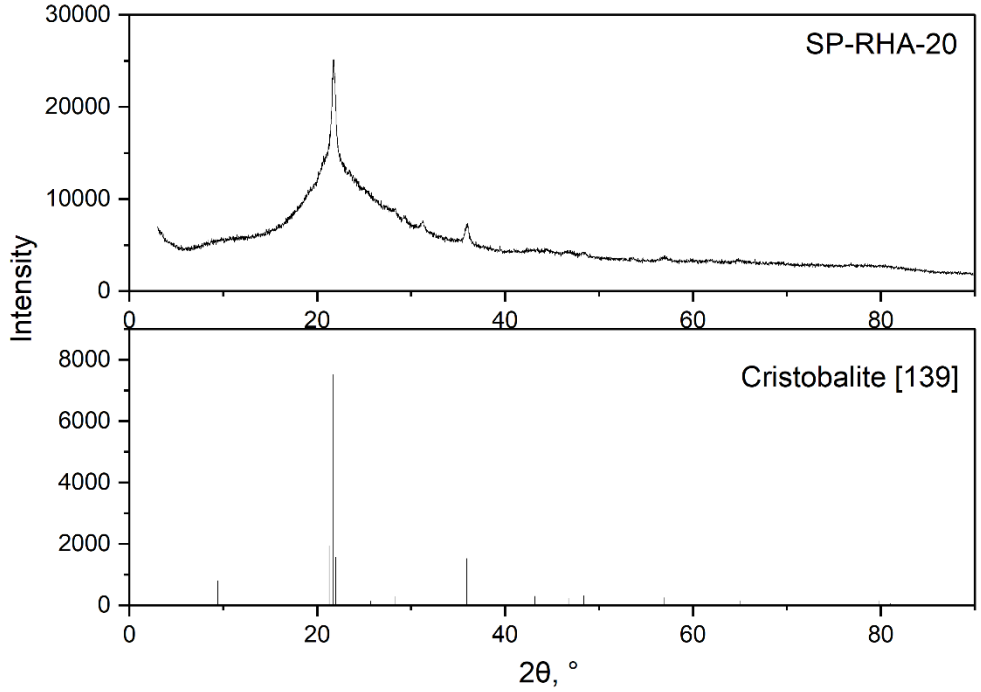

Figure 3-2: XRD pattern of SP-RHA-20 and Cristobalite [138]

Figure 3-2 shows the XRD pattern of 20-minutes solar pyrolyzed RHA sample. Peaks at 2θ= 21.7º and 35.9º are the characteristic peaks of cristobalite, a type of silica mineral [138–140]. Broad linewidth of the pattern indicates the amorph structure of silica. From the Scherrer equation, crystallite size was calculated as 21 nm. Details of the calculation are explained in Appendix C.

3.2.2 Thermal Gravimetric Analysis (TGA)

Upon several thermal gravimetric analyses under air flow; average moisture, combustible material, and ash contents of rice husk, and flame and solar pyrolyzed rice husk ash samples were calculated and given in Table 3-1. TGA profiles of all

samples are given in Appendix D. Regardless of the production method, moisture contents are similar for all samples. Combustible material amount is inversely proportional to pyrolysis duration for the solar pyrolyzed samples. For the flame pyrolyzed samples, contents are mostly similar except for two samples, FP-RHA-C and FP-RHA-E, which have significantly lower combustible content. Remaining ash is considered to be SiO_2 and its derivatives for all samples.

For the combustible material content, flame pyrolyzed samples seem to be non-homogenous since different TGA profiles were observed for different analyses. This might be a result of non-homogenous temperature distribution within the pyrolysis system. In the solar pyrolyzed samples, however, even though samples were thermally analysed only once, results are in good agreement with each other in terms of change of combustible content with pyrolysis duration.

Table 3-1: Thermal gravimetric analysis results

Sample	Content		
	Moisture (%)	Combustibles (%)	Other (%)
RH	10.0	75.8	14.2
FP-RHA-A	2.7 ± 0.4	10.4 ± 0.2	86.9 ± 0.4
FP-RHA-B	2.7 ± 0.3	9.1 ± 0.1	88.2 ± 0.4
FP-RHA-C	2.1 ± 0.5	6.0 ± 0.3	91.9 ± 0.5
FP-RHA-D	4.4 ± 0.8	11.2 ± 0.3	84.4 ± 1.1
FP-RHA-E	1.3 ± 0.1	6.0 ± 0.3	92.7 ± 0.2
SP-RHA-01	3.2	52.2	44.6
SP-RHA-02	2.9	45.3	51.8
SP-RHA-03	3.6	40.9	55.5
SP-RHA-04	3.5	41.4	55.1
SP-RHA-05	4.3	34.0	61.7
SP-RHA-07	4.3	26.9	68.8
SP-RHA-10	2.4	22.5	75.1
SP-RHA-20	3.3	21.2	75.5
SP-RHA-40	6.3	17.5	77.2

3.2.3 Brunauer-Emmett-Teller (BET) Surface Analysis

Specific BET surface area and BJH pore volume obtained by BET surface analysis is tabulated below in Table 3-2 for flame and solar pyrolyzed samples. BET isotherms of all samples are given in Appendix E. Figure 3-3 shows the relation between BET surface area and carbon content of RHA samples. Results clearly indicate carbon content and BET surface area to be directly proportional for solar pyrolyzed samples. Solar pyrolyzed samples have a strongly linear relationship

between BET surface area and carbon content. This paves the way for ease of engineering the porous properties of the sample to tailor the material suitable for the process needs by utilizing concentrated solar energy for pyrolysis.

Pore size distributions were also obtained by BET analysis by BJH adsorption method. Distributions are given in Figure 3-4 and Figure 3-5. Assemblage of pores of different sizes is a direct proof of hierarchical porosity where pores of smaller size form the majority of the surface area, connected by the greater pores of varying sizes. This not only adds to the authenticity of the porosity but also enhances the mass transfer within the material.

Table 3-2: BET surface analysis results

Sample	Specific Surface Area (m^2g^{-1})	Specific Pore Volume (cm^3g^{-1})
FP-RHA-A	57.0	0.04
FP-RHA-B	23.0	0.03
FP-RHA-C	15.7	0.02
FP-RHA-D	18.8	0.02
FP-RHA-E	15.4	0.02
SP-RHA-02	191.3	0.07
SP-RHA-03	169.2	0.06
SP-RHA-04	176.1	0.09
SP-RHA-05	167.9	0.08
SP-RHA-07	147.6	0.08
SP-RHA-10	131.1	0.08
SP-RHA-20	132.7	0.07

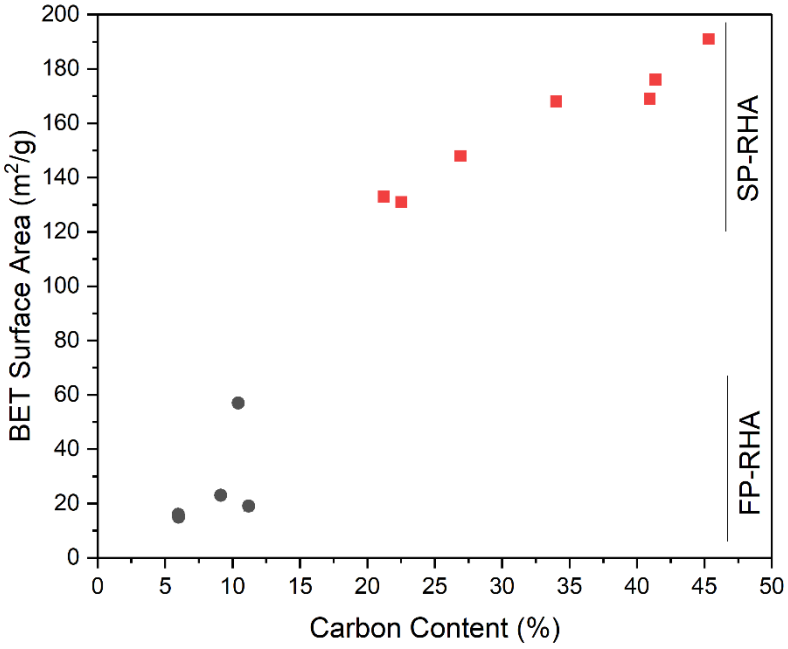

Figure 3-3: Change of BET surface area with carbon content of RHA

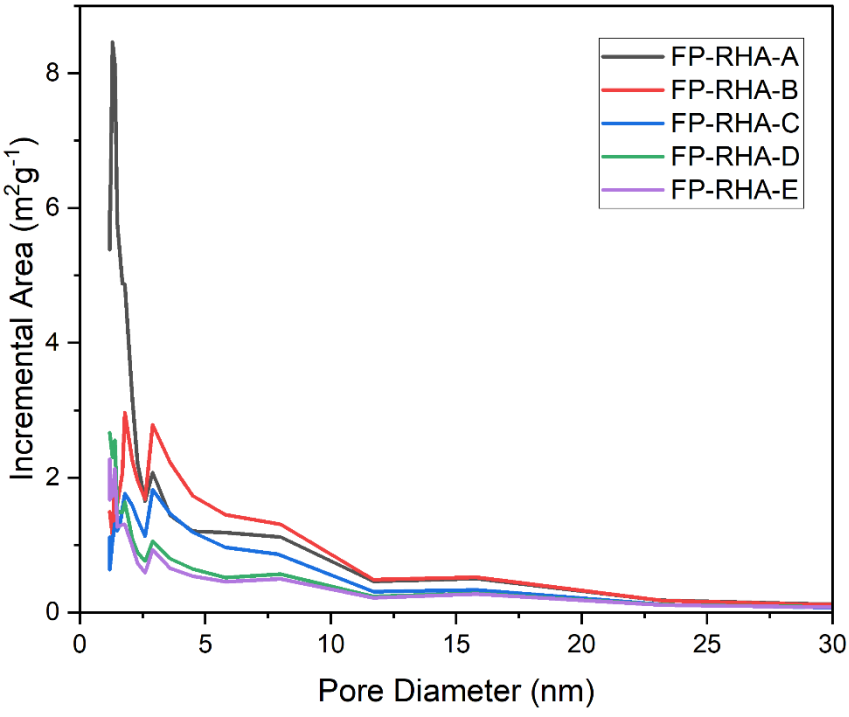

Figure 3-4: FP-RHA pore size distribution

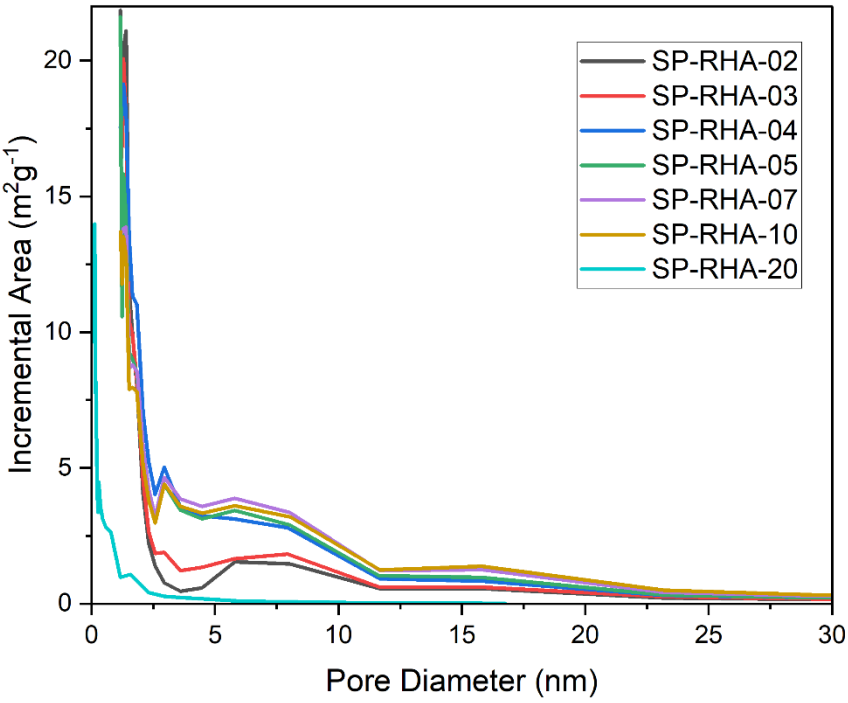

Figure 3-5: SP-RHA pore size dsitribution

3.2.4 Scanning Electron Microscopy (SEM)

Figure 3-6 shows the SEM images of rice husk; and rice husk ash produced by flame, and solar pyrolysis methods.

Rice husk seems to have a coarse, serrated structure. Presence of pores of different sizes are evident from the images for both flame and solar pyrolyzed samples. Flame pyrolyzed rice husk ash is in a hollow cylinder-like structure while solar pyrolyzed samples exhibit irregular shapes albeit similar pore structures. There are numerous canals within the samples, in sizes of a couple micrometers that are preserved regardless of the concentrated solar radiation exposure time. Furthermore, the serrated structure of rice husk is observed on all surfaces of the rice husk ash samples.

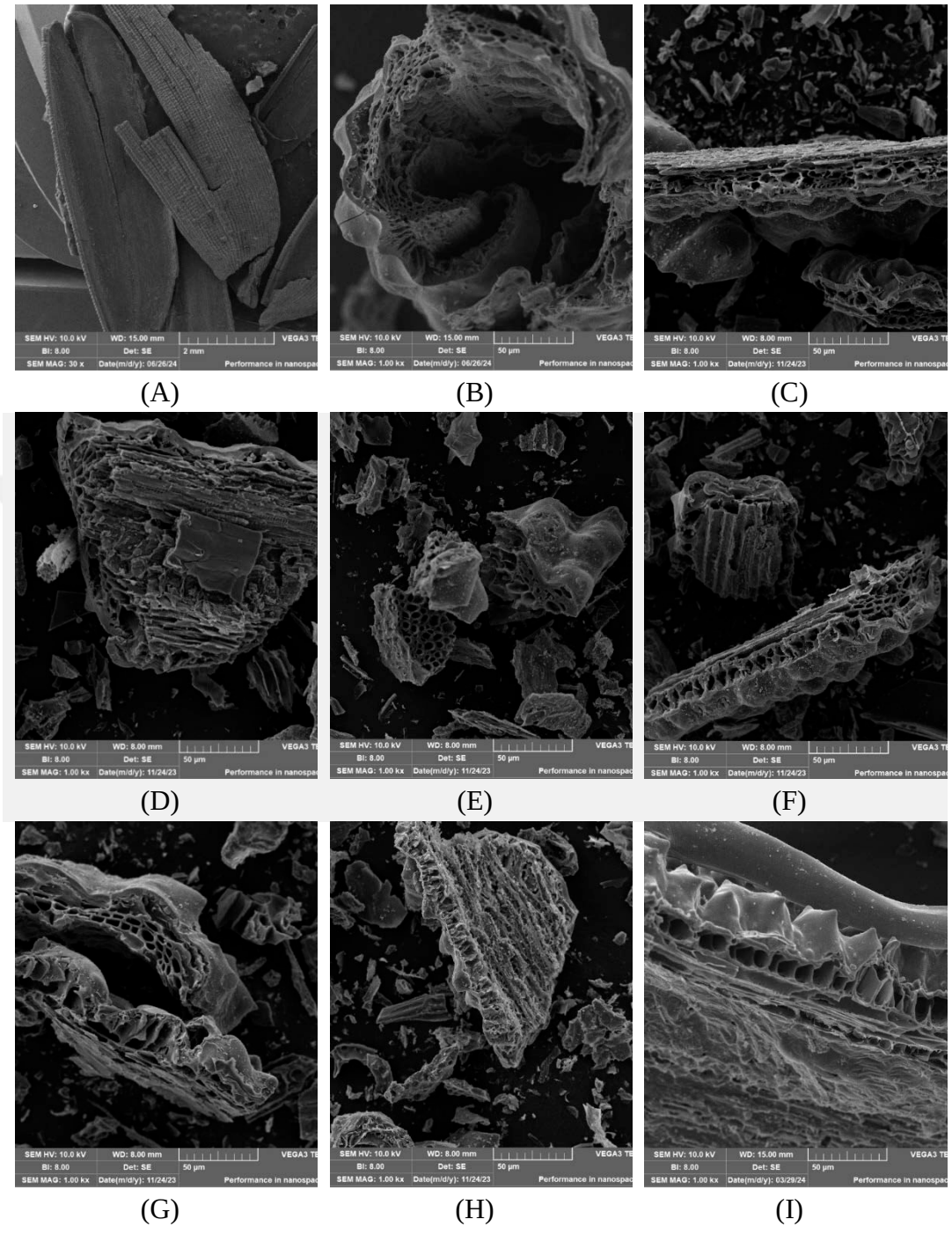

Figure 3-6: SEM images. (A) RH, (B) FP-RHA-A, (C) SP-RHA-02, (D) SP-RHA-03, (E) SP-RHA-04, (F) SP-RHA-05, (G) SP-RHA-07, (H) SP-RHA-10, (I) SP-RHA-20

3.2.5 Raman Spectroscopy

Raman spectra of FP and SP RHA samples are shown in Figure 3-7. Regardless of the production method and carbon content, all samples exhibit significant peaks at 1300 cm^{-1} and 1700 cm^{-1} regions corresponding to defect and graphitic carbon structures. Graphitic carbon is the ordered, crystalline structure of carbon while defect carbon contains the structural imperfections, or defects. Defect carbon is where the dangling bonds are present, causing the free electrons and, therefore, higher chemical reactivity. The defect carbon peaks are broad in all samples, indicating amorph defect carbon structure.

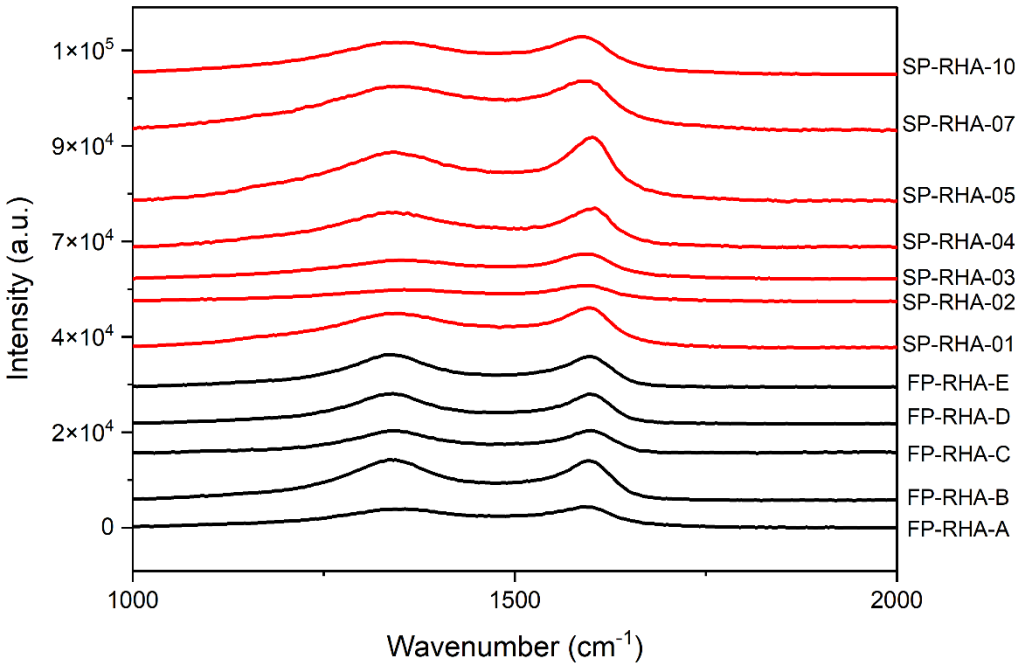

Figure 3-7: Raman Spectra of FP and SP RHA

Defect carbon contents were determined by intensity ratio of the defect carbon signals to the sum of intensity of defect and graphitic carbon signals after applying deconvolution. Deconvolution procedure is as explained in Appendix A. All deconvoluted spectra are presented in Appendix F. Defect carbon content is plotted

against carbon content in Figure 3-8. Degree of disorders were calculated as the ratio of intensity of defect carbon to graphitic carbon and shown in Figure 3-9. In this context, intensity is the area under the related peak to obtain a more accurate value due to broad bands caused by the high disorder of the samples. It is observed that, for the solar pyrolyzed samples, carbon content does not have much effect on the degree of disorder. Albeit the total carbon content decreases as the exposure time increases, ratio of defect carbon to graphitic carbon is barely affected. It can be deduced that after some point during the solar pyrolysis, graphitic carbon and defect carbon might be consumed in a similar rate.

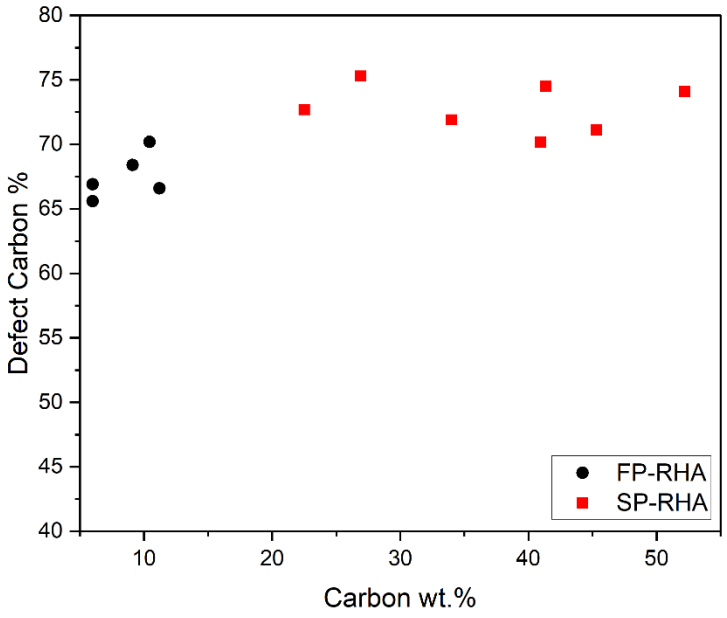

Figure 3-8: Defect carbon content of FP and SP RHA

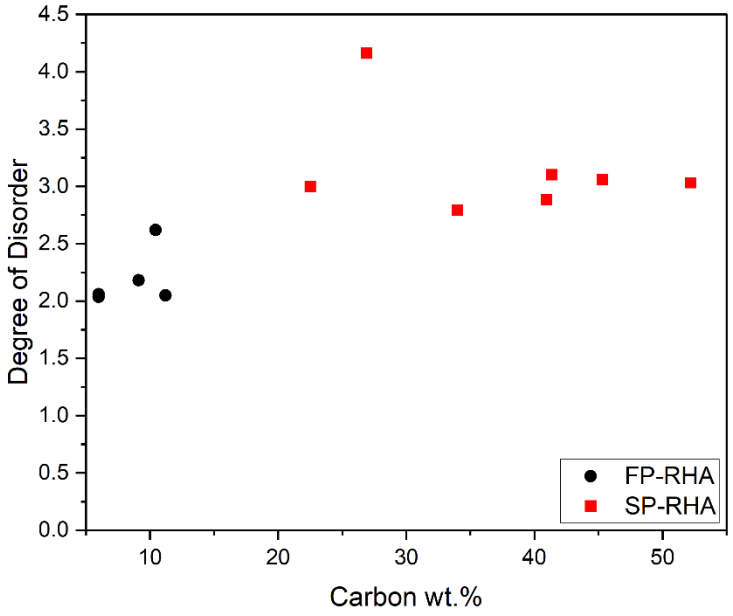

Figure 3-9: Degree of disorder of SP and FP RHA

3.2.6 Electron Spin Resonance (ESR) Spectroscopy

ESR spectra of flame and solar pyrolyzed RHA samples are given in Figure 3-10 and Figure 3-11. Both flame and solar pyrolyzed rice husk ash samples have free electrons, which comes from the defect carbon structures.

Carbon-specific ESR intensities are calculated by taking the integral of the spectra and dividing the absolute area by the carbon weight of that analyte. Carbon-specific ESR intensities are plotted against carbon content and BET surface area in Figure 3-12 and Figure 3-13. Solar pyrolyzed samples have a lower carbon specific ESR intensity despite the higher carbon content and BET surface area. This strongly indicates the higher stability of solar pyrolyzed samples, despite the higher defect carbon content. Another aspect of solar pyrolyzed samples is that carbon specific ESR intensity decreases with decreasing carbon content. Since carbon content can be directly manipulated by concentrated solar energy exposure time, it can be

deduced that free electron density can be controlled. Besides, unlike the degree of disorder, free electron density decreases with increasing solar radiation exposure time. This indicates that free electrons are somehow consumed or paired during the solar pyrolysis while defect to graphitic carbon ratio remains unaffected. Solar pyrolyzed samples offer a higher surface area with lesser free electron density, creating a material superior to flame pyrolyzed samples in terms of surface area stability.

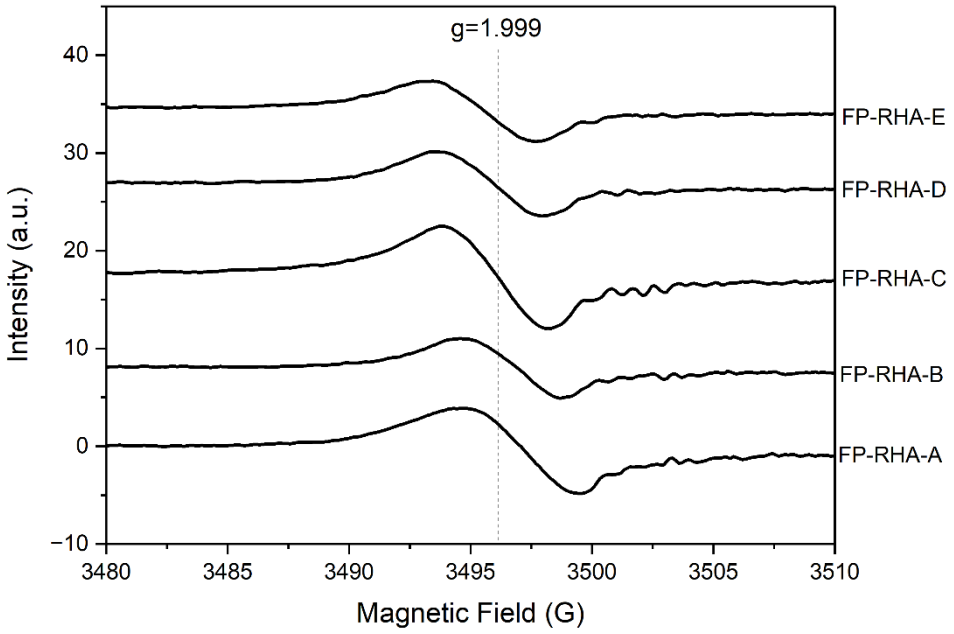

Figure 3-10: ESR spectra of FP-RHA

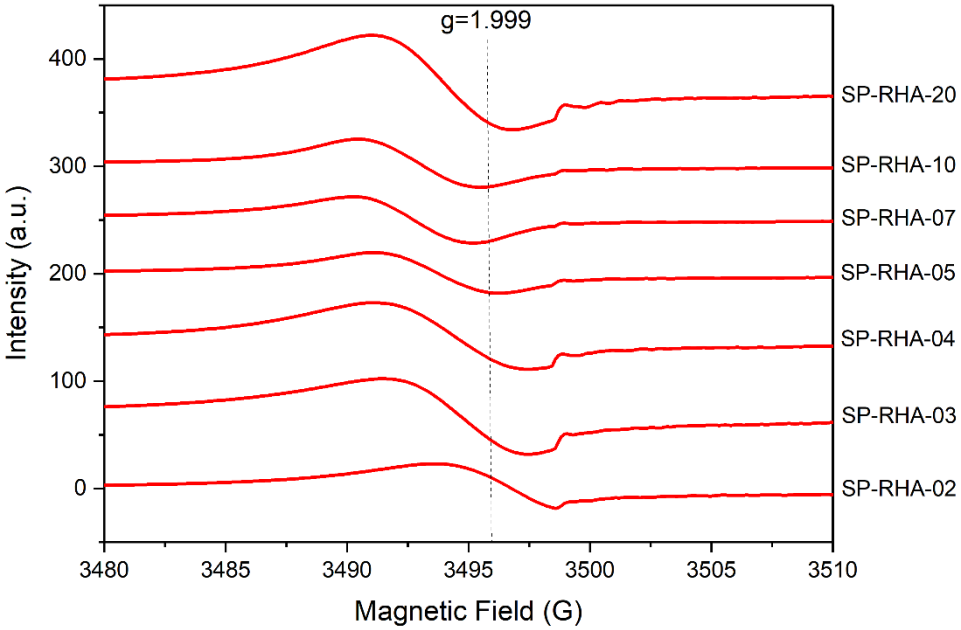

Figure 3-11: ESR spectra of SP-RHA

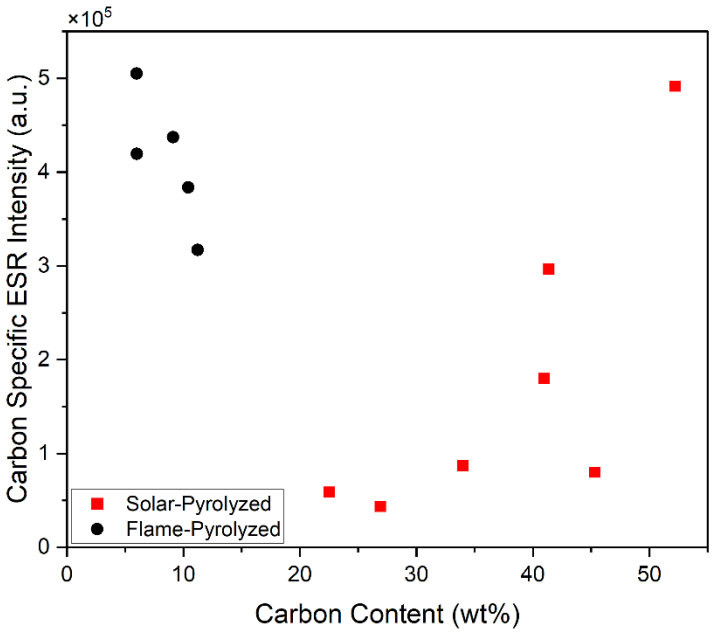

Figure 3-12: Change of carbon specific ESR intensity with respect to carbon content

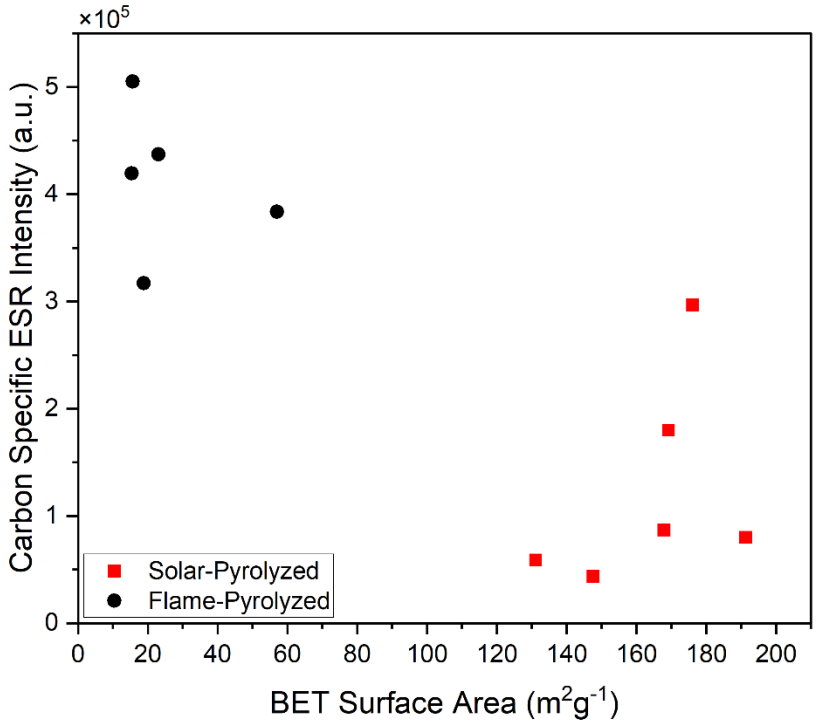

Figure 3-13: Change of carbon specific ESR intensity with respect to BET surface area

3.2.7 Nuclear Magnetic Resonance (NMR) Spectroscopy

Figure 3-14 shows the NMR ^{1}H single pulse spectrum at an acquisition time of 3.2 s for all rice husk ash samples. Spectra reveals that samples have significant peaks in both negative and positive chemical shift regions. This was attributed to presence of acidic and basic surface sites, co-existing on the rice husk ash surface.

Further NMR studies were also performed on RHA and ammonium hydroxide. Data is given in Appendices G, H and İ, and open for further investigation.

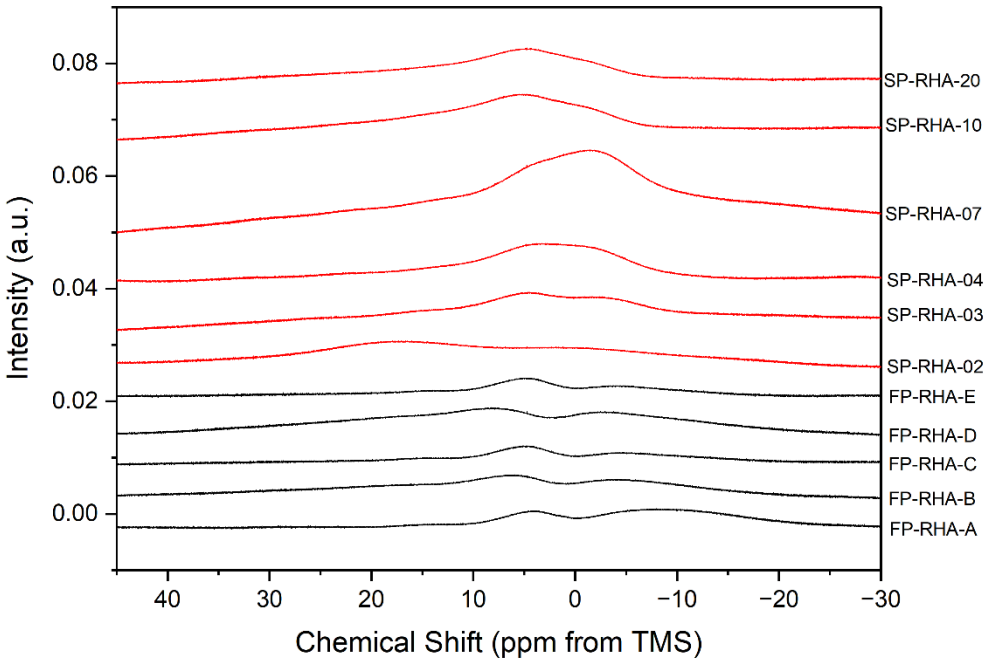

Figure 3-14: ^{1}H single pulse spectrum for RHA

3.2.8 Fourier-Transform Infrared (FTIR) Spectroscopy

IR spectrum of rice husk in Figure 3-15 shows numereous peaks, indicating a high number of functional groups. All significant peaks and corresponding functional groups are summarized in Table 3-3.

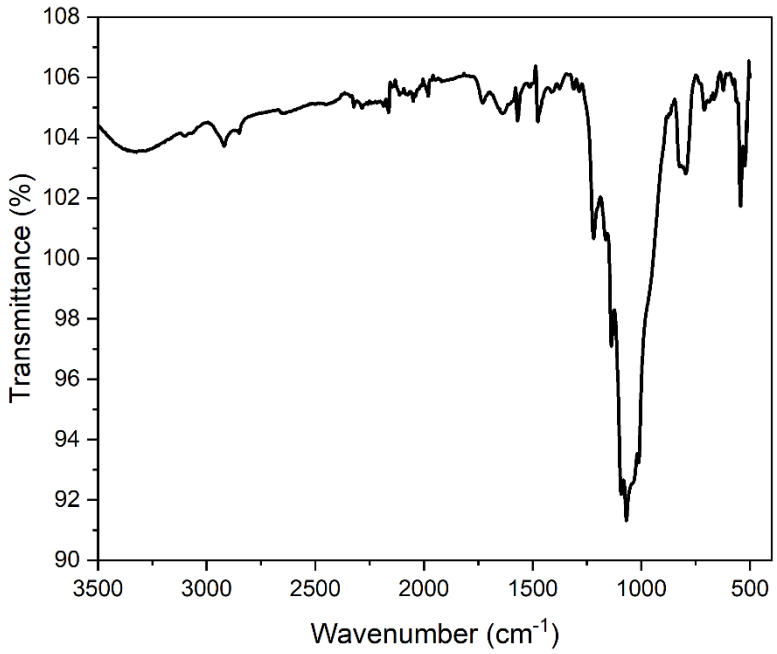

Figure 3-15: IR spectra of RH

Table 3-3: RH IR peaks and functional groups

Peak wavenumber	Functional group	Reference(s)
620	Cristobalite	[141,142]
670	C-H aromatic bending (out-plane)	[143]
790	Si-O-Si symmetric stretching	[144]
970	C=C bending	[145]
1070	Si-O-Si	[146]
1090	Si-O-Si	[146]
1140	C-N stretch	[143]
1160	C-N stretch	[143]
1220	Si-O-Si asymmetric stretching	[144]
1290	O-H bending (in-plane)	[143]
1310	O-H bending (in-plane)	[143]
1480	C-H bending	[143]

Table 3-3 (continued)

Peak wavenumber	Functional group	Reference(s)
1580	Aromatic ring stretching	[147]
1640	C=C stretching	[143]
1730	C=O stretching	[145]
2850	C-H symmetric stretching	[143,148]
2920	C-H asymmetric stretching	[143]
3100	Aromatic C-H stretching	[143]
3320	OH stretch	[143]

Figure 3-16 and Figure 3-17 shows IR spectra of flame and solar pyrolyzed rice husk ash samples. Peak wavenumbers and corresponding functional groups are summarized in Table 3-4.

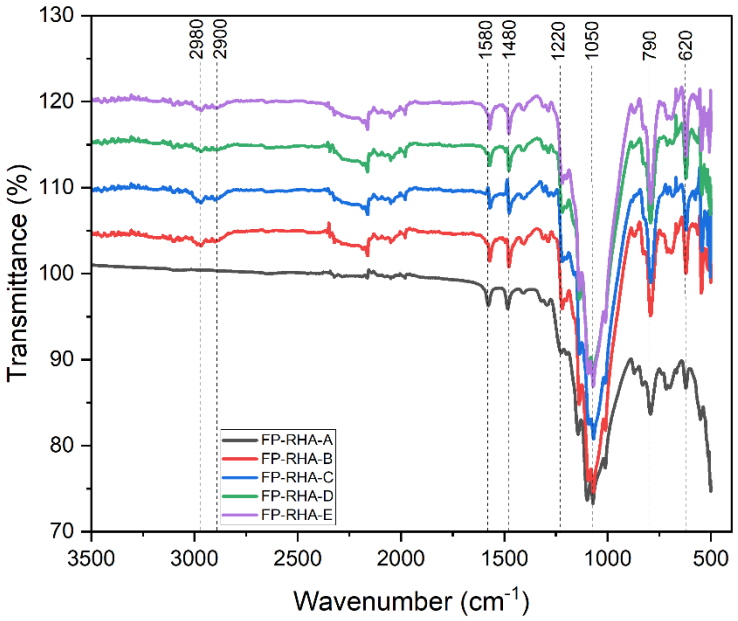

Figure 3-16: IR spectra of FP-RHA

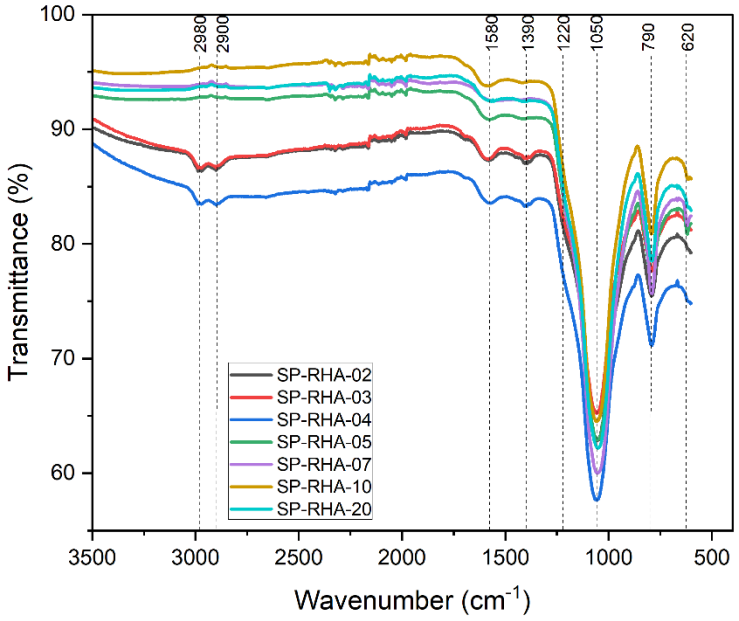

Figure 3-17: IR spectra of SP-RHA

Table 3-4: RHA IR peaks and functional groups

Peak wavenumber	Functional group	Reference(s)
620	Cristobalite	[141,142]
790	Si-O-Si symmetric stretching	[149]
1050	Si-O-Si	[146]
1220	Si-O-Si asymmetric stretching	[144]
1390	C-H bending	[143]
1480	C-H bending	[143]
1580	Aromatic ring stretching	[147]
2900	C-H aliphatic	[150]
2980	C-H aliphatic	[150]

Most of the organic functional groups have been eliminated during the pyrolysis process, as understood from the decrease in functional group diversity for the rice husk ash samples. As expected, there is not much change in the inorganic content of

rice husk. It is observed that C-H aliphatic groups at 2900 and 2980 cm^{-1} disappear after 5 minutes of solar pyrolysis. This indicates solar pyrolysis to be an effective method to manipulate several functional groups within the sample.

3.3 Use as Adsorbent

3.3.1 Gas Phase Adsorption

Ammonia and carbon dioxide adsorption isotherms at 100°C are given in Figure 3-18 and Figure 3-19.

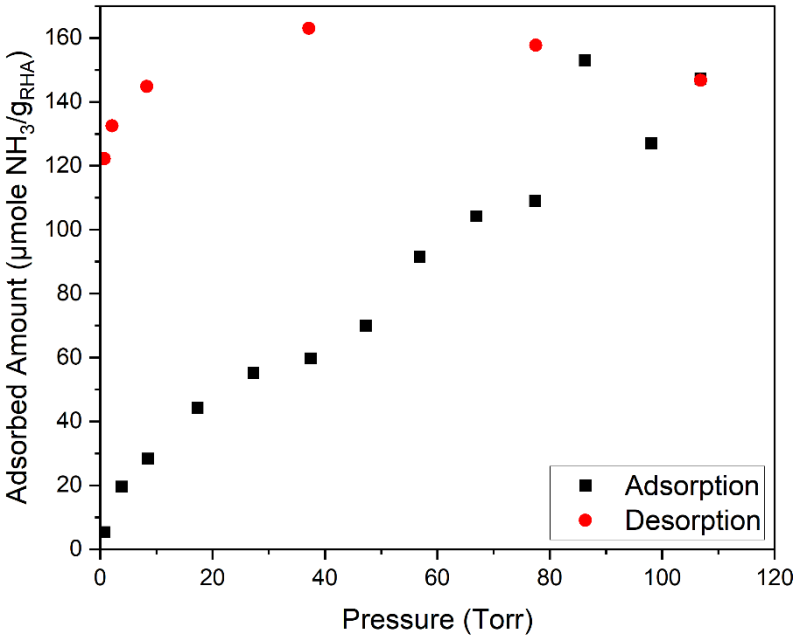

Figure 3-18: Ammonia adsorption isotherm on RHA at 100°C

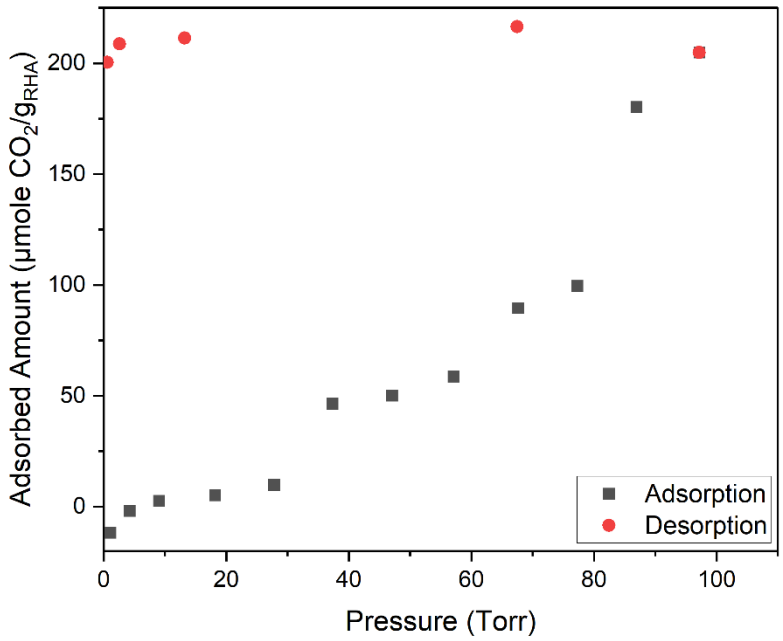

Figure 3-19: Carbon dioxide adsorption isotherm on RHA at 100°C

0.25 grams and 0.10 grams of RHA was used and at the maximum pressure of ~100 Torr, ~150 and ~200 µmoles of adsorbate was reached per gram RHA for ammonia and carbon dioxide experiments, respectively.

Ammonia and carbon dioxide have similar trends for adsorption and desorption. Albeit carbon dioxide has higher quantities adsorbed at higher pressures. One important difference between ammonia and carbon dioxide is that ammonia is a basic, and carbon dioxide is an acidic gas. Higher adsorption quantities of carbon dioxide indicates the surface basicity of RHA. Both isotherms have adsorption hysteresis. Such hysteresis might have been a result of RHA having ink-bottle type of pores, making it difficult for an adsorbate to desorb from the surface.

3.3.2 Liquid Phase Adsorption

Liquid phase adsorption studies were completed for RB5 adsorption on RHA. Adsorption was quantized by UV-Vis spectroscopy. For the calculations, a calibration plot was formed for UV-Vis absorbance intensity of RB5 at different concentrations. Calibration spectra and plot was given in Appendix G.

To measure the adsorption isotherm, 5.0 grams of RHA was mixed with 50 ml of deionized water in an Erlenmeyer flask with a stir bar. The RHA – water suspension was mixed at 500 rpm for 4 minutes and 3.0 ml of the suspension was taken, filtered, and analysed with UV-Vis spectroscopy. Without stopping the mixing, 3.0 ml of 0.52 g/L RB5 solution was added in the flask to keep the total volume constant at 50 ml. This procedure was repeated for 12 more times, and the absorbance spectra in Figure 3-20 was formed, presenting the results for different concentrations. Adsorption isotherm was measured by applying a mass balance for RB5. At each step, constant amount of RB5 was added to the system while the amount retracted for UV-Vis analysis inevitably changed. Since UV-Vis spectroscopy gives the missing information of concentration within the system, adsorbed RB5 amount can be calculated by the difference between the concentrations. Adsorption isotherm was given in Figure 3-21. Isotherm shows the continuous increase in the cumulative adsorbed RB5 amount, which signals the effectiveness of rice husk ash as an adsorbent for this particular dye.

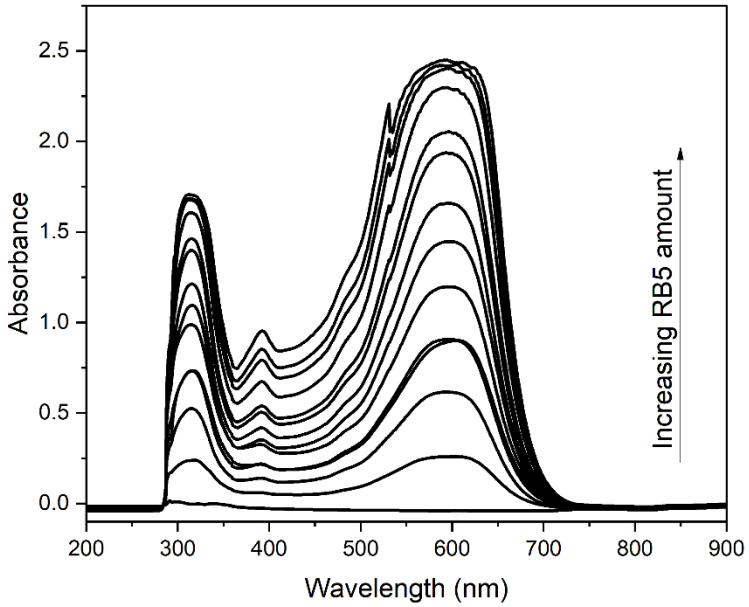

Figure 3-20: Absorbance spectra of RB5 on RHA

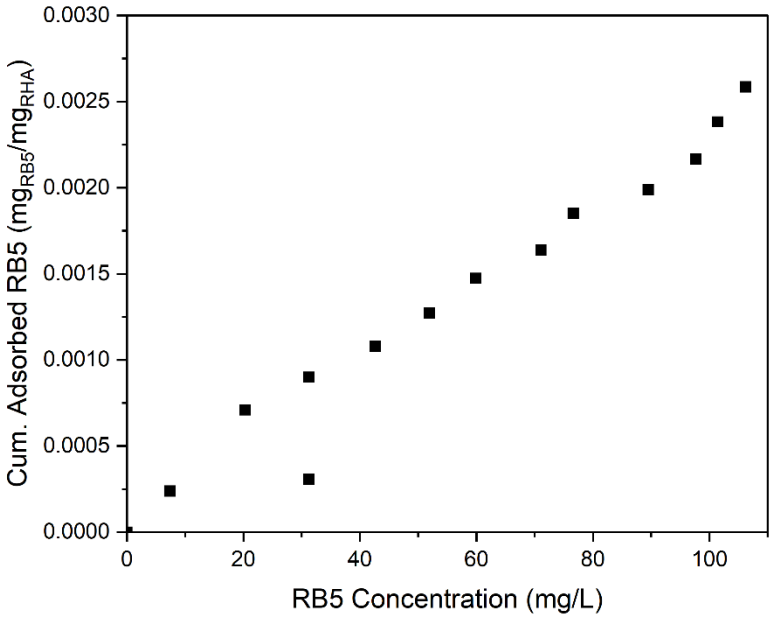

Figure 3-21: Cumulative RB5 adsorption isotherm on RHA

3.4 Use as a Catalyst Support

TPR profile of 0.5% Palladium supported on FP-RHA-A is shown in Figure 3-22. For the analysis, 36 mg of 0.5% Pd/RHA was heated to 950 ºC from room temperature with a 10ºC/min heating rate. Operational procedure was described in Appendix K.

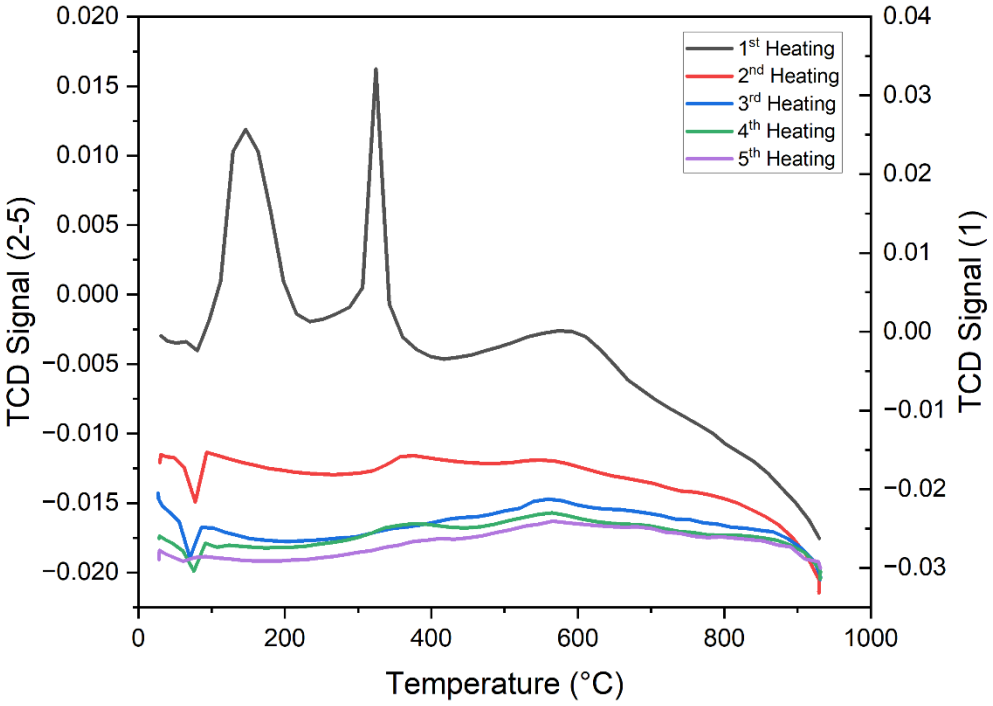

Figure 3-22: TPR profile of 0.5% Pd/RHA

In the first heating, two sharp and one broad peaks were observed at 150, 320, and 580ºC. Deconvolution surfaced another hidden peak at 260ºC. The 150ºC peak was attributed to PdO_x, and surface hydroxyl group reductions. Other peaks at 260, 320, and 580ºC peaks were attributed to hydrogenation of surface functional groups. While the first two disappear after the first heating, 580ºC peak always remains despite decreasing in intensity.

H_2 consumption was calculated to be 17 μmol for PdO_x and surface hydroxyl reduction peak at 150°C. H_2 consumption due to hydrogenation of surface functional groups were calculated as 26.8, 8.1, 9.7, 8.1 and 11.5 μmol for the cycles 1-5, respectively. Sum of these correspond to a carbon consumption of 32 μmol, or 0.39 mg. This amounts to 11 wt.% of the carbon present in the RHA sample used for the analysis.

H_2 consumption was previously calibrated using Ag_2O for the quantitaive analysis [98]. Calibration procedure details are explained in Appendix I.

CHAPTER 4

CONCLUSIONS

In this work, rice husk ash samples produced with flame pyrolysis by an industrial source, and solar pyrolysis by the author was investigated. Samples were thoroughly characterized, and potential utilization as an adsorbent for both gas and liquid phase adsorptives, and as a catalyst support in the presence of hydrogen was studied.

Rice husk ash samples were produced by two different methods: Flame pyrolysis and solar pyrolysis. Flame pyrolyzed rice husk ash was produced by an industrial source. Solar pyrolyzed rice husk ash samples were produced by a homemade concave mirror system that can concentrate solar energy in a designed focus point, where raw materials are placed for pyrolysis. Exposure time of rice husk to concentrated solar radiation was manipulated to observe the effect of pyrolysis duration. Results gave a polynomial relationship between an exposure time range of 1-40 minutes and carbon content of the product that changes across the breadth of 17-52%. It was also observed that after 10^{th} minute, exposure time have minimal effect on carbon content. This was attributed to crytallization of the sample due to sudden contact with scorching temperature levels caused by concentrated solar energy. Flame pyrolyzed rice husk ash samples, on the other hand, have a narrower carbon content range of 6-11%. BET measurements showed a direct relationship between carbon content and specific surface area. Naturally, solar pyrolyzed rice husk ash samples had greater specific surface area encompassing 133-191 m^2g^{-1} while flame pyolyzed samples stayed in the range 15-57 m^2g^{-1}. SEM images showed a serrated surface on all samples with high porosity and micro canal formations.

Both flame and solar pyrolyzed samples were found to contain defect and graphitic carbon structures. Degrees of disorder were calculated to be around 2 for flame and 3 for solar pyrolyzed samples. Despite the higher degree of disorder, solar pyrolyzed samples have lower carbon specific ESR intensities, meaning lower free electron

densities. It was observed that solar radiation exposure time has minimal effect on degree of disorder while causes a significant decrease in the free electron density. NMR studies showed the co-existing of acidic and basic functional groups on rice husk ash surface for all samples. FTIR results showed the rich variety of functional groups on rice husk surface, many of which were eradicated during the pyrolysis process.

Gas phase adsorption studies were performed with ammonia and carbon dioxide gases as adsorptives. Within a similar adsorptive pressure range, carbon dioxide had a higher adsorption amount compared to ammonia. Results indicate a higher density of basic surface sites based on the adsorption isotherm trends. Desorption for both gases showed a similar behaviour that a majority of the adsorbate remained undesorbed. This provides further validation for co-existing of acidic and basic surface sites that was indicated by NMR spectra. Liquid phase adsorption for RB5 showed that rice husk ash might be a suitable adsorbent for dye containing wastewater treatment.

Rice husk ash was used as a support for a palladium catalyst and stability tests were performed using a temperature programmed desorption equipment under hydrogen flow up to 900^{o}C. TPR profiles indicated the surface stability under hydrogen flow after the first heating for a flame pyrolyzed sample.

In short, rice husk ash is a promising material for adsorption and catalytic reaction processes. It ensures a sustainable alternative for traditional, energy consuming and high-cost materials. On top of that, solar pyrolysis method is superior to flame pyrolysis method for production of rice husk ash with higher surface area, and chemical stability while further decreasing the carbon emissions by utilizing a renewable energy source.

REFERENCES

[1] P. Ehrenfreund, W. Irvine, L. Becker, J. Blank, J.R. Brucato, L. Colangeli, S. Derenne, D. Despois, A. Dutrey, H. Fraaije, A. Lazcano, T. Owen, F. Robert, Astrophysical and astrochemical insights into the origin of life, Reports on Progress in Physics 65 (2002) 1427–1487. https://doi.org/10.1088/0034-4885/65/10/202.

[2] P.S. Karthik, A.L. Himaja, S.P. Singh, Carbon-allotropes: Synthesis methods, applications and future perspectives, Carbon Letters 15 (2014) 219–237. https://doi.org/10.5714/CL.2014.15.4.219.

[3] CD Bioparticles, Synthesis of Carbon Allotropes, (n.d.). https://www.cd-bioparticles.com/support/synthesis-of-carbon-allotropes.html.

[4] International Union of Pure and Applied Chemistry Physical Chemistry Division Commission On Colloid and Surface Chemistry Including Catalysis Reporting Physisorption Data For Gas/Solid Systems, (1985).

[5] A. Lazzarini, Activated carbons for applications in catalysis: the point of view of a physical-chemist, Rendiconti Lincei 28 (2017) 29–42. https://doi.org/10.1007/s12210-017-0603-5.

[6] H. Marsh, F. Rodríguez-Reinoso, Activated Carbon, Activated Carbon (2006) 1–536. https://doi.org/10.1016/B978-0-08-044463-5.X5013-4.

[7] N. Byamba-Ochir, W.G. Shim, M.S. Balathanigaimani, H. Moon, Highly porous activated carbons prepared from carbon rich Mongolian anthracite by direct NaOH activation, Appl Surf Sci 379 (2016) 331–337. https://doi.org/10.1016/j.apsusc.2016.04.082.

[8] D. Cuhadaroglu, O.A. Uygun, Production and characterization of activated carbon from a bituminous coal by chemical activation, Afr J Biotechnol 7 (2008) 3703–3710. https://doi.org/10.5897/AJB08.588.

[9] Z. Heidarinejad, M.H. Dehghani, M. Heidari, G. Javedan, I. Ali, M. Sillanpää, Methods for preparation and activation of activated carbon: a review, Environmental Chemistry Letters 2020 18:2 18 (2020) 393–415. https://doi.org/10.1007/S10311-019-00955-0.

[10] Y. Gao, Q. Yue, B. Gao, A. Li, Insight into activated carbon from different kinds of chemical activating agents: A review, Science of the Total Environment 746 (2020). https://doi.org/10.1016/j.scitotenv.2020.141094.

[11] N. Abuelnoor, A. AlHajaj, M. Khaleel, L.F. Vega, M.R.M. Abu-Zahra, Activated carbons from biomass-based sources for CO2 capture applications, Chemosphere 282 (2021). https://doi.org/10.1016/J.CHEMOSPHERE.2021.131111.

[12] M. Mariana, A.K. Abdul, E.M. Mistar, E.B. Yahya, T. Alfatah, M. Danish, M. Amayreh, Recent advances in activated carbon modification techniques for enhanced heavy metal adsorption, Journal of Water Process Engineering 43 (2021). https://doi.org/10.1016/j.jwpe.2021.102221.

[13] R. Hoseinzadeh Hesas, W.M.A. Wan Daud, J.N. Sahu, A. Arami-Niya, The effects of a microwave heating method on the production of activated carbon from agricultural waste: A review, J Anal Appl Pyrolysis 100 (2013) 1–11. https://doi.org/10.1016/j.jaap.2012.12.019.

[14] S.S. Lam, R.K. Liew, Y.M. Wong, E. Azwar, A. Jusoh, R. Wahi, Activated Carbon for Catalyst Support from Microwave Pyrolysis of Orange Peel, Waste Biomass Valorization 8 (2017) 2109–2119. https://doi.org/10.1007/s12649-016-9804-x.

[15] A.K. Geim, Graphene: Status and Prospects, Science (1979) 324 (2009) 1530–1534. https://doi.org/10.1126/science.1158877.

[16] V. Subrahmanyam, L. Dumpala, V. V. Subbarao, Synthesis and Raman Scattering Characterization of NRHA for Nanocomposite Applications, in:

Mater Today Proc, Elsevier Ltd, 2015: pp. 4317–4322. https://doi.org/10.1016/j.matpr.2015.10.016.

[17] K.S. Novoselov, A.K. Geim, S. V. Morozov, D. Jiang, Y. Zhang, S. V. Dubonos, I. V. Grigorieva, A.A. Firsov, Electric field effect in atomically thin carbon films, Science 306 (2004) 666–669. https://doi.org/10.1126/SCIENCE.1102896.

[18] V.B. Mbayachi, E. Ndayiragije, T. Sammani, S. Taj, E.R. Mbuta, A. ullah khan, Graphene synthesis, characterization and its applications: A review, Results Chem 3 (2021). https://doi.org/10.1016/J.RECHEM.2021.100163.

[19] Y. Zhang, Q. Wan, N. Yang, Y. Zhang, Q. Wan, N. Yang, Recent Advances of Porous Graphene: Synthesis, Functionalization, and Electrochemical Applications, Small 15 (2019) 1903780. https://doi.org/10.1002/SMLL.201903780.

[20] D.C. Marcano, D. V. Kosynkin, J.M. Berlin, A. Sinitskii, Z. Sun, A. Slesarev, L.B. Alemany, W. Lu, J.M. Tour, Improved synthesis of graphene oxide, ACS Nano 4 (2010) 4806–4814. https://doi.org/10.1021/NN1006368.

[21] F. Liu, C. Wang, X. Sui, M.A. Riaz, M. Xu, L. Wei, Y. Chen, Synthesis of graphene materials by electrochemical exfoliation: Recent progress and future potential, Carbon Energy 1 (2019) 173–199. https://doi.org/10.1002/cey2.14.

[22] J. Bin Wang, Z. Ren, Y. Hou, X.L. Yan, P.Z. Liu, H. Zhang, H.X. Zhang, J.J. Guo, A review of graphene synthesis at low temperatures by CVD methods, Xinxing Tan Cailiao/New Carbon Materials 35 (2020) 193–208. https://doi.org/10.1016/S1872-5805(20)60484-X.

[23] B. Deng, Z. Liu, H. Peng, B. Deng, Z. Liu, H. Peng, Toward Mass Production of CVD Graphene Films, Advanced Materials 31 (2019) 1800996. https://doi.org/10.1002/ADMA.201800996.

[24] Z. Chen, Y. Qi, X. Chen, Y. Zhang, Z. Liu, Direct CVD Growth of Graphene on Traditional Glass: Methods and Mechanisms, Advanced Materials 31 (2019) 1803639. https://doi.org/10.1002/ADMA.201803639.

[25] M. Chen, T. Tao, L. Zhang, W. Gao, C. Li, Highly conductive and stretchable polymer composites based on graphene/MWCNT network, Chemical Communications 49 (2013) 1612–1614. https://doi.org/10.1039/C2CC38290C.

[26] Y. Zhang, Z. Liu, A. Chen, Q. Wang, J. Zhang, C. Zhao, J. Xu, W. Yang, Y. Peng, Z. Zhang, Fabrication of Micro-/Submicro-/Nanostructured Polypropylene/Graphene Superhydrophobic Surfaces with Extreme Dynamic Pressure Resistance Assisted by Single Hierarchically Porous Anodic Aluminum Oxide Template, The Journal of Physical Chemistry C 124 (2020) 6197–6205. https://doi.org/10.1021/ACS.JPCC.9B12038.

[27] P.M. Pandian, A. Pandurangan, Copper nanoparticles anchored onto boron-doped graphene nanosheets for use as a high performance asymmetric solid-state supercapacitor, RSC Adv 9 (2019) 3443–3461. https://doi.org/10.1039/C8RA08762H.

[28] S.W. Bokhari, A.H. Siddique, P.C. Sherrell, X. Yue, K.M. Karumbaiah, S. Wei, A. V. Ellis, W. Gao, Advances in graphene-based supercapacitor electrodes, Energy Reports 6 (2020) 2768–2784. https://doi.org/10.1016/J.EGYR.2020.10.001.

[29] K.M. Yam, N. Guo, Z. Jiang, S. Li, C. Zhang, Graphene-Based Heterogeneous Catalysis: Role of Graphene, Catalysts 2020, Vol. 10, Page 53 10 (2020) 53. https://doi.org/10.3390/CATAL10010053.

[30] X. Fan, G. Zhang, F. Zhang, Multiple roles of graphene in heterogeneous catalysis, Chem Soc Rev 44 (2015) 3023–3035. https://doi.org/10.1039/C5CS00094G.

[31] R. Vidu, M. Rahman, M. Mahmoudi, M. Enachescu, T.D. Poteca, I. Opris, Nanostructures: A platform for brain repair and augmentation, Front Syst Neurosci 8 (2014). https://doi.org/10.3389/FNSYS.2014.00091.

[32] N. Anzar, R. Hasan, M. Tyagi, N. Yadav, J. Narang, Carbon nanotube - A review on Synthesis, Properties and plethora of applications in the field of biomedical science, Sensors International 1 (2020). https://doi.org/10.1016/j.sintl.2020.100003.

[33] A. Takakura, K. Beppu, T. Nishihara, A. Fukui, T. Kozeki, T. Namazu, Y. Miyauchi, K. Itami, Strength of carbon nanotubes depends on their chemical structures, Nature Communications 2019 10:1 10 (2019) 1–7. https://doi.org/10.1038/s41467-019-10959-7.

[34] H. Dai, Carbon nanotubes: opportunities and challenges, Surf Sci 500 (2002) 218–241. https://doi.org/10.1016/S0039-6028(01)01558-8.

[35] N. Gupta, S.M. Gupta, S.K. Sharma, Carbon nanotubes: synthesis, properties and engineering applications, Carbon Letters 29 (2019) 419–447. https://doi.org/10.1007/s42823-019-00068-2.

[36] N. Jain, E. Gupta, N.J. Kanu, Plethora of Carbon Nanotubes Applications in Various Fields: A State of the Art Review, Smart Science 10 (2022) 1–24. https://doi.org/10.1080/23080477.2021.1940752.

[37] S. Rathinavel, K. Priyadharshini, D. Panda, A review on carbon nanotube: An overview of synthesis, properties, functionalization, characterization, and the application, Materials Science and Engineering: B 268 (2021). https://doi.org/10.1016/J.MSEB.2021.115095.

[38] K.S. Ibrahim, Carbon nanotubes-properties and applications: a review, Carbon Letters 14 (2013) 131–144. https://doi.org/10.5714/CL.2013.14.3.131-.

[39] R. Shoukat, M.I. Khan, Carbon nanotubes: a review on properties, synthesis methods and applications in micro and nanotechnology, Microsystem Technologies 27 (2021) 4183–4192. https://doi.org/10.1007/S00542-021-05211-6.

[40] R. Fang, K. Chen, L. Yin, Z. Sun, F. Li, H.-M. Cheng, R.P. Fang, K. Chen, L.C. Yin, Z.H. Sun, F. Li, H. Cheng, The Regulating Role of Carbon Nanotubes and Graphene in Lithium-Ion and Lithium–Sulfur Batteries, Advanced Materials 31 (2019) 1800863. https://doi.org/10.1002/ADMA.201800863.

[41] J. Wang, W. Qin, X. Zhu, Y. Teng, Covalent organic frameworks (COF)/CNT nanocomposite for high performance and wide operating temperature lithium–sulfur batteries, Energy 199 (2020). https://doi.org/10.1016/j.energy.2020.117372.

[42] F. Mashkoor, A. Nasar, Inamuddin, Carbon nanotube-based adsorbents for the removal of dyes from waters: A review, Environ Chem Lett 18 (2020) 605–629. https://doi.org/10.1007/S10311-020-00970-6.

[43] P. Serp, E. Castillejos, Catalysis in carbon nanotubes, ChemCatChem 2 (2010) 41–47. https://doi.org/10.1002/cctc.200900283.

[44] E. Dujardin, T.W. Ebbesen, H. Hiura, K. Tanigaki, Capillarity and wetting of carbon nanotubes, Science (1979) 265 (1994) 1850–1852. https://doi.org/10.1126/science.265.5180.1850.

[45] C. Pham-Huu, N. Keller, C. Estournès, G. Ehret, M.J. Ledoux, Synthesis of CoFe2O4 nanowire in carbon nanotubes. A new use of the confinement effect, Chemical Communications (2002) 1882–1883. https://doi.org/10.1039/B203787B.

[46] G.W. Huber, S. Iborra, A. Corma, Synthesis of transportation fuels from biomass: Chemistry, catalysts, and engineering, Chem Rev 106 (2006) 4044–4098. https://doi.org/10.1021/CR068360D.

[47] A.K. Karmaker, M.M. Rahman, M.A. Hossain, M.R. Ahmed, Exploration and corrective measures of greenhouse gas emission from fossil fuel power stations for Bangladesh, J Clean Prod 244 (2020) 118645. https://doi.org/10.1016/J.JCLEPRO.2019.118645.

[48] L.J.R. Nunes, The rising threat of atmospheric CO2: A review on the causes, impacts, and mitigation strategies, Environments 2023, Vol. 10, Page 66 10 (2023) 66. https://doi.org/10.3390/ENVIRONMENTS10040066.

[49] J. Wang, W. Azam, Natural resource scarcity, fossil fuel energy consumption, and total greenhouse gas emissions in top emitting countries, Geoscience Frontiers 15 (2024) 101757. https://doi.org/10.1016/J.GSF.2023.101757.

[50] H. Ritchie, P. Rosado, M. Roser, Energy production and consumption, Our World in Data (2024). https://ourworldindata.org/energy-production-consumption.

[51] J. Bezerra, E. Turnhout, I.M. Vasquez, T.F. Rittl, B. Arts, T.W. Kuyper, The promises of the Amazonian soil: shifts in discourses of Terra Preta and biochar, Journal of Environmental Policy & Planning 21 (2019) 623–635. https://doi.org/10.1080/1523908X.2016.1269644.

[52] W. Chen, J. Meng, X. Han, Y. Lan, W. Zhang, Past, present, and future of biochar, Biochar 2019 1:1 1 (2019) 75–87. https://doi.org/10.1007/S42773-019-00008-3.

[53] X.S. Wang, D. Chen, H. Wang, L. Liu, J.F. Huang, X.M. Duan, X.X. Yan, X.G. Luo, Mawangdui-Type Ancient Human Cadavers in China and Strategies for Their Long-Term Preservation, Biopreserv Biobank 17 (2019) 113–118. https://doi.org/10.1089/BIO.2019.0018.

[54] B. Qiu, X. Tao, H. Wang, W. Li, X. Ding, H. Chu, Biochar as a low-cost adsorbent for aqueous heavy metal removal: A review, J Anal Appl Pyrolysis 155 (2021) 105081. https://doi.org/10.1016/J.JAAP.2021.105081.

[55] J. Prens, Z. Kurt, A.M. James Rivas, J. Chen, Production and characterization of wild sugarcane (Saccharum spontaneum L.) biochar for atrazine adsorption in aqueous media, Agronomy 2023, Vol. 13, Page 27 13 (2022) 27. https://doi.org/10.3390/AGRONOMY13010027.

[56] J. Maroušek, L. Trakal, Techno-economic analysis reveals the untapped potential of wood biochar, Chemosphere 291 (2022) 133000. https://doi.org/10.1016/J.CHEMOSPHERE.2021.133000.

[57] J. Buggenhout, K. Brijs, I. Celus, J.A. Delcour, The breakage susceptibility of raw and parboiled rice: A review, J Food Eng 117 (2013) 304–315. https://doi.org/10.1016/j.jfoodeng.2013.03.009.

[58] L.Z. Cheong, X. Xu, Rice bran and rice bran oil: Chemistry, processing and utilization, Elsevier, 2019. https://doi.org/10.1016/C2016-0-02191-5.

[59] X. Zhuang, T. Yin, W. Han, X. Zhang, Nutritional ingredients and active compositions of defatted rice bran, in: Rice Bran and Rice Bran Oil: Chemistry, Processing and Utilization, Elsevier, 2019: pp. 247–270. https://doi.org/10.1016/B978-0-12-812828-2.00010-X.

[60] A.A. Behroozmand, K. Keating, E. Auken, A review of the principles and applications of the NMR technique for near-surface characterization, Surv Geophys 36 (2015) 27–85. https://doi.org/10.1007/S10712-014-9304-0.

[61] D. Battegazzore, S. Bocchini, J. Alongi, A. Frache, Rice husk as bio-source of silica: Preparation and characterization of PLA-silica bio-composites, RSC Adv 4 (2014) 54703–54712. https://doi.org/10.1039/c4ra05991c.

[62] M. Kordi, N. Farrokhi, M.I. Pech-Canul, A. Ahmadikhah, Rice husk at a glance: From agro-industrial to modern applications, Rice Sci 31 (2024) 14–32. https://doi.org/10.1016/J.RSCI.2023.08.005.

[63] FAO publications catalogue 2023, FAO Publications Catalogue 2023 (2023). https://doi.org/10.4060/CC7285EN.

[64] I.J. Fernandes, D. Calheiro, A.G. Kieling, C.A.M. Moraes, T.L.A.C. Rocha, F.A. Brehm, R.C.E. Modolo, Characterization of rice husk ash produced using different biomass combustion techniques for energy, Fuel 165 (2016) 351–359. https://doi.org/10.1016/j.fuel.2015.10.086.

[65] C.A.M. Moraes, I.J. Fernandes, D. Calheiro, A.G. Kieling, F.A. Brehm, M.R. Rigon, J.A. Berwanger Filho, I.A.H. Schneider, E. Osorio, Review of the rice production cycle: By-products and the main applications focusing on rice husk combustion and ash recycling, Waste Management and Research 32 (2014) 1034–1048. https://doi.org/10.1177/0734242X14557379.

[66] M.J. Kaleli, P.K. Kamweru, J.M. Gichumbi, F.G. Ndiritu, Characterization of rice husk ash prepared by open air burning and furnace calcination, Journal of Chemical Engineering and Materials Science 11 (2020) 24–30. https://doi.org/10.5897/jcems2020.0348.

[67] Y. Zou, T. Yang, Rice husk, rice husk ash and their applications, in: Rice Bran and Rice Bran Oil: Chemistry, Processing and Utilization, Elsevier, 2019: pp. 207–246. https://doi.org/10.1016/B978-0-12-812828-2.00009-3.

[68] B. Karunanithi, S. Sivasubramaniya, K. Bogeshwaran, R. Kalaivani, S. Ashraf, G.N. Manikandan, G.E. Prabhu, Production of silica from rice husk, 2014. https://www.researchgate.net/publication/285026933.

[69] S.S. Shukla, R. Chava, S. Appari, B. A, B.V.R. Kuncharam, Sustainable use of rice husk for the cleaner production of value-added products, J Environ Chem Eng 10 (2022). https://doi.org/10.1016/j.jece.2021.106899.

[70] E. Assureira, Rice husk: An alternative fuel in Perú, Stoves.Bioenergylists.Org (n.d.). http://www.stoves.bioenergylists.org/stovesdoc/peru/bp48_pp35-36.pdf.

[71] I. Quispe, R. Navia, R. Kahhat, Energy potential from rice husk through direct combustion and fast pyrolysis: A review, Waste Management 59 (2017) 200–210. https://doi.org/10.1016/J.WASMAN.2016.10.001.

[72] R. Fathurahman, A. Surjosatyo, Utilization of rice husks as a fuel for gasification – A review, IOP Conf Ser Earth Environ Sci 1034 (2022) 012065. https://doi.org/10.1088/1755-1315/1034/1/012065.

[73] S.K.S. Hossain, L. Mathur, P.K. Roy, Rice husk/rice husk ash as an alternative source of silica in ceramics: A review, Journal of Asian Ceramic Societies 6 (2018) 299–313. https://doi.org/10.1080/21870764.2018.1539210.

[74] G.A. Benedet, A. Zaccaron, J.M. Inocente, V. de Souza Nandi, S. Arcaro, F. Raupp-Pereira, D. Gorini Neto, Development of eco-friendly clay ceramics using rice husk ash as a secondary mineral source of quartz, Mater Today Commun 38 (2024) 108103. https://doi.org/10.1016/J.MTCOMM.2024.108103.

[75] Y. Wang, H. Jia, P. Chen, X. Fang, T. Du, Synthesis of La and Ce modified X zeolite from rice husk ash for carbon dioxide capture, Journal of Materials Research and Technology 9 (2020) 4368–4378. https://doi.org/10.1016/j.jmrt.2020.02.061.

[76] C.G. Flores, H. Schneider, J.S. Dornelles, L.B. Gomes, N.R. Marcilio, P.J. Melo, Synthesis of potassium zeolite from rice husk ash as a silicon source, Clean Eng Technol 4 (2021). https://doi.org/10.1016/j.clet.2021.100201.

[77] P.L. Tran-Nguyen, K.P. Ly, L.H.V. Thanh, A.E. Angkawijaya, S.P. Santoso, N.P.D. Tran, M.L. Tsai, Y.H. Ju, Facile synthesis of zeolite NaX using rice husk ash without pretreatment, J Taiwan Inst Chem Eng 123 (2021) 338–345. https://doi.org/10.1016/J.JTICE.2021.05.009.

[78] D. Prasetyoko, Z. Ramli, S. Endud, H. Hamdan, B. Sulikowski, Conversion of rice husk ash to zeolite beta, Waste Management 26 (2006) 1173–1179. https://doi.org/10.1016/j.wasman.2005.09.009.

[79] H.P. Wang, K.S. Lin, Y.J. Huang, M.C. Li, L.K. Tsaur, Synthesis of zeolite ZSM-48 from rice husk ash, J Hazard Mater 58 (1998) 147–152. https://doi.org/10.1016/S0304-3894(97)00127-1.

[80] S. Ruengsri, S. Insiripong, N. Sangwaranatee, J. Kaewkhao, Development of barium borosilicate glasses for radiation shielding materials using rice husk ash as a silica source, Progress in Nuclear Energy 83 (2015) 99–104. https://doi.org/10.1016/J.PNUCENE.2015.03.006.

[81] İ. Özkan, E. Dokumacı, Utilization of rice husk ash for production of sodium borosilicate glass cullets, Journal of the Australian Ceramic Society 58 (2022) 151–156. https://doi.org/10.1007/s41779-021-00679-x.

[82] K. Farooque, M. Zaman, E. Halim, S. Islam, M. Hossain, Y. Mollah, A. Mahmood, Characterization and utilization of rice husk ash (RHA) from rice mill of Bangladesh, Bangladesh Journal of Scientific and Industrial Research 44 (2009) 157–162. https://doi.org/10.3329/BJSIR.V44I2.3666.

[83] J. Li, P. Chen, H. Cai, Y. Xu, C. Li, Preliminary study on the utilization of RHA as a performance enhancer for rubber mortar, Materials 2021, Vol. 14, Page 3216 14 (2021) 3216. https://doi.org/10.3390/MA14123216.

[84] S.K. Das, J. Mishra, S.K. Singh, S.M. Mustakim, A. Patel, S.K. Das, U. Behera, Characterization and utilization of rice husk ash (RHA) in fly ash: Blast furnace slag based geopolymer concrete for sustainable future, Mater Today Proc 33 (2020) 5162–5167. https://doi.org/10.1016/J.MATPR.2020.02.870.

[85] V.C. Srivastava, I.D. Mall, I.M. Mishra, Characterization of mesoporous rice husk ash (RHA) and adsorption kinetics of metal ions from aqueous solution onto RHA, J Hazard Mater 134 (2006) 257–267. https://doi.org/10.1016/J.JHAZMAT.2005.11.052.

[86] F.F. Severo, L.S. da Silva, J.S.C. Moscôso, Q. Sarfaraz, L.F. Rodrigues Júnior, A.F. Lopes, L.B. Marzari, G.D. Molin, Chemical and physical characterization of rice husk biochar and ashes and their iron adsorption capacity, SN Appl Sci 2 (2020). https://doi.org/10.1007/s42452-020-3088-2.

[87] W. Bai, M. Qian, Q. Li, S. Atkinson, B. Tang, Y. Zhu, J. Wang, Rice husk-based adsorbents for removing ammonia: Kinetics, thermodynamics and adsorption mechanism, J Environ Chem Eng 9 (2021). https://doi.org/10.1016/J.JECE.2021.105793.

[88] Q. Feng, Q. Lin, F. Gong, S. Sugita, M. Shoya, Adsorption of lead and mercury by rice husk ash, J Colloid Interface Sci 278 (2004) 1–8. https://doi.org/10.1016/j.jcis.2004.05.030.

[89] U.R. Lakshmi, V.C. Srivastava, I.D. Mall, D.H. Lataye, Rice husk ash as an effective adsorbent: evaluation of adsorptive characteristics for Indigo Carmine dye, J Environ Manage 90 (2009) 710–720. https://doi.org/10.1016/J.JENVMAN.2008.01.002.

[90] V.R. Madduluri, K.K. Mandari, V. Velpula, M. Varkolu, S.R.R. Kamaraju, M. Kang, Rice husk-derived carbon-silica supported Ni catalysts for selective hydrogenation of biomass-derived furfural and levulinic acid, Fuel 261 (2020). https://doi.org/10.1016/j.fuel.2019.116339.

[91] Malahayati, E. Yufita, I. Ismail, M. Mursal, R. Idroes, Z. Jalil, The Effect of Natural Silica from Rice Husk Ash and Nickel as a Catalyst on the Hydrogen Storage Properties of MgH2, Journal of Ecological Engineering 22 (2021) 79–85. https://doi.org/10.12911/22998993/142959.

[92] Z. Teng, S. Huang, L. Fu, H. Xu, N. Li, Q. Zhou, Study of a catalyst supported on rice husk ash for NO reduction with carbon monoxide, Catal Sci Technol 10 (2020) 1431–1443. https://doi.org/10.1039/C9CY02204J.

[93] F. Adam, S. Balakrishnan, P.-L. Wong, Rice husk ash silica as a support material for ruthenium based heterogenous catalyst, 2006.

[94] N. Kleger, C. Minas, P. Bosshard, I. Mattich, K. Masania, A.R. Studart, Hierarchical porous materials made by stereolithographic printing of photo-curable emulsions, Scientific Reports 2021 11:1 11 (2021) 1–11. https://doi.org/10.1038/s41598-021-01720-6.

[95] X.Y. Yang, L.H. Chen, Y. Li, J.C. Rooke, C. Sanchez, B.L. Su, Hierarchically porous materials: synthesis strategies and structure design, Chem Soc Rev 46 (2017) 481–558. https://doi.org/10.1039/C6CS00829A.

[96] W.Q. Tian, X.Y. Wu, K.X. Wang, Y.M. Jiang, J.F. Wang, J.S. Chen, Hierarchical porous carbon spheres as an anode material for lithium ion batteries, RSC Adv 3 (2013) 10823–10827. https://doi.org/10.1039/C3RA40667A.

[97] A. Bahrami, U. Simon, N. Soltani, S. Zavareh, J. Schmidt, M.I. Pech-Canul, A. Gurlo, Eco-fabrication of hierarchical porous silica monoliths by ice-templating of rice husk ash, 19 (2017) 188. https://doi.org/10.1039/c6gc02153k.

[98] M. Yarar, Interaction of hydrogen with titanium dioxide and palladium-titanium dioxide surface at low and high temperature, 2022. https://open.metu.edu.tr/handle/11511/101188.

[99] B.D. Cullity, S.R. Stock, Elements of x-ray diffraction, Addison-Wesley, Massachusetts, 1957. https://doi.org/10.1021/ED034PA178.

[100] L.A. Feigin, D.I. Svergun, Structure analysis by small-angle X-ray and neutron scattering, Structure Analysis by Small-Angle X-Ray and Neutron Scattering (1987). https://doi.org/10.1007/978-1-4757-6624-0.

[101] M.H. Boratto, Semiconducting and Insulating oxides applied to electronic devices, 2018. https://www.researchgate.net/publication/326560396_Semiconducting_and_Insulating_oxides_applied_to_electronic_devices.

[102] D.D. Dung, Magnetism in titanates, Defect-Induced Magnetism in Oxide Semiconductors (2023) 481–527. https://doi.org/10.1016/B978-0-323-90907-5.00011-7.

[103] Chemistry LibreTexts, X-ray diffraction (XRD) basics and application, (n.d.). https://chem.libretexts.org/Courses/Franklin_and_Marshall_College/Introduction_to_Materials_Characterization__CHM_412_Collaborative_Text/Diffraction_Techniques/X-ray_diffraction_(XRD)_basics_and_application.

[104] K. Ahmad, M.B. Kakakhel, S. Hayat, M. Wazir-ud-Din, M.M. Mahmood, S. Ur Rehman, M.T. Siddique, S.M. Mirza, Thermoluminescence study of pellets prepared using NaCl from Khewra Salt Mines in Pakistan, Radiat Environ Biophys 60 (2021) 365–375. https://doi.org/10.1007/S00411-021-00894-X.

[105] S. Loganathan, R.B. Valapa, R.K. Mishra, G. Pugazhenthi, S. Thomas, Thermogravimetric analysis for characterization of nanomaterials, Thermal and Rheological Measurement Techniques for Nanomaterials Characterization 3 (2017) 67–108. https://doi.org/10.1016/B978-0-323-46139-9.00004-9.

[106] Thermogravimetric analysis (TGA), Chemistry LibreTexts (n.d.). https://chem.libretexts.org/Courses/Franklin_and_Marshall_College/Introduction_to_Materials_Characterization__CHM_412_Collaborative_Text/Thermal_Analysis/Thermogravimetric_analysis_(TGA).

[107] S. Brunauer, P.H. Emmett, E. Teller, Adsorption of Gases in Multimolecular Layers, J Am Chem Soc 60 (1938) 309–319. https://doi.org/10.1021/JA01269A023.

[108] I. Langmuir, The adsorption of gases on plane surfaces of glass, mica and platinum, J Am Chem Soc 40 (1918) 1361–1403. https://doi.org/10.1021/JA02242A004.

[109] R. Masters, Novel techniques in the scanning electron microscope for characterising polymer-based photovoltaic materials, 2017.

[110] D.A. Skoog, F.J. Holler, S.R. Crouch, Principles of Instrumental Analysis. , 7th ed., Thomson Brooks/Cole, Belmont, 2007.

[111] J.W. Niemantsverdriet, Spectroscopy in Catalysis, 3rd, Completely Revised and Enlarged Edition, (2007) 344. https://www.wiley.com/en-jp/Spectroscopy+in+Catalysis%3A+An+Introduction%2C+3rd%2C+Completely+Revised+and+Enlarged+Edition-p-9783527611355.

[112] A.C. Ferrari, J.C. Meyer, V. Scardaci, C. Casiraghi, M. Lazzeri, F. Mauri, S. Piscanec, D. Jiang, K.S. Novoselov, S. Roth, A.K. Geim, Raman spectrum of graphene and graphene layers, Phys Rev Lett 97 (2006). https://doi.org/10.1103/PhysRevLett.97.187401.

[113] Z. Li, L. Deng, I.A. Kinloch, R.J. Young, Raman spectroscopy of carbon materials and their composites: Graphene, nanotubes and fibres, Prog Mater Sci 135 (2023). https://doi.org/10.1016/j.pmatsci.2023.101089.

[114] M.J. Pelletier, Quantitative analysis using Raman spectrometry, Appl Spectrosc 57 (2003). https://doi.org/10.1366/000370203321165133.

[115] A. Jorio, R. Saito, G. Dresselhaus, M.S. Dresselhaus, Raman Spectroscopy in Graphene Related Systems, John Wiley & Sons, 2011.

[116] J. Dennison, M. Holtz, Raman spectroscopy of carbon materials, Spectroscopy 11 (1996) 1. https://digitalcommons.usu.edu/mp_facpub/26/.

[117] A. Ferrari, J. Robertson, Interpretation of Raman spectra of disordered and amorphous carbon, Phys Rev B 61 (2000) 14095. https://doi.org/10.1103/PhysRevB.61.14095.

[118] R. Rao, J. Reppert, R. Podila, X. Zhang, A.M. Rao, S. Talapatra, B. Maruyama, Double resonance Raman study of disorder in CVD-grown single-walled carbon nanotubes, Carbon N Y 49 (2011) 1318–1325. https://doi.org/10.1016/j.carbon.2010.11.052.

[119] Anders Lund, Masaru Shiotani, Shigetaka Shimada, Principles and Applications of ESR Spectroscopy, New York, 2011.

[120] L.D.S. Yadav, Organic Spectroscopy, Springer Netherlands, 2005. https://doi.org/10.1007/978-1-4020-2575-4.

[121] Chemistry LibreTexts, EPR: Interpretation, (n.d.). https://chem.libretexts.org/Bookshelves/Physical_and_Theoretical_Chemistry_Textbook_Maps/Supplemental_Modules_(Physical_and_Theoretical_Chemistry)/Spectroscopy/Magnetic_Resonance_Spectroscopies/Electron_Paramagnetic_Resonance/EPR_-_Interpretation.

[122] Chemistry LibreTexts, NMR Spectroscopy, (n.d.). https://chem.libretexts.org/Bookshelves/Analytical_Chemistry/Physical_Methods_in_Chemistry_and_Nano_Science_(Barron)/04%3A_Chemical_Speciation/4.07%3A_NMR_Spectroscopy.

[123] M.H.. Levitt, Spin dynamics : basics of nuclear magnetic resonance, John Wiley & Sons, Ltd, 2008.

[124] Chemistry LibreTexts, How an FTIR Spectrometer Operates, (n.d.). https://chem.libretexts.org/Bookshelves/Physical_and_Theoretical_Chemistry_Textbook_Maps/Supplemental_Modules_(Physical_and_Theoretical_Chemistry)/Spectroscopy/Vibrational_Spectroscopy/Infrared_Spectroscopy/How_an_FTIR_Spectrometer_Operates.

[125] Chemistry LibreTexts, Infrared Spectroscopy, (n.d.). https://chem.libretexts.org/Bookshelves/Physical_and_Theoretical_Chemistry_Textbook_Maps/Supplemental_Modules_(Physical_and_Theoretical_Chemistry)/Spectroscopy/Vibrational_Spectroscopy/Infrared_Spectroscopy/Infrared_Spectroscopy.

[126] J.J. Ojeda, M. Dittrich, Fourier transform infrared spectroscopy for molecular analysis of microbial cells, Methods in Molecular Biology 881 (2012) 187–211. https://doi.org/10.1007/978-1-61779-827-6_8.

[127] Caffeine, (n.d.). https://webbook.nist.gov/cgi/cbook.cgi?ID=C58082&Mask=80#IR-Spec.

[128] The CALVET calorimeter - SETARAM, (n.d.). https://setaramsolutions.com/product/calvet.

[129] C. Miao, Y. Ju Park, W. Liu, M. Joshi, S. Jun Hu, M.S. Goorsky, L.E. Vilchiz-Bravo, A. Pacheco-Vega, B.E. Handy, Heat-flow and temperature control in Tian-Calvet microcalorimeters: toward higher detection limits Porous Silicon Films for Thin Film Layer Transfer and Wafer Bonding Applications, Meas. Sci. Technol 21 (2010) 8. https://doi.org/10.1088/0957-0233/21/11/115103.

[130] Chemistry LibreTexts, UV-Visible Spectroscopy, (n.d.). https://chem.libretexts.org/Bookshelves/Analytical_Chemistry/Physical_Methods_in_Chemistry_and_Nano_Science_(Barron)/04%3A_Chemical_Speciation/4.04%3A_UV-Visible_Spectroscopy.

[131] H.-Helmut. Perkampus, UV-VIS Spectroscopy and Its Applications Heinz-Helmut Perkampus, (2013).

[132] M. El Bouraie, W.S. El Din, Biodegradation of Reactive Black 5 by Aeromonas hydrophila strain isolated from dye-contaminated textile wastewater, Sustainable Environment Research 26 (2016) 209–216. https://doi.org/10.1016/J.SERJ.2016.04.014.

[133] PubChem, Reactive Black 5 | C26H21N5Na4O19S6 | CID 135442967, (n.d.). https://pubchem.ncbi.nlm.nih.gov/compound/Reactive-Black-5.

[134] M.S. Roriz, J.F. Osma, J.A. Teixeira, S. Rodríguez Couto, Application of response surface methodological approach to optimise Reactive Black 5 decolouration by crude laccase from Trametes pubescens, J Hazard Mater 169 (2009) 691–696. https://doi.org/10.1016/J.JHAZMAT.2009.03.150.

[135] L. Bilińska, M. Gmurek, S. Ledakowicz, Comparison between industrial and simulated textile wastewater treatment by AOPs – Biodegradability, toxicity and cost assessment, Chemical Engineering Journal 306 (2016) 550–559. https://doi.org/10.1016/J.CEJ.2016.07.100.

[136] M.A. Oliver-Tolentino, E. Jiménez-Álvarez, M. De Jesús Martínez-Ortiz, E. García-Báez, M.O. Franco-Hernández, A. Guzmán-Vargas, Effective electro-fenton degradation of reactive black 5 dye using modified electrode with Cu-zeolites, Journal of New Materials for Electrochemical Systems 17 (2014) 71–75. https://doi.org/10.14447/JNMES.V17I2.426.

[137] B. Palas, G. Ersöz, S. Atalay, Fenton-like oxidation of reactive black 5 in the presence of LABO3 (B: Fe, Co, Mn, Ni) perovskite catalysts, Journal of the Turkish Chemical Society, Section A: Chemistry 5 (2018) 37–44. https://doi.org/10.18596/JOTCSA.370758.

[138] I.M. Joni, L. Nulhakim, M. Vanitha, C. Panatarani, Characteristics of crystalline silica (SiO2) particles prepared by simple solution method using sodium silicate (Na2SiO3) precursor, in: J Phys Conf Ser, Institute of Physics Publishing, 2018. https://doi.org/10.1088/1742-6596/1080/1/012006.

[139] K. Kordatos, S. Gavela, A. Ntziouni, K.N. Pistiolas, A. Kyritsi, V. Kasselouri-Rigopoulou, Synthesis of highly siliceous ZSM-5 zeolite using silica from rice husk ash, Microporous and Mesoporous Materials 115 (2008) 189–196. https://doi.org/10.1016/J.MICROMESO.2007.12.032.

[140] H. Younesi, Z. Ghasemi, Preparation and Characterization of Nanozeolite NaA from Rice Husk at Room Temperature without Organic Additives, J Nanomater 2011 (2011) 858961. https://doi.org/10.1155/2011/858961.

[141] A. Cristiane, K. Nascimento, Study of Rice Husk Ash by Infrared Spectroscopy, International Journal of Science and Engineering Investigations 9 (2020). https://doi.org/10.1111/j.1551-2916.2011.04988.x.

[142] D.M. Ibrahim, S.A. El-Hemaly, F.M. Abdel-Kerim, Study of rice-husk ash silica by infrared spectroscopy, Thermochim Acta 37 (1980) 307–314. https://doi.org/10.1016/0040-6031(80)87160-7.

[143] J. Coates, Interpretation of Infrared Spectra, A Practical Approach, Encyclopedia of Analytical Chemistry (2000). https://doi.org/10.1002/9780470027318.A5606.

[144] A.Y. Atta, B.Y. Jibril, B.O. Aderemi, S.S. Adefila, Preparation of analcime from local kaolin and rice husk ash, Appl Clay Sci 61 (2012) 8–13. https://doi.org/10.1016/J.CLAY.2012.02.018.

[145] Chemistry LibreTexts, Infrared Spectroscopy Absorption Table, (n.d.). https://chem.libretexts.org/Ancillary_Materials/Reference/Reference_Tables/Spectroscopic_Reference_Tables/Infrared_Spectroscopy_Absorption_Table.

[146] B. Arkles, G.L. Larson, Silicon Compounds: Silanes and Silicones, A Survey of Properties and Chemistry (2013).

[147] A.M. Puziy, O.I. Poddubnaya, A. Martínez-Alonso, F. Suárez-García, J.M.D. Tascón, Surface chemistry of phosphorus-containing carbons of lignocellulosic origin, Carbon N Y 43 (2005) 2857–2868. https://doi.org/10.1016/J.CARBON.2005.06.014.

[148] S. Aprilia, B. Arifin, N. Arahman, A. Amin, A. Wicaksono, D. Bakhtiar, Synthesis and characterization film polypropylene/rice husk and rice husk ash nanocomposites, Rasayan J. Chem 12 (1001) 994–1001. https://doi.org/10.31788/RJC.2019.1225144.

[149] A. Cristiane, K. Nascimento, Study of Rice Husk Ash by Infrared Spectroscopy, International Journal of Science and Engineering Investigations 9 (2020). https://doi.org/10.1111/j.1551-2916.2011.04988.x.

[150] B. Manoj, A.G. Kunjomana, K.A. Chandrasekharan, Chemical leaching of low rank coal and its characterization using SEM/EDAX and FTIR, Journal of Minerals & Materials Characterization & Engineering 8 (2009) 821–832.

[151] J.J. Chen, X. Kong, K. Sumida, M.A. Manumpil, J.R. Long, J.A. Reimer, ExSitu NMR relaxometry of metal-organic frameworks for rapid surface-area screening, Angewandte Chemie - International Edition 52 (2013) 12043–12046. https://doi.org/10.1002/anie.201305247.

APPENDICES

A. Procedure for Peak Fitting via OriginLab

- Upload data on OriginLab and plot.
- Click on the curve to apply PeakFitting
- Click on; *Analysis > Peaks and Baseline > Peak Analyzer > Open Dialog*
- In the pop-up screen, choose *Fit Peaks (pro),* click on *Next*
- Define baseline if necessary, click on *Next* until "Find Peaks" section is reached.
- Disable auto find, add peaks manually by clicking on *Add*.
- Specify direction of the peaks to be fit on *Peak Finding Settings.*

Click on *Next* and *Finish*

B. Procedure for NMR spectroscopy

- Open SpinSolve software.
- Insert the shim sample in the NMR spectrometer.
- Go to; *system* > *shim*, choose the desired shimming procedure.
- When the shimming ends and software pops up the *"Ready to use"* screen, remove the shim sample and insert the analyte.
- Go to; ^{1}H screen and select the desired analysis method.
- Set the parameters if there are any.
- Click on *"Start"* to begin analysis.
- When the analysis ends, click on MNova option on the right bottom part of the screen to export data to MestReNova software.

Data can be exported from MestReNova after the corrections, if there are any, by *File* > *save as* > *NMR CSV file* path.

C. Quantitative XRD Analysis by Scherrer Equation

Scherrer equation is given by;

$$\boldsymbol{\tau = \frac{K\lambda}{\beta cos\theta}}$$

where τ is the average crystallite size in nm, K is a dimensionless shape factor (K=0.9), λ is the x-ray wavelength (0.154 nm), β is the full width at half of maximum intensity in radians, θ is Bragg angle in radians. To apply, Scherrer equation, XRD peak corresponding to the plane (1 1 1) was plotted in Figure C-1. θ is the half of peak position of the (1 1 1) plane, calculated as;

$$\frac{21.76°}{2} = 10.88° = 0.1899\, rad$$

To calculate FWHM, half of the maximum intensity is shown in Figure C-2 as dashed line, which crosses XRD pattern at 2θ = 21.56º and 21.98º. FWHM is then calculated as;

$$21.98° - 21.56° = 0.42° = 0.0073\, rad$$

Then, using the Scherrer formula, crystallite size for (1 1 1) plane was calculated as;

$$\tau = \frac{0.9 * 0.154\, nm}{0.0073\, rad * \cos(0.1899)} = 21\, nm$$

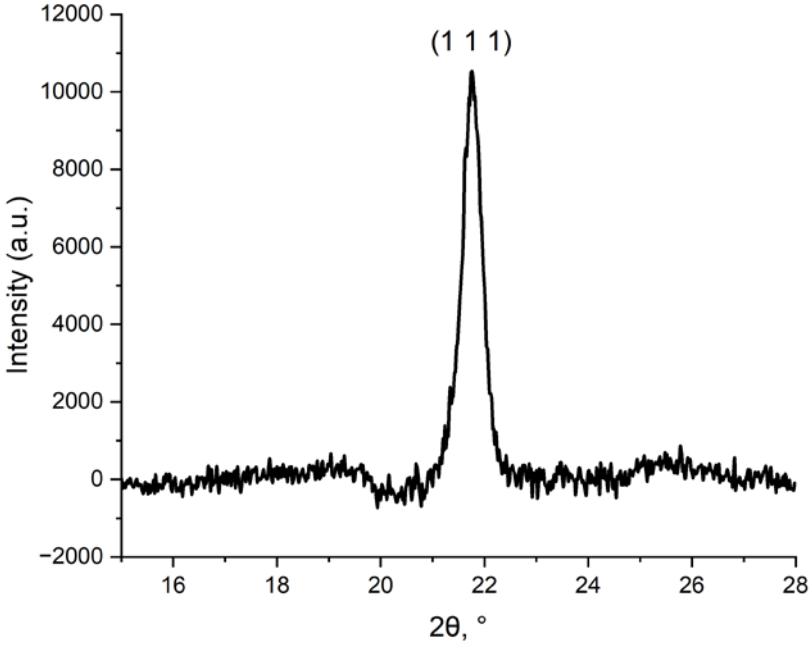

Figure C-1: (1 1 1) plane of SP-RHA-20 XRD pattern after baseline correction

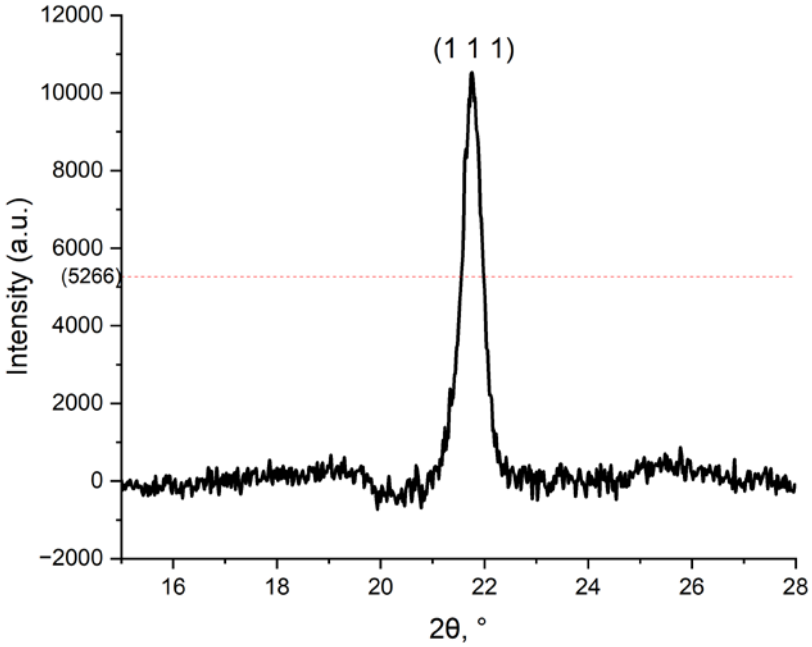

Figure C-2: FWHM of (1 1 1) plane of SP-RHA-20

D. TGA Profiles

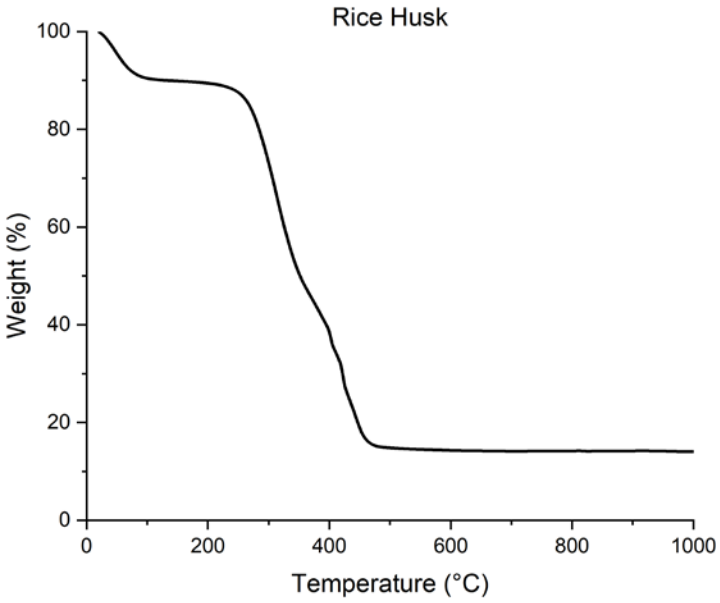

Figure D-1: Rice husk TGA profile

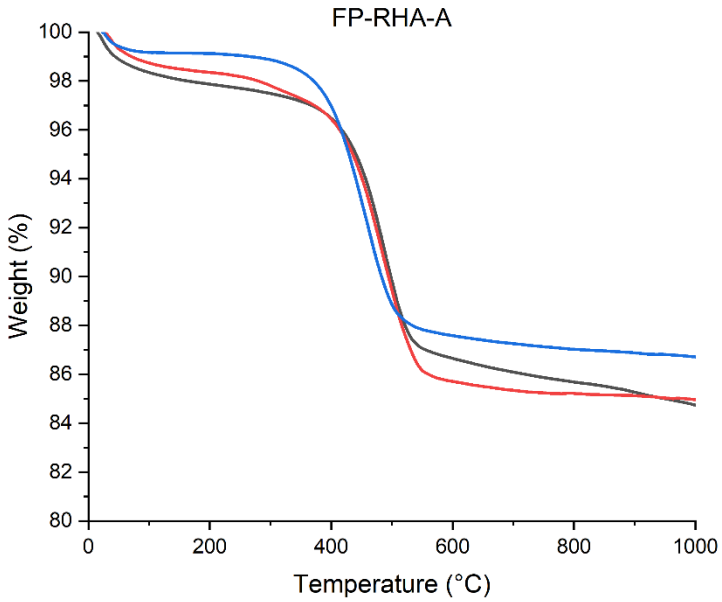

Figure D-2: FP-RHA-A TGA profiles

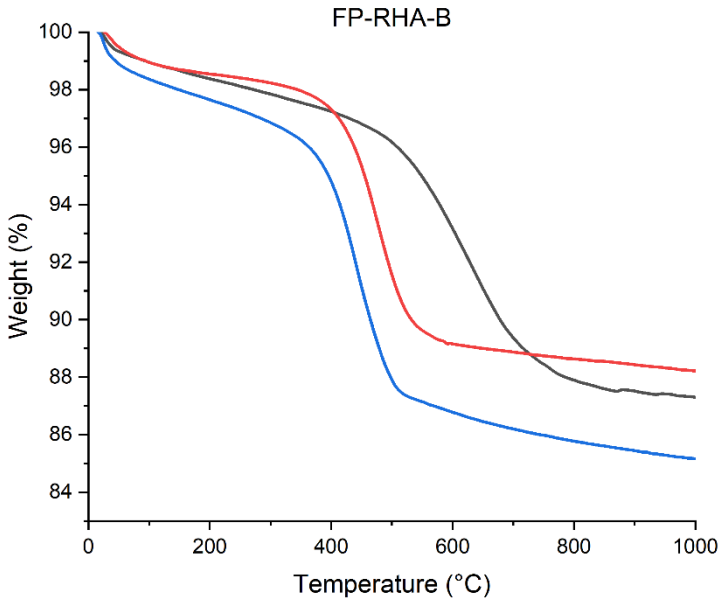

Figure D-3: FP-RHA-B TGA profiles

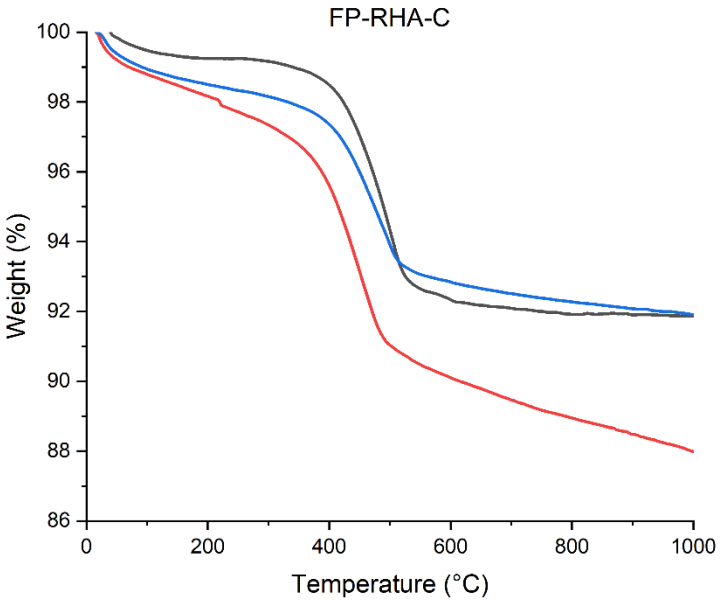

Figure D-4: FP-RHA-C TGA profiles

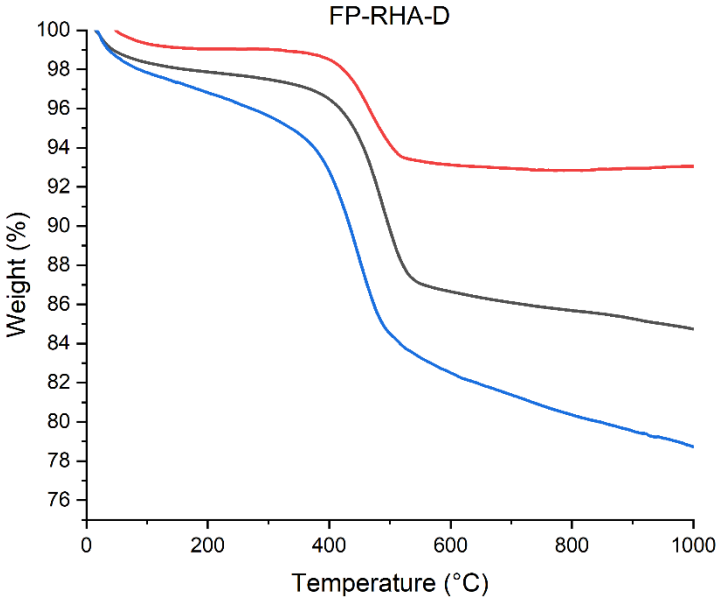

Figure D-5: FP-RHA-D TGA profiles

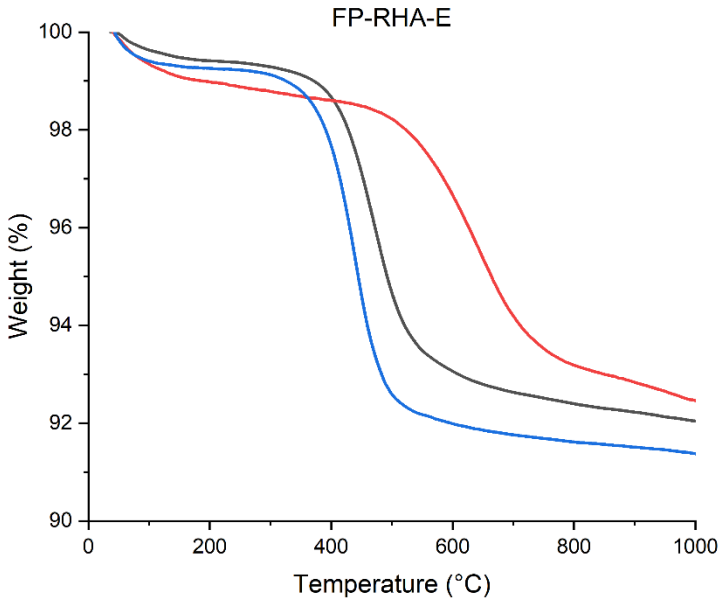

Figure D-6: FP-RHA-E TGA profiles

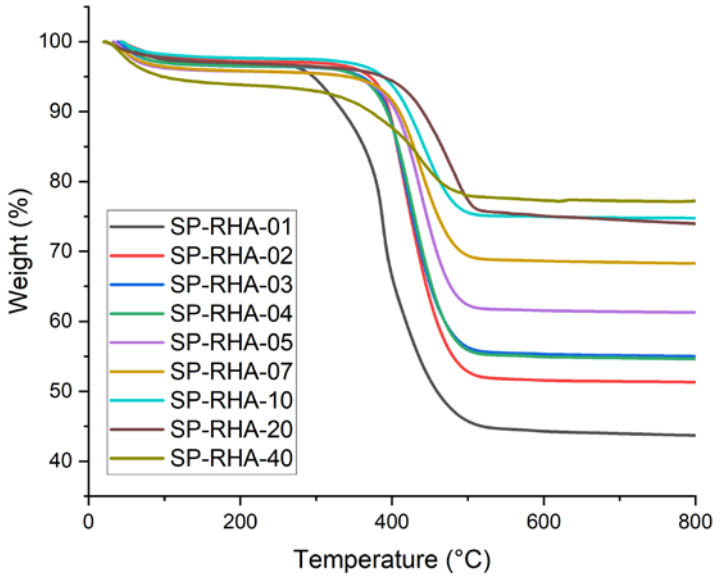

Figure D-7: SP-RHA TGA profiles

E. BET Isotherms

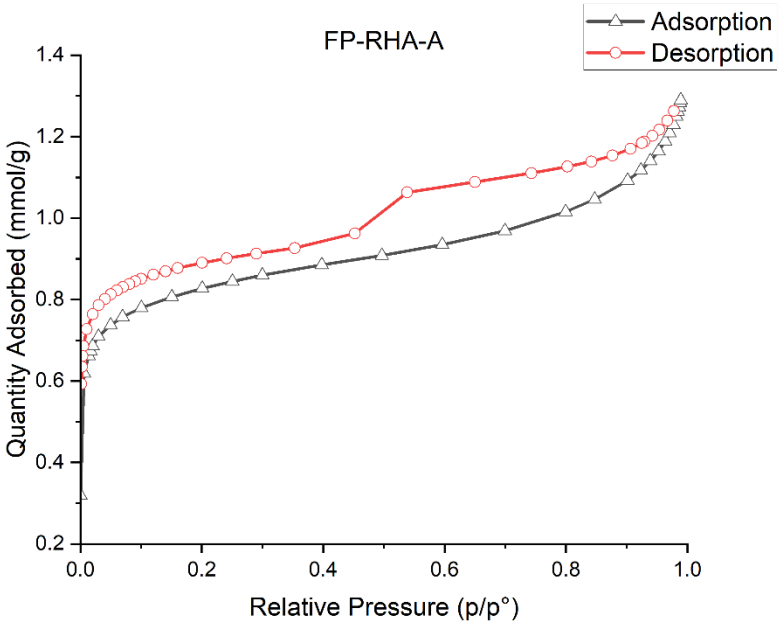

Figure E-1: BET isotherm of FP-RHA-A

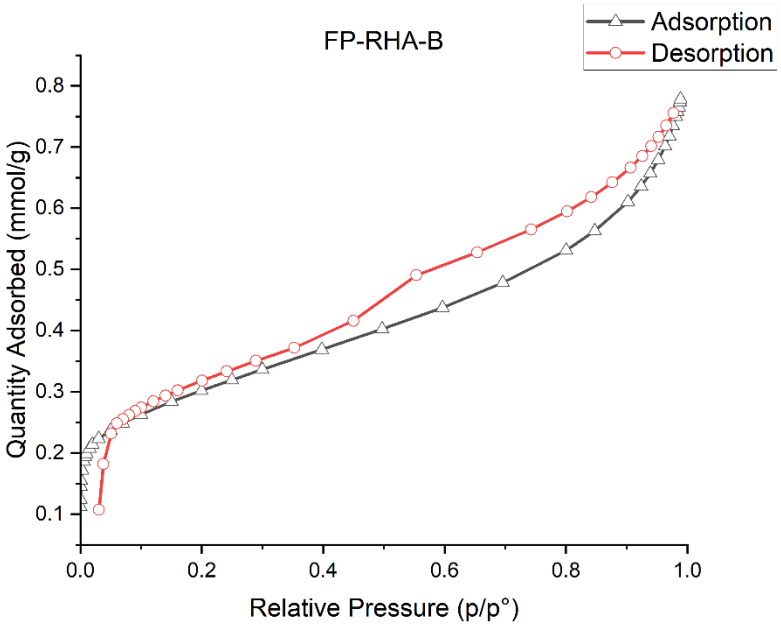

Figure E-2: BET isotherm of FP-RHA-B

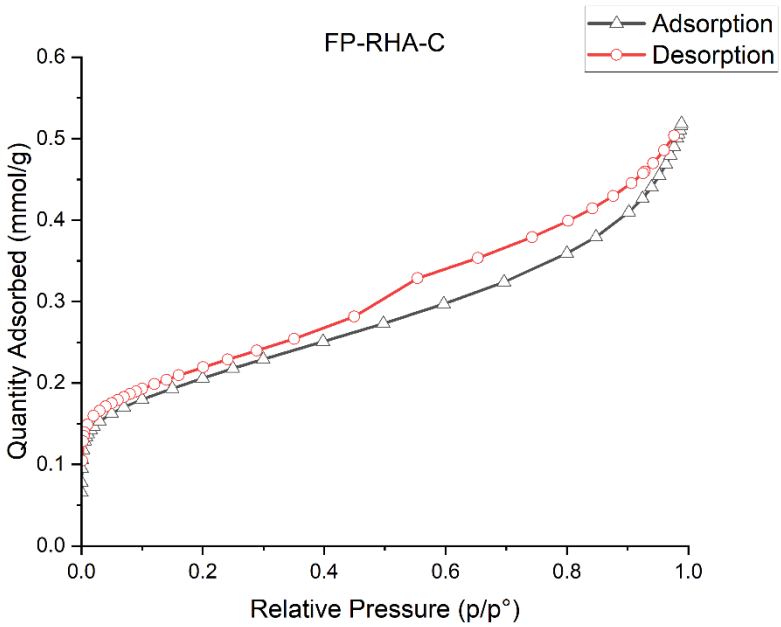

Figure E-3: BET isotherm of FP-RHA-C

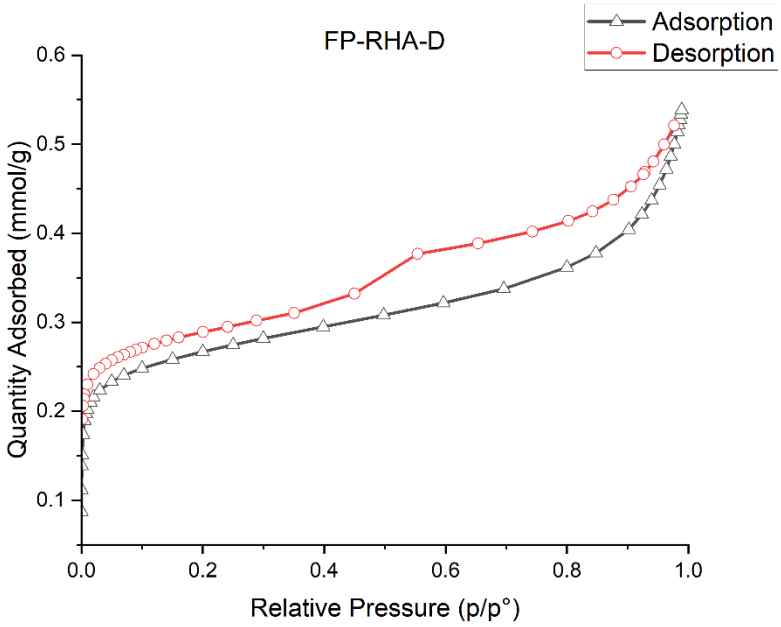

Figure E-4: BET isotherm of FP-RHA-D

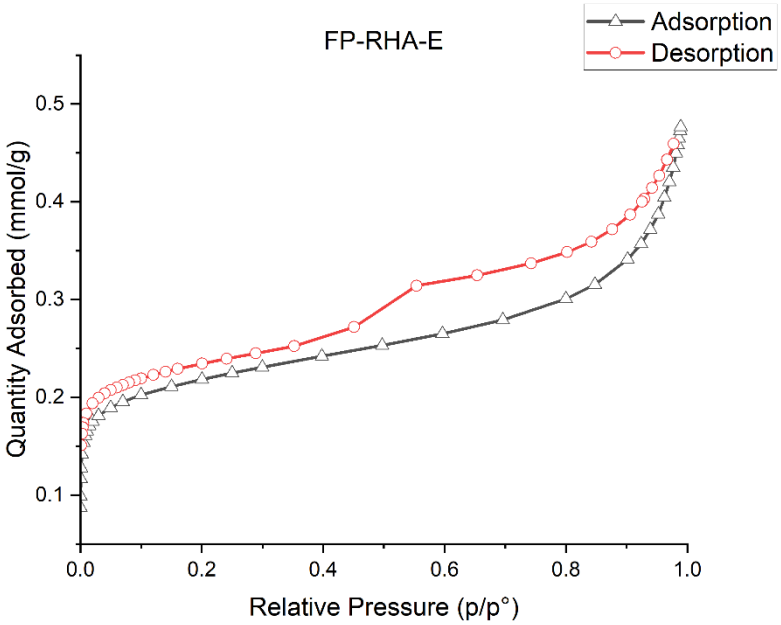

Figure E-5: BET isotherm of FP-RHA-E

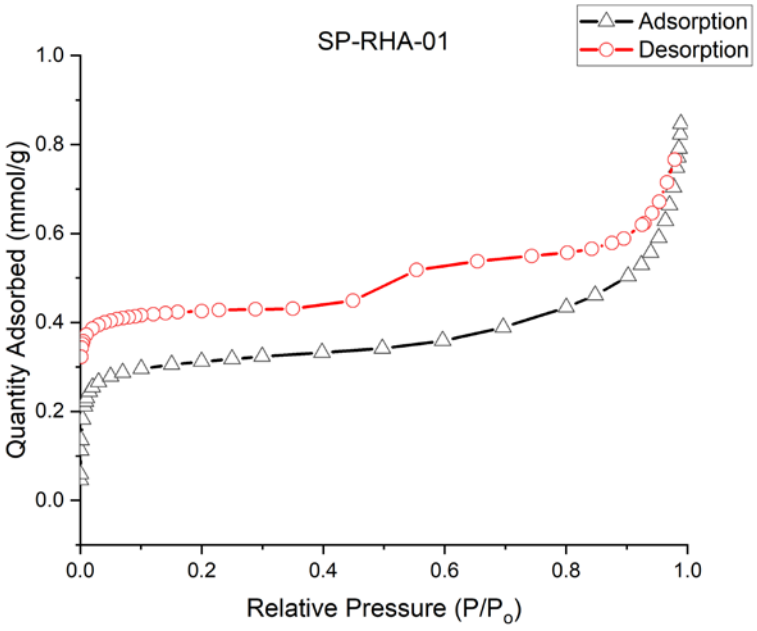

Figure E-6: BET isotherm of SP-RHA-01

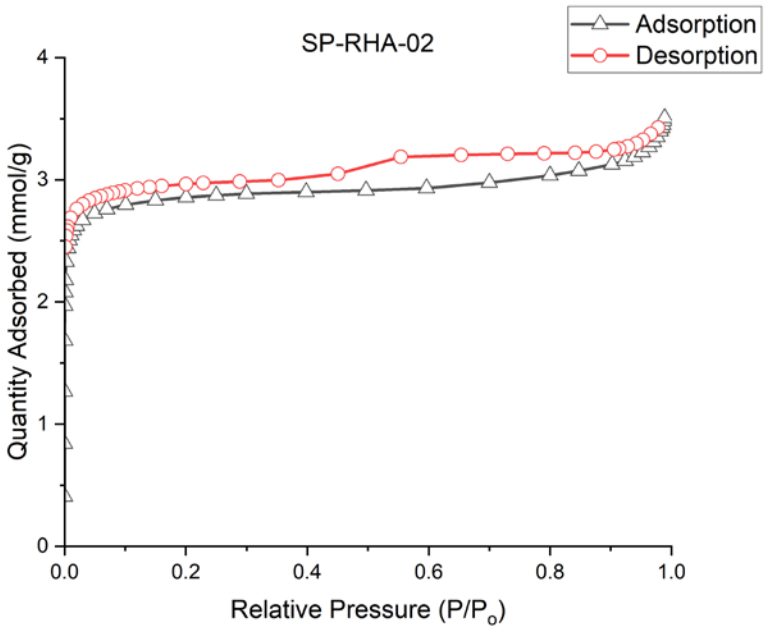

Figure E-7: BET isotherm of SP-RHA-02

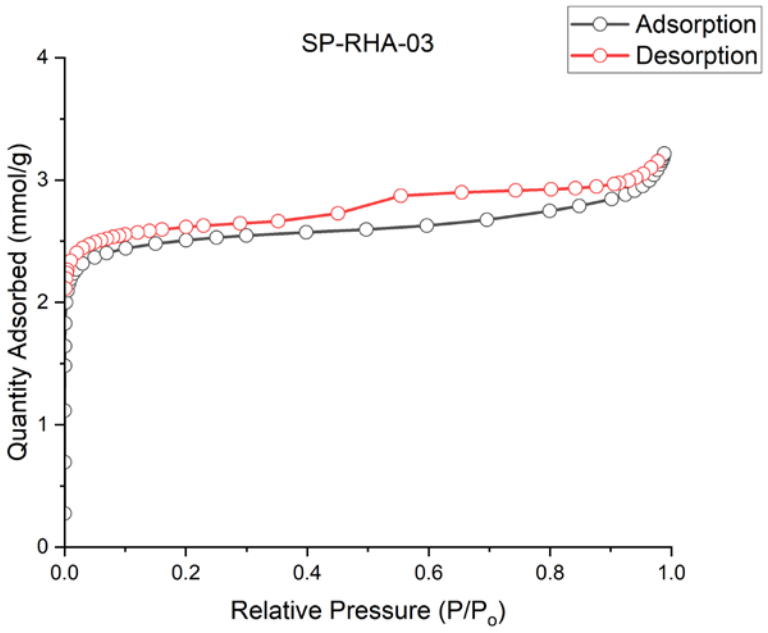

Figure E-8: BET isotherm of SP-RHA-03

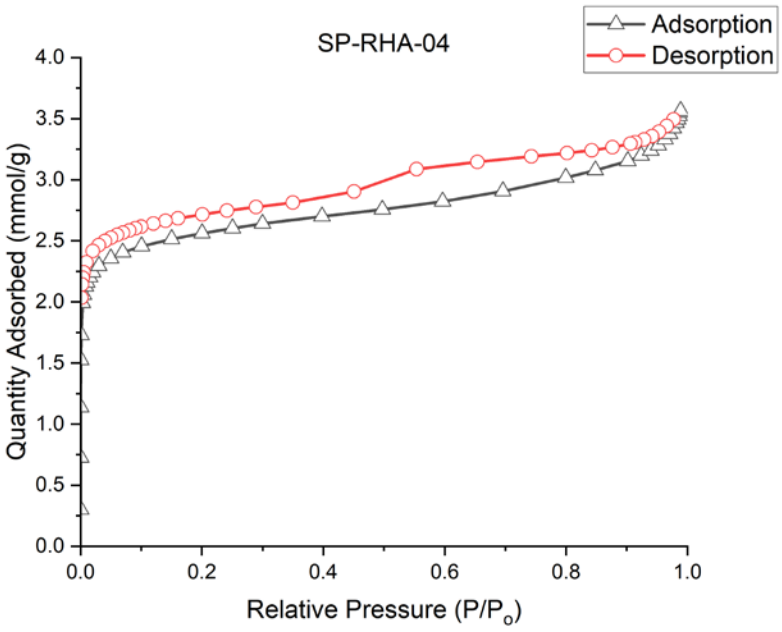

Figure E-9: BET isotherm of SP-RHA-04

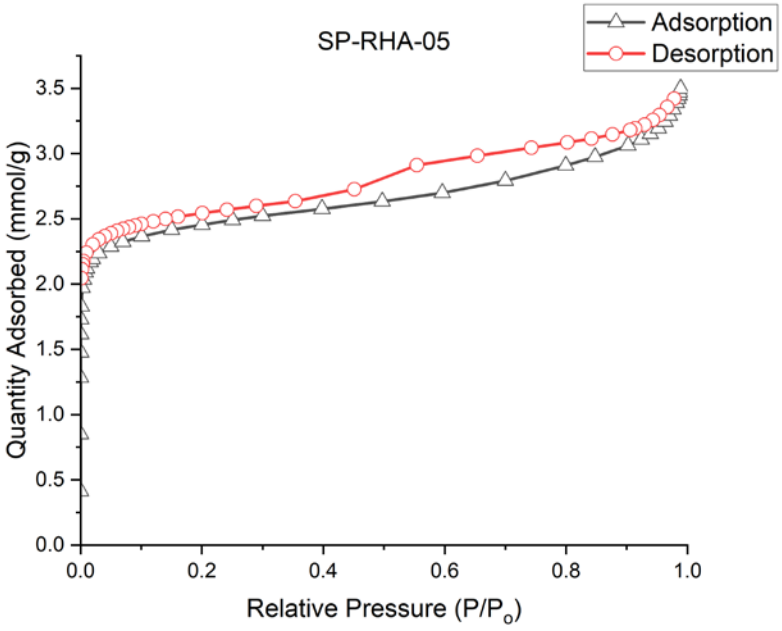

Figure E-10: BET isotherm of SP-RHA-05

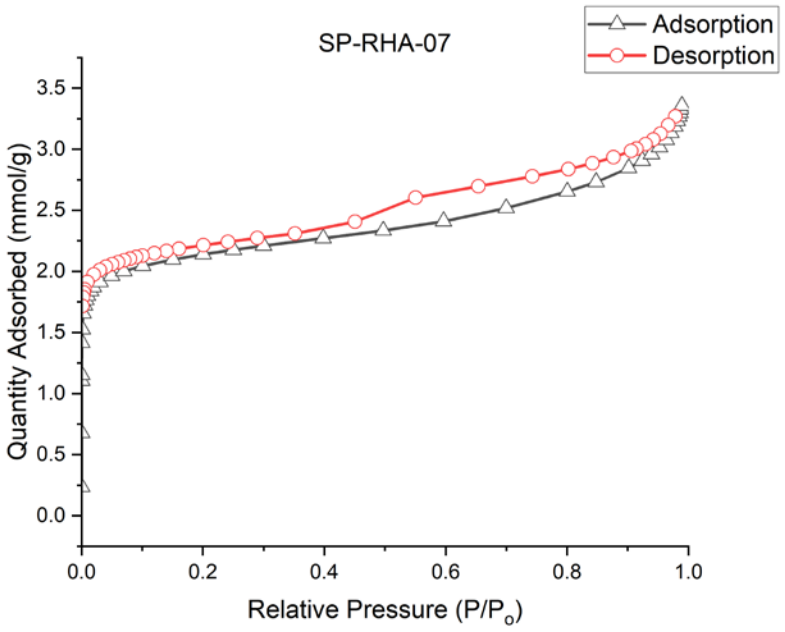

Figure E-11: BET isotherm of SP-RHA-07

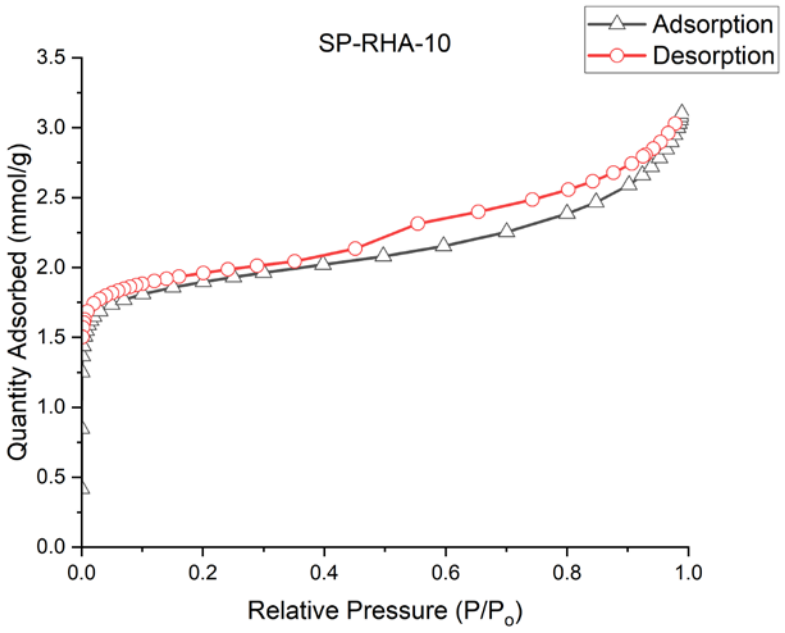

Figure E-12: BET isotherm of SP-RHA-10

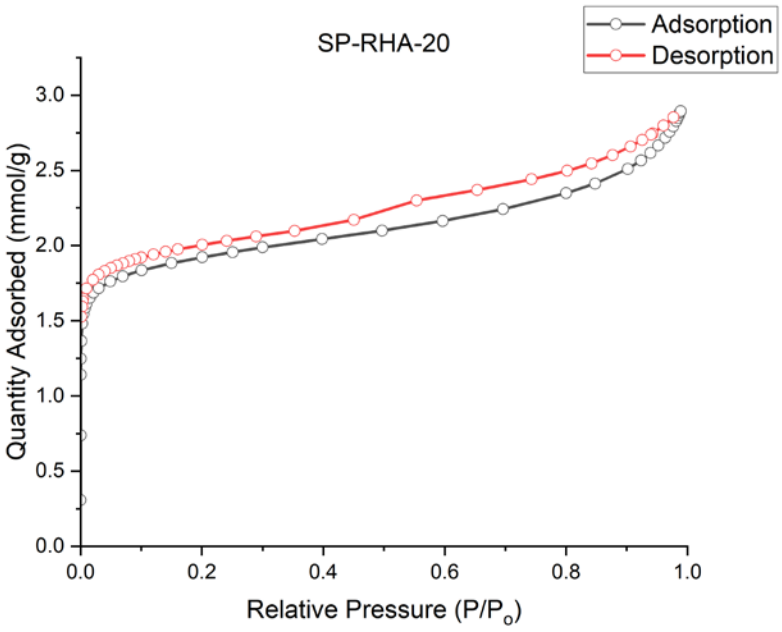

Figure E-13: BET isotherm of SP-RHA-20

F. Deconvoluted Raman Spectra

1. Deconvolution was applied as described in Appendix A.
2. Integral results for all peaks were automaticallycalculated by the software.
3. Degree of Disorder was calculated by dividing the area under the D band at ~1300 cm^{-1} to the area under the G band at ~1600cm^{-1}.

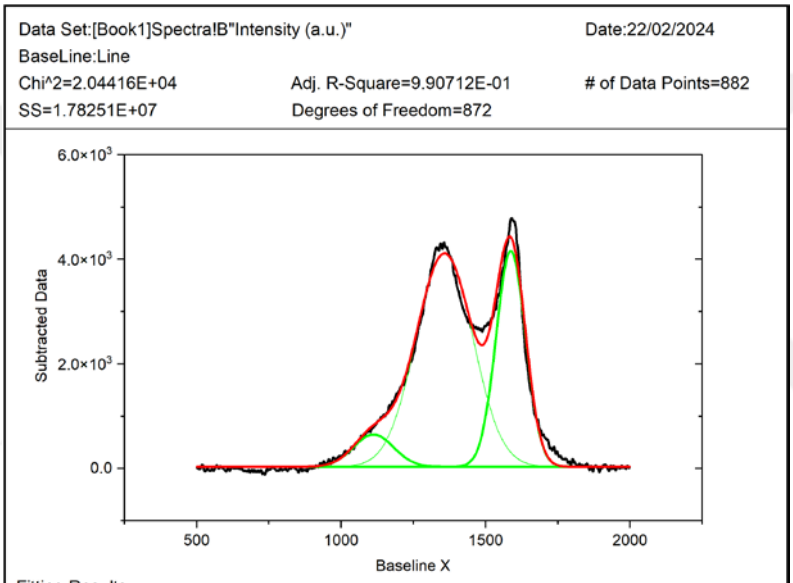

Fitting Results

Peak Index	Peak Type	Area Intg	FWHM	Max Height	Center Grvty	Area IntgP
1	Gaussian	1004485.53967	231.43403	4077.40879	1357.72887	61.27947
2	Gaussian	528101.75808	120.34266	4122.54867	1587.12225	32.21728
3	Gaussian	106600.4773	162.30405	617.01765	1111.91929	6.50325

Figure F-1: Deconvoluted Raman spectra of FP-RHA-A

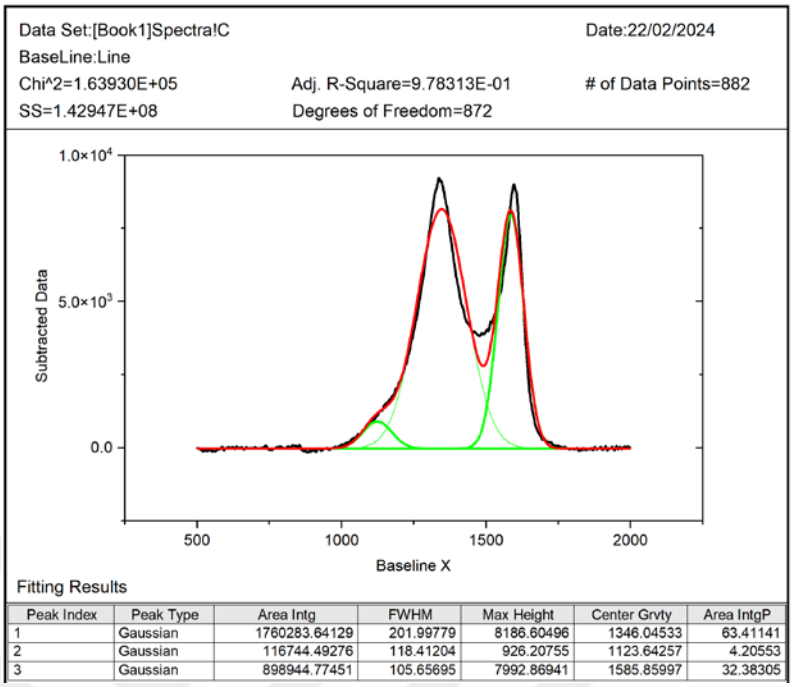

Fitting Results

Peak Index	Peak Type	Area Intg	FWHM	Max Height	Center Grvty	Area IntgP
1	Gaussian	1760283.64129	201.99779	8186.60496	1346.04533	63.41141
2	Gaussian	116744.49276	118.41204	926.20755	1123.64257	4.20553
3	Gaussian	898944.77451	105.65695	7992.86941	1585.85997	32.38305

Figure F-2: Deconvoluted Raman spectra of FP-RHA-B

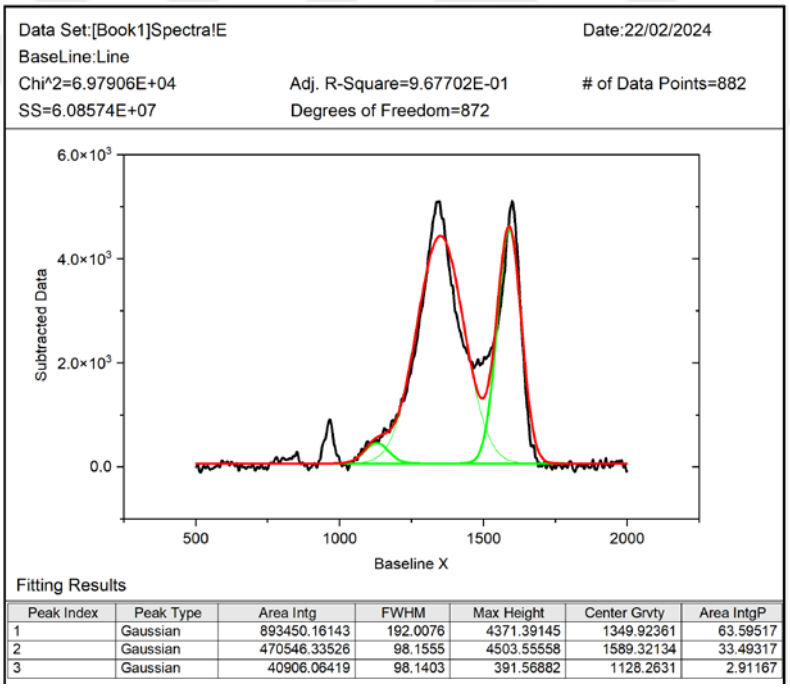

Fitting Results

Peak Index	Peak Type	Area Intg	FWHM	Max Height	Center Grvty	Area IntgP
1	Gaussian	893450.16143	192.0076	4371.39145	1349.92361	63.59517
2	Gaussian	470546.33526	98.1555	4503.55558	1589.32134	33.49317
3	Gaussian	40906.06419	98.1403	391.56882	1128.2631	2.91167

Figure F-3: Deconvoluted Raman spectra of FP-RHA-C

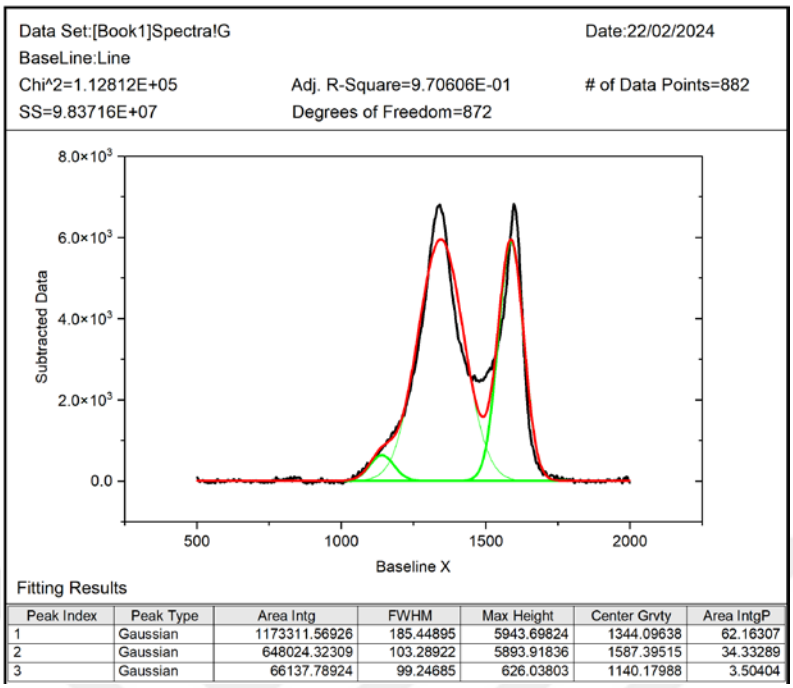

Fitting Results

Peak Index	Peak Type	Area Intg	FWHM	Max Height	Center Grvty	Area IntgP
1	Gaussian	1173311.56926	185.44895	5943.69824	1344.09638	62.16307
2	Gaussian	648024.32309	103.28922	5893.91836	1587.39515	34.33289
3	Gaussian	66137.78924	99.24685	626.03803	1140.17988	3.50404

Figure F-4: Deconvoluted Raman spectra of FP-RHA-D

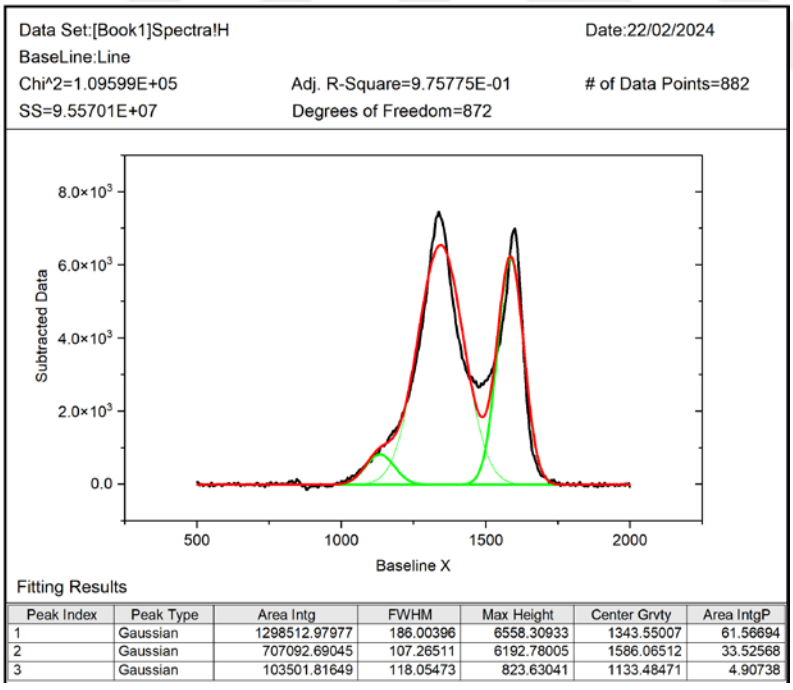

Fitting Results

Peak Index	Peak Type	Area Intg	FWHM	Max Height	Center Grvty	Area IntgP
1	Gaussian	1298512.97977	186.00396	6558.30933	1343.55007	61.56694
2	Gaussian	707092.69045	107.26511	6192.78005	1586.06512	33.52568
3	Gaussian	103501.81649	118.05473	823.63041	1133.48471	4.90738

Figure F-5: Deconvoluted Raman spectra of FP-RHA-E

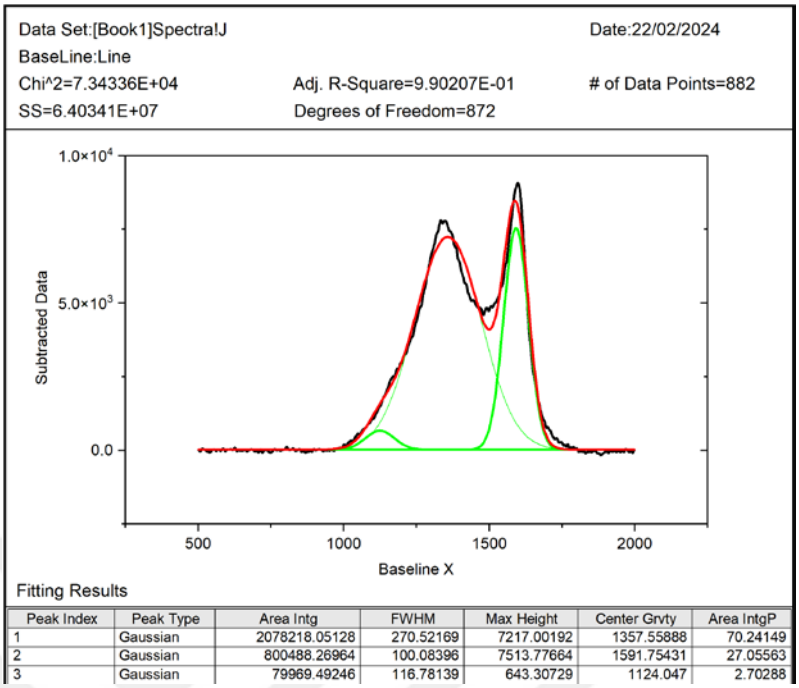

Fitting Results

Peak Index	Peak Type	Area Intg	FWHM	Max Height	Center Grvty	Area IntgP
1	Gaussian	2078218.05128	270.52169	7217.00192	1357.55888	70.24149
2	Gaussian	800488.26964	100.08396	7513.77664	1591.75431	27.05563
3	Gaussian	79969.49246	116.78139	643.30729	1124.047	2.70288

Figure F-6: Deconvoluted Raman spectra of SP-RHA-01

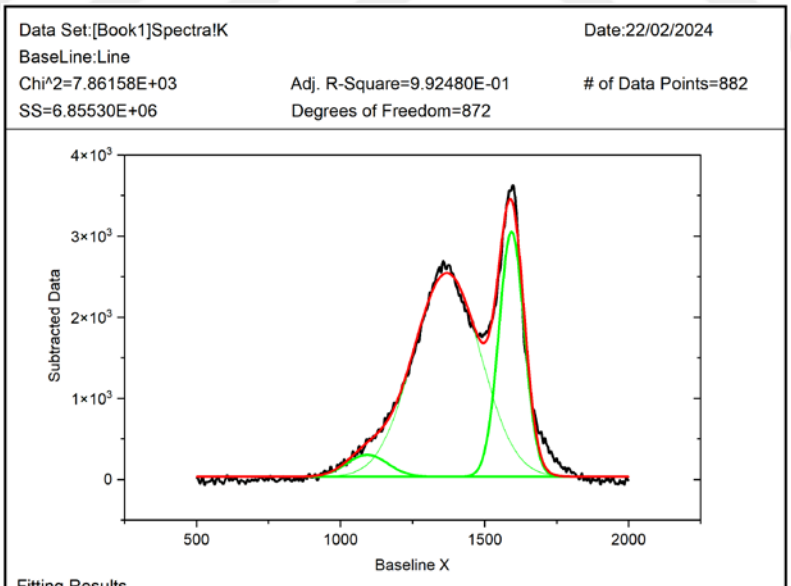

Fitting Results

Peak Index	Peak Type	Area Intg	FWHM	Max Height	Center Grvty	Area IntgP
1	Gaussian	735683.8786	275.24931	2510.91956	1368.62451	65.94523
2	Gaussian	331940.39873	103.33863	3017.62467	1593.08505	29.75447
3	Gaussian	47973.96441	166.84949	270.11489	1092.15071	4.30029

Figure F-7: Deconvoluted Raman spectra of SP-RHA-02

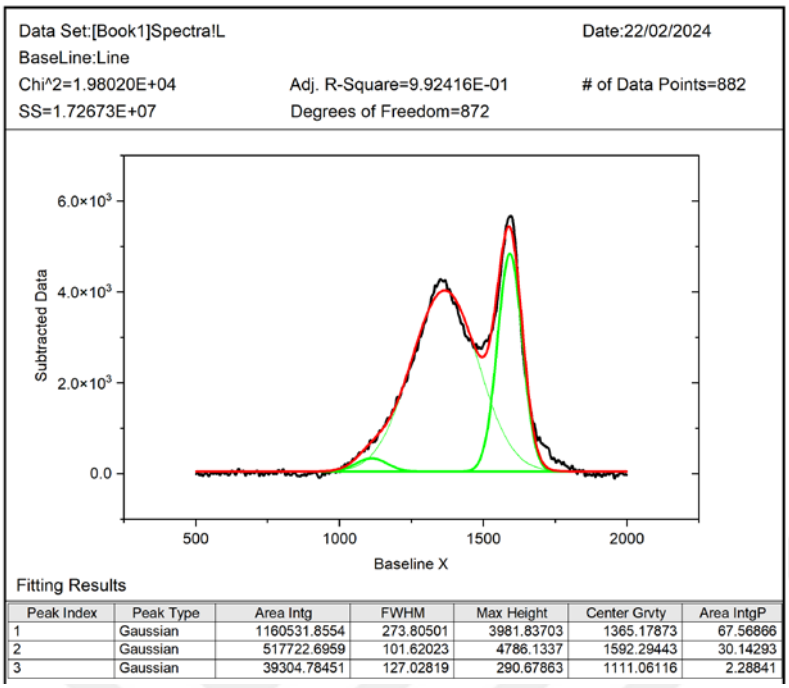

Fitting Results

Peak Index	Peak Type	Area Intg	FWHM	Max Height	Center Grvty	Area IntgP
1	Gaussian	1160531.8554	273.80501	3981.83703	1365.17873	67.56866
2	Gaussian	517722.6959	101.62023	4786.1337	1592.29443	30.14293
3	Gaussian	39304.78451	127.02819	290.67863	1111.06116	2.28841

Figure F-8: Deconvoluted Raman spectra of SP-RHA-03

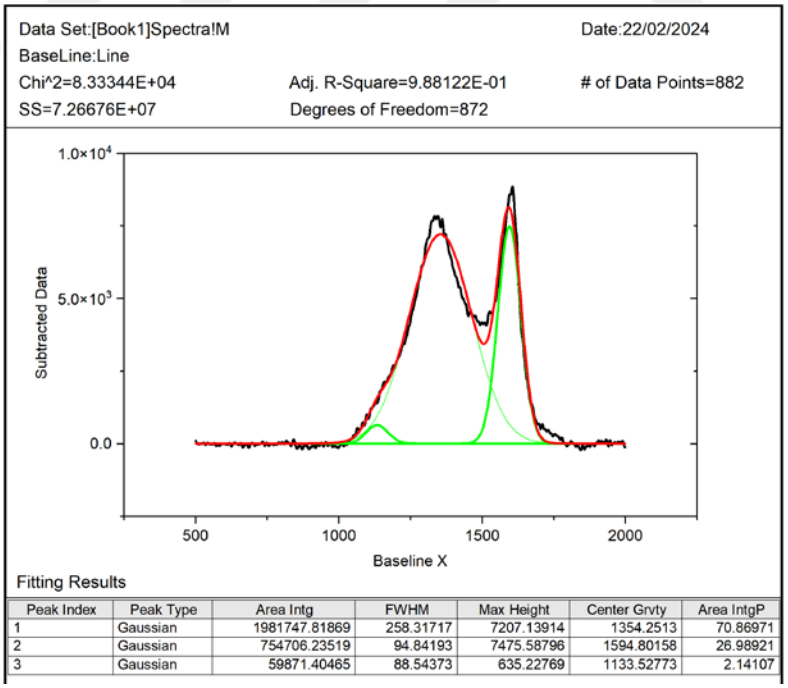

Fitting Results

Peak Index	Peak Type	Area Intg	FWHM	Max Height	Center Grvty	Area IntgP
1	Gaussian	1981747.81869	258.31717	7207.13914	1354.2513	70.86971
2	Gaussian	754706.23519	94.84193	7475.58796	1594.80158	26.98921
3	Gaussian	59871.40465	88.54373	635.22769	1133.52773	2.14107

Figure F-9:Deconvoluted Raman spectra of SP-RHA-04

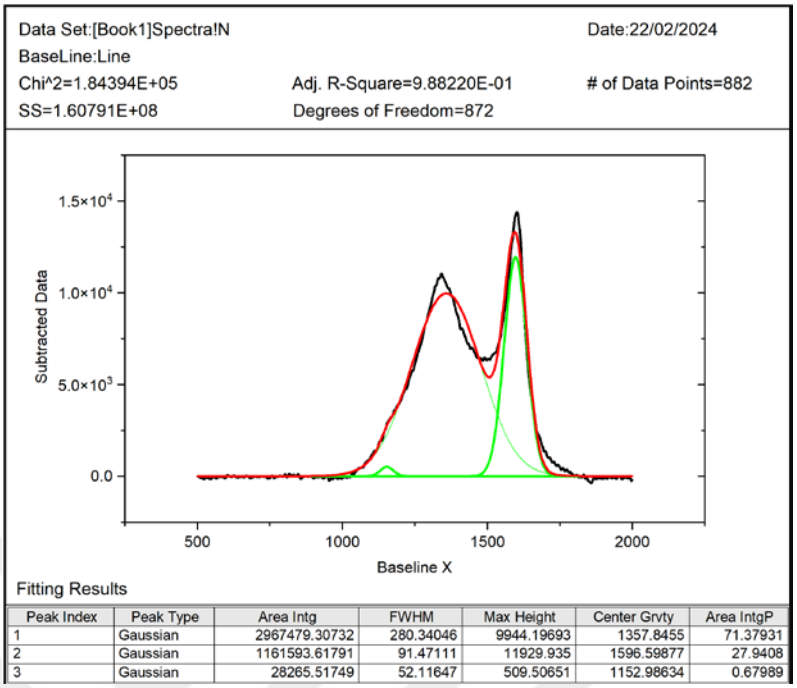

Fitting Results

Peak Index	Peak Type	Area Intg	FWHM	Max Height	Center Grvty	Area IntgP
1	Gaussian	2967479.30732	280.34046	9944.19693	1357.8455	71.37931
2	Gaussian	1161593.61791	91.47111	11929.935	1596.59877	27.9408
3	Gaussian	28265.51749	52.11647	509.50651	1152.98634	0.67989

Figure F-10: Deconvoluted Raman spectra of SP-RHA-05

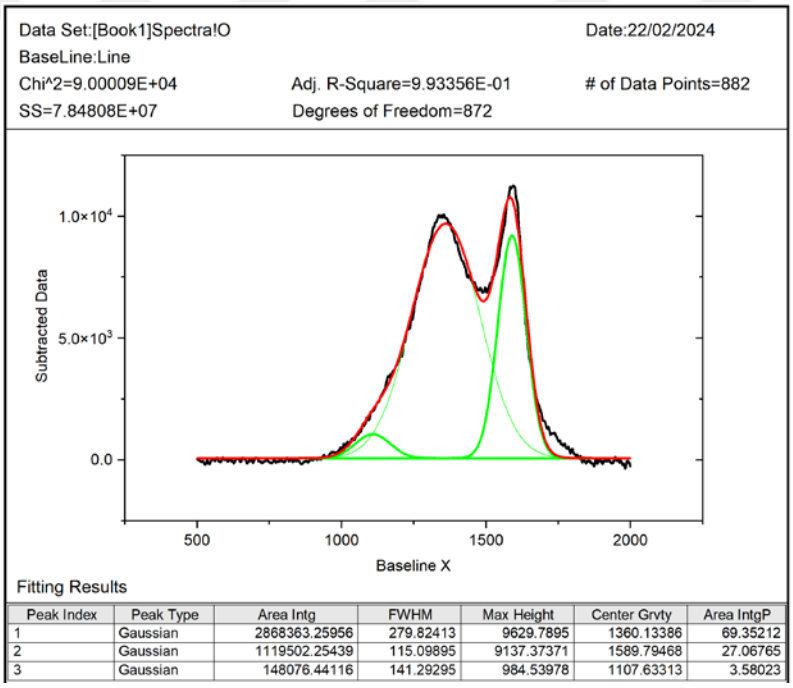

Fitting Results

Peak Index	Peak Type	Area Intg	FWHM	Max Height	Center Grvty	Area IntgP
1	Gaussian	2868363.25956	279.82413	9629.7895	1360.13386	69.35212
2	Gaussian	1119502.25439	115.09895	9137.37371	1589.79468	27.06765
3	Gaussian	148076.44116	141.29295	984.53978	1107.63313	3.58023

Figure F-11: Deconvoluted Raman spectra of SP-RHA-07

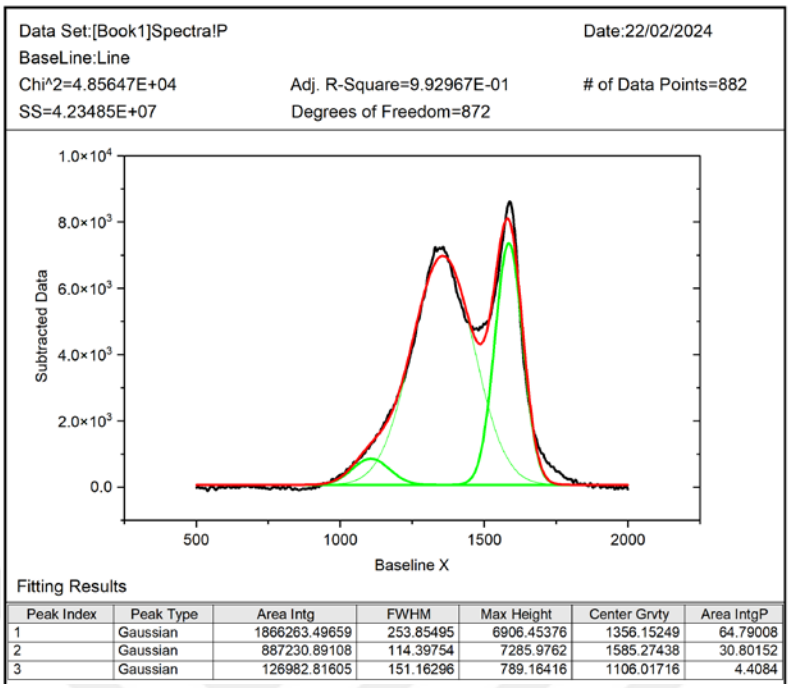

Fitting Results

Peak Index	Peak Type	Area Intg	FWHM	Max Height	Center Grvty	Area IntgP
1	Gaussian	1866263.49659	253.85495	6906.45376	1356.15249	64.79008
2	Gaussian	887230.89108	114.39754	7285.9762	1585.27438	30.80152
3	Gaussian	126982.81605	151.16296	789.16416	1106.01716	4.4084

Figure F-12: Deconvoluted Raman spectra of SP-RHA-10

G. NMR Studies – RHA Pore Size Distribution by T_2 Relaxation

Procedure

1. 105 mg of FP-RHA-A was mixed with 1500 mg DI water.
2. Several T_2 relaxation time spectra were measured by changing the final echo time and number of steps.
3. Area under the spectra were calculated by integration for intensity calculations.
4. Area at each step was plotted against time.
5. Inverse laplace transform was applied to the plot to obtain pore size distributions with respect to T_2 relaxation time [60,151].

Pore size distribution of FP-RHA-A by NMR relaxometry is given in Figure G-1.

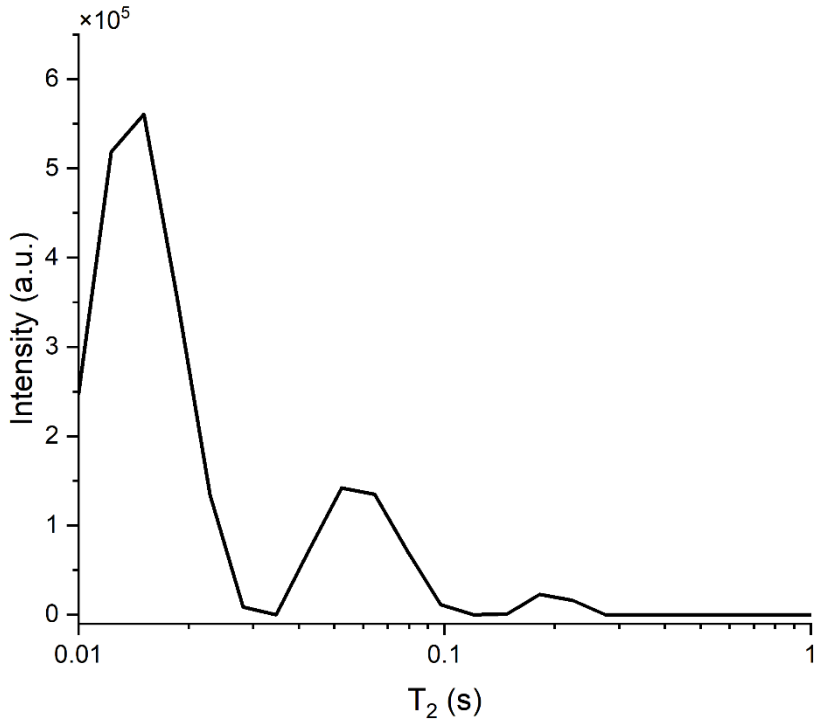

Figure G-1: FP-RHA-A pore size distribution by T_2 NMR relaxometry

H. NMR – Calibration for Ammonium Hydroxide Weight Fraction

Procedure

1. Prepare ammonium hydroxide solutions of different concentrations by mixing 29 wt% ammonium hydroxide solution and deionised water.
2. Obtain 1H spectrums of the solutions by NMR spectrometer.
3. Note the peak chemical shift.
4. Plot peak chemical shifts against ammonia weight fraction for each mixture.
5. Obtain the equation in the form $\delta = a + b * m_{NH_3}$.

Calibration curve is given in Figure G-2.

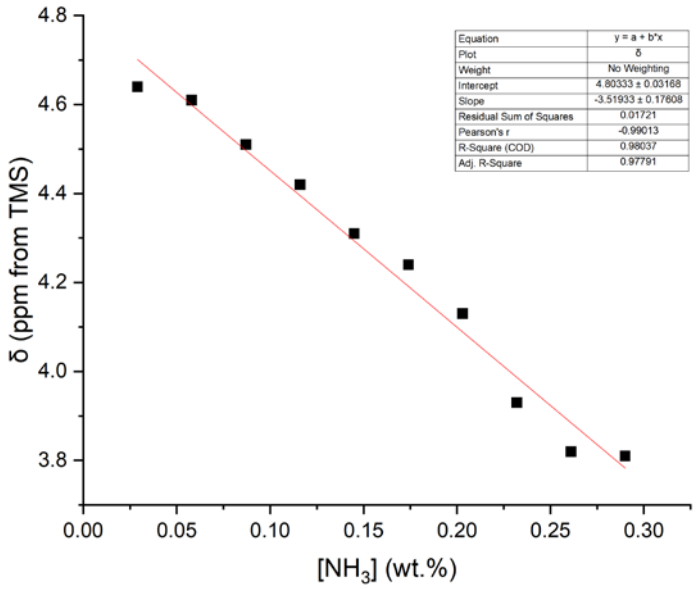

Figure G-2 :Ammonium hydroxide NMR calibration

Calibration equations

Chemical Shift Explicit: $\delta = 4.80 - 3.52 * m_{NH_3}$

Weight Fraction Explicit: $m_{NH_3} = 1.365 - 0.284 * \delta$

İ. RHA and Water Single Pulse Experiments

Numereous ^{1}H single pulse experiments were performed with FP-RHA-A and water mixtures of changing ratios. Spectra obtained from all those experiments are given in Figure I-1. Chemical shift of pure water is marked with dashed lines at 4.74 ppm on the plot.

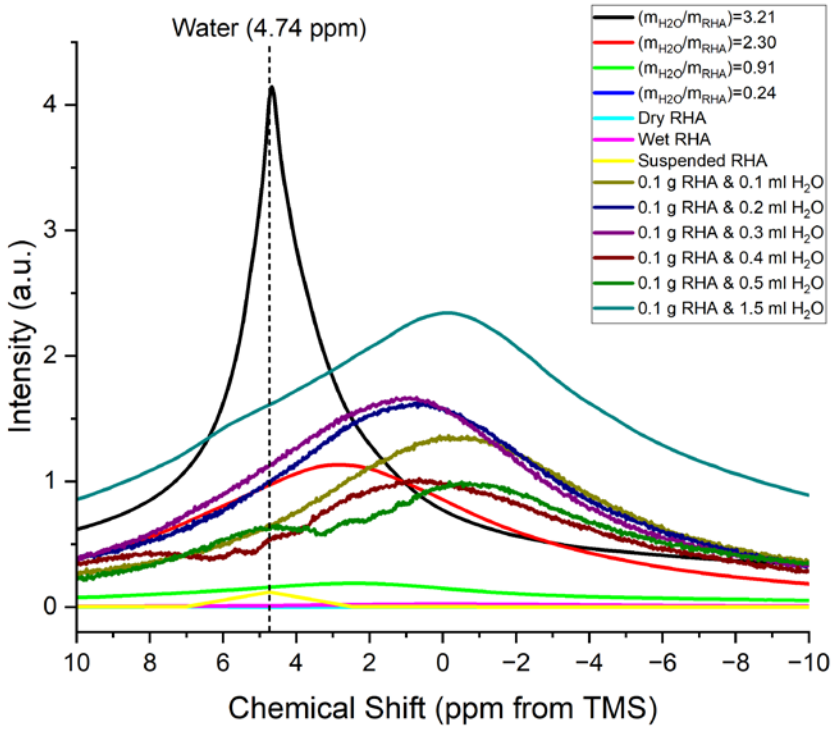

Figure I-1: RHA and water experiments on single pulse ^{1}H NMR

All of these experiments have an obvious nexus that is the fact that when RHA is mixed with water, peak of the spectrum shifts to right, in other words, the basic region. This indicates the predominantly basic surface of rice husk ash.

J. RB5 Adsorption Calibration Plot

UV-Vis spectra of RB5 at different concentrations are given in Figure J-1.

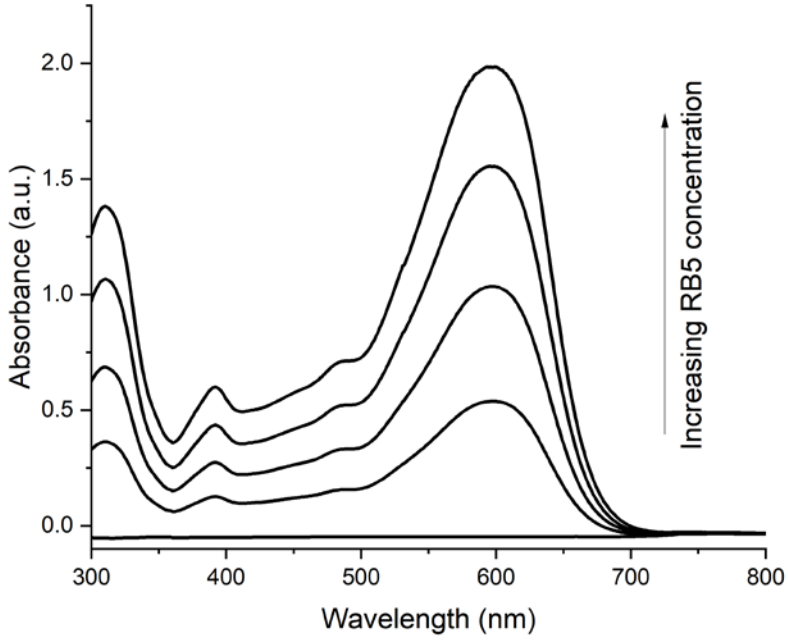

Figure J-1: UV-Vis spectra of RB5 at different concentrations

For the calibration curve, integral of the spectrum was calculated via OriginLab in the wavelength range of 500-700 nm, which corresponds to the characteristic peak of RB5, and plotted against concentration. Calibration plot of RB5 was given in Figure J-2.

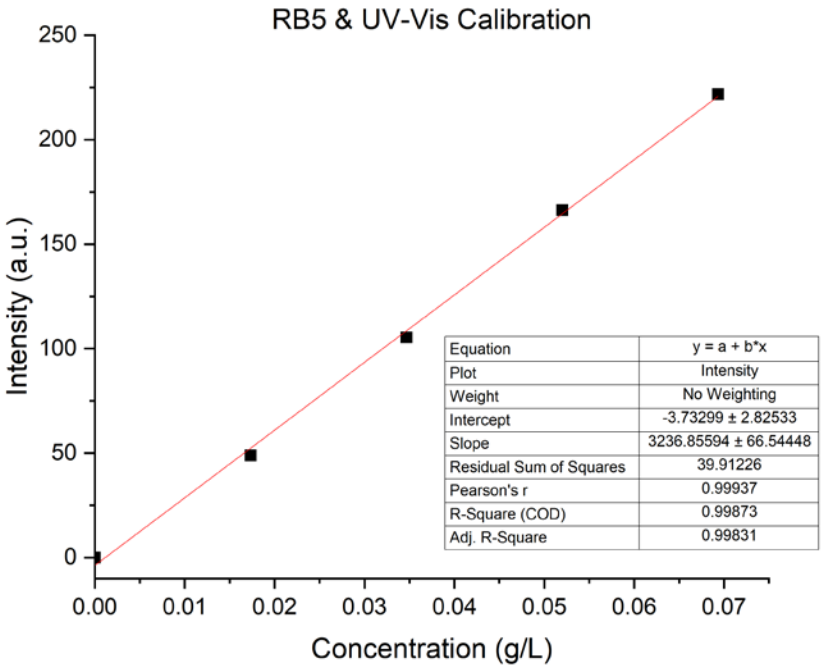

Figure J-2: Concentration calibration plot for RB5

K. Procedure for TPR Analysis

- Fill the U-shaped quartz reactor with sample, put quartz wool to both sides.
- Connect the reactor to the system, close the doors of the furnace, insert thermocouple. Cover the top with insulation material.
- Crush some ice and mix with isopropanol. Connect the cold trap filled with the mixture to the system. Cover the top with insulation material.
- Turn on the Micromeritics ChemiSorb 2750 , and temperature control systems.
- Open the TPx software, create a document for the experiment from *File* > *Open* > *Sample.* Fill in sample weight, and experiment details.
- Turn on He and H_2/Ar cylinder valves.
- Set the flowrate, switch to port A for helium. Set up for *bypass* and *short path*.
- Click on *continue*, wait for purge to finish.
- When purge is completed, set up the system for *sample* and *long path/cold trap.*
- Switch to port B for H_2/Ar. Wait for signal stabilization.
- Set up temperature ramp and final temperature on the temperature controller.
- Start the temperature ramp and data collecting.
- Check the software for the progress, wait until the experiment is completed.
- Switch to port A for He during the cooling. Remove insulation material.
- Open the doors of the furnace and the cooling fan when system cooled down to safer levels.
- Save the TCD signal data collected.

Turn off the cylinder valves, temperature controller and the Micromeritics ChemiSorb 2750 system.

L. Quantitative Analysis with TPR

Hydrogen consumption was calibrated for TCD signal using 0.0235 grams of Ag_2O. Calibration was completed by Melis Yarar of our research group [98]. Silver oxide calibration curve is given below in Figure L-1.

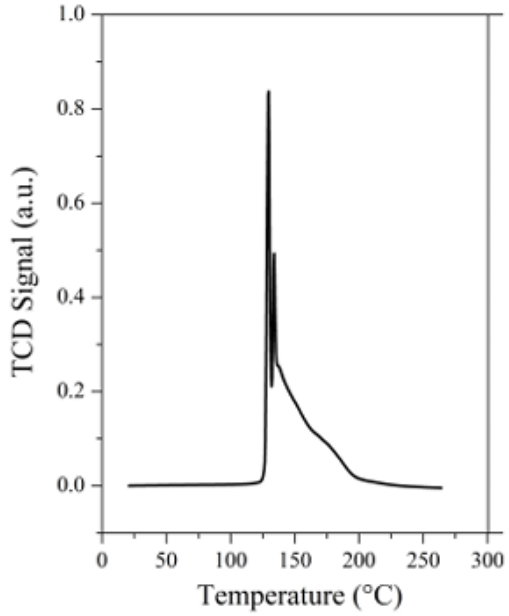

Figure L-1: Silver oxide calibration curve for quantitative TPR analysis [98]

Silver oxide is reduced in the form of the following reaction:

$$Ag_2O + H_2 \rightarrow 2Ag + H_2O$$

0.0235 grams of silver oxide equates to 0.000101 mols. From the stoichiometry, required hydrogen is known to be equimolar with silver oxide.

Peak area was found to be 10.73 [98]. Therefore, calibration can be completed by dividing the mols of hydrogen consumed to the total area:

$$\frac{0.000101\ mol}{10.73\ area} = 0.00000945\ mols\frac{H_2}{area}$$